ALMA MATER STUDIORUM - UNIVERSITY OF BOLOGNA

SCHOOL OF ENGINEERING AND ARCHITECTURE

DEPARTMENT OF
ELECTRICAL, ELECTRONIC AND INFORMATION ENGINEERING
“GUGLIELMO MARCONI”
DEI

MASTER DEGREE IN
ELECTRICAL ENERGY ENGINEERING

MASTER THESIS
in
Applied Superconductivity

NUMERICAL STUDY OF QUENCH IN AN HTS SUPERCONDUCTING MAGNET FOR THE 40T NHMFL PROJECT

AUTHOR	SUPERVISOR
Sayantani Maiti	Prof. Marco Breschi
	CO-SUPERVISOR
	Ing. Lorenzo Cavallucci
	Ing. Antonio Macchiagodena

Academic Year 2024/25

ACKNOWLEDGEMENT

A heartfelt gratitude to my supervisor, Prof. Marco Breschi who instilled the curiosity in me about applied superconductivity in his lectures. I'd like to thank my co-supervisor Lorenzo Cavallucci for guiding me calmly throughout my thesis and Antonio, who often came up with different solutions to the problems. My deepest appreciation to all my professors, who made me feel heard and seen in this university, by handling doubts and questions delicately.

I am also grateful to my classmates, Diego, Gianluca, Elio, Lorenzo, Giovanni, Amir, Edoardo, Salvatore, Filippo, Francesco, Weronika, Marco, with whom I have shared the exam stress and the banter between lectures. My academic career would not be half as fun if not for them. I am thankful for the vibrant Indian group of friends to whom I could turn to, whenever I missed home.

To Munni's and Manjinder's families, thank you for always welcoming me home. To, Tracy, Khushi and Prashant, thanks for always checking on me from time to time. Thank you Fit-activ for providing me a healthy workout space. To Mansib, thanks for the impeccable studio where I could jam with lovely musicians, whenever I wanted.

To Shagnik, thank you for being the partner in crime in literally everything – cooking, workouts, music, travel. I really appreciate your selfless attitude to be there for your people, whenever needed.

My masters journey was possible due to my parents' relentless efforts throughout their lives. They taught me kindness, persistence and believed in me that it is never too late to go back to school.

I'd like to thank my sister, who became an inspiration for me when she moved abroad to pursue her masters. When I left my long-term stable job, I was without salary. From giving pocket money for errands to sometimes financing our trips, she has done it all. I couldn't be more proud of her and more thankful for being my little sister and my academic senior.

Lastly, I'd take a moment to pat myself on the back, to have made it through this competitive, gruelling yet very satisfying masters degree of Electrical Energy Engineering from the University of Bologna. It was not easy, but I had fun.

CONTENTS

ABBREVIATIONS

1. K – Kelvin
2. 2D – 2 dimensional
3. LSC – Large Scale Coil
4. LTS – Low Temperature Superconductor
5. HTS – High Temperature Superconductor
6. MRI – Magnetic Resonance Imaging
7. NHMFL – National High Magnetic field laboratory
8. SC – superconducting coil
9. T -Tesla
10. DEI - Department of Electrical, Electronic and Information Engineering
11. BCS theory– Bardeen Cooper Schreiffer theory
12. ITER – International Thermonuclear Experimental Reactor
13. MW- Mega Watt
14. REBCO- rare-earths barium copper oxide
15. YBCO – Yttrium Barium copper oxide

LIST OF FIGURES

LIST OF TABLES

ABSTRACT

The National High Magnetic Field Laboratory (NHMFL), USA, is advancing the development of a 40 T superconducting magnet, combining high-temperature REBCO inner coils with low-temperature superconducting (LTS) outer coils. As part of this initiative, a full-scale prototype coil—designated as the “Large Scale Coil” (LSC) has been fabricated and experimentally tested at 4.2 K using quench protection heaters.

This thesis presents a comprehensive electrothermal numerical study of the LSC quench behaviour, performed using a coupled finite element method (FEM) model developed at the Department of Electrical, Electronics and Information Engineering (DEI), University of Bologna. The model incorporates homogenization of REBCO tapes and coil materials to reduce computational load while accurately coupling distributed contact resistances across the coil’s pancake submodules. Critical to this approach is the dynamic integration of temperature and field-dependent material properties, achieved through custom C-code subroutines linked to COMSOL Multiphysics simulations.

Comparative analysis between simulation results and experimental data reveals a rather good agreement in current decay, voltage rise, and resistive transitions across magnet modules. Notably, the study highlights the disproportionate quench sensitivity of modules 2 to 6; not necessarily the central, highest-field modules; due to combined magnetic field strength and field angle effects on the critical current.

Further tests are ongoing on the LSC, and the model will be applied to eventually predict and interpret the experimental results. This work provides a useful tool to guide the design of next prototypes in the frame of 40 T magnet project.

1. INTRODUCTION

Superconductivity [1] was discovered in 1911 when Kamerlingh Onnes observed a sudden drop in resistivity of an extremely pure mercury below 4.2 Kelvin (K). Zero resistivity meant transport of current without any energy losses. The potential application of this discovery was recognised in a variety of industries.

Superconductors are classified based on its critical temperature (T_c) as low temperature superconductors (LTS) and high temperature superconductors (HTS). And based on its critical field (H_c) as Type I superconductors and Type II superconductors. HTS materials and their applications in the magnet industry have become a significant topic of research in recent years due to their high T_c i.e. between 30 K to 140 K.

The use of superconducting materials enable technological advances in fields where physical limits of conventional technologies have been reached such as using superconducting magnets to generate the high magnetic fields needed for the development of magnetic resonance imaging (MRI) machines or introducing superconducting magnets to guide electron beams in synchrotrons and accelerators at scientific user facilities.[1] High field laboratories such as National High Magnetic Field Laboratory (NHMFL) located in Tallahassee, USA offers a wide range and robust interdisciplinary research facilities including physics, biology, engineering, and chemistry. It was founded in 1994 and is one of the twelve high-field laboratories worldwide. The Magnet Lab, one of the labs of NHMFL, holds numerous world records for high field magnet development.

A magnet can be either a permanent magnet or an electromagnet. A superconducting magnet is a type of electromagnet which are made of coils of superconducting wire or superconducting cables and can be turned on and off. A resistive magnet, on the other hand, is a type of electromagnet that is made from normal-conducting metal such as copper and aluminium [2]. A purely resistive magnet dissipates heat and consumes high power to produce high field of the order of 30 Tesla (T). A purely superconductive magnet, instead, consumes very low power to produce high field [4]. However, world's highest field dc magnets, for more than 50 years, consisted of a combination of resistive and superconducting coils (SC) that are referred to as a "hybrid" magnet. The peak field available has been 45 T for over 20 years in Tallahassee, USA. There is presently a 'revolution' underway in hybrid magnet development. A second 45 T hybrid was completed in 2022 in Hefei, China that might be upgraded to 48 T in a few years. The high field lab in Grenoble, France is also testing a hybrid magnet intended to reach 43.5 T but which also might be upgraded to 46 T in a few years. In addition, the lab in Nijmegen, The Netherlands is presently assembling a hybrid magnet intended to operate at 46 T. Several studies have been published and presented at academic forums with conceptual designs of hybrid magnets with fields up to 60 T. [3].

In 2016, NHMFL developed a 32 T all-superconductive magnet. Department of Electrical, Electronic and Information Engineering (DEI), University of Bologna (UniBO), Italy carried out the numerical analysis of the experimental results of the quench tests of the prototype coils [5]. In 2024, NHMFL started developing a 40 T all-superconductive magnet. In the frame of this project, a prototype coil, named "Large Scale Coil" (LSC) is under development. A numerical analysis is ongoing at the University of Bologna to study quench in the LSC. My thesis is based on this numerical study of quench where we have built the model of the magnet in COMSOL, simulated a quench with different operational currents and analysed their results.

2. LITERATURE REVIEW

In 1908, physicist Heike Kamerlingh Onnes had succeeded in liquefying helium at 4.15 K making his laboratory the first to reach such low temperatures. In 1911, he discovered the phenomenon of superconductivity while studying the electrical behaviour of certain materials at extremely low temperatures. During his experiments, he noticed that impurities significantly affected electrical resistance. He thus concentrated on producing increasingly pure samples. His assistant, Gilles Holst, who had perfected mercury purification methods, suggested testing mercury at low temperatures. Onnes observed that mercury's electrical resistance dropped sharply when the temperature reached 4.2 K, from a measurable 0.12 Ω to about 10^{-5} Ω (as shown in Fig. 1).

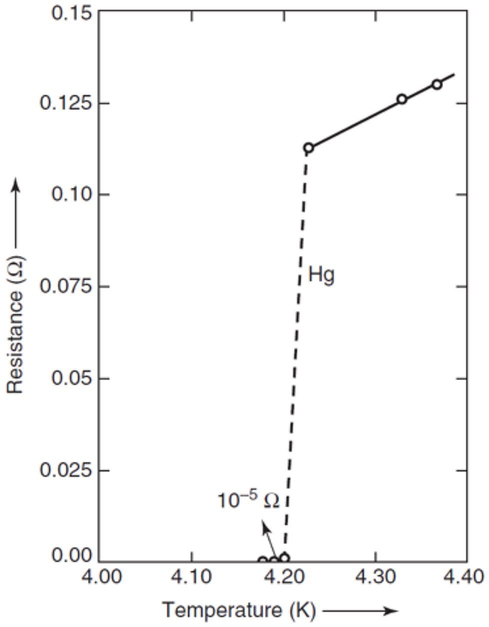

Figure 1 - Resistance of mercury suddenly dropped as it was cooled below 4.2K which led to the discovery of superconductivity.

In pure metals, electrical resistance arises from the interaction between moving electrons and oscillating lattice ions caused by thermal energy as shown in Fig. 2. The more intense the ion vibrations, the greater the disruption to electron flow, leading to increased resistance.

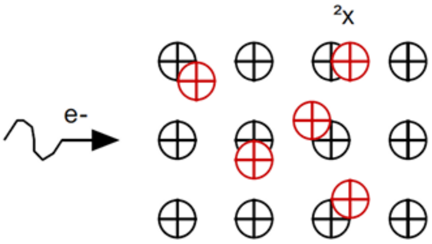

Figure 2 - The interaction of electrons with ions of the crystal lattice, which vibrate due to thermal agitation around their equilibrium position.

Thus, electrical resistance in metals depends on temperature—it decreases as temperature drops. However, even at absolute zero, resistance doesn't reach zero due to imperfections and structural defects in the lattice, which create a residual resistivity**.** According to Matthiessen's Rule, total resistivity is the sum of thermal and residual components:

$$\rho(total) = \rho_t + \rho_r \qquad \textit{(Eq. 1)}$$

where:

- ρ_t = resistivity due to lattice vibrations
- ρ_r = resistivity due to structural defects

An ideal crystal would have zero resistivity when cooled to absolute zero, however, a real crystal, at absolute zero, still retains a residual resistivity due to crystal imperfections and impurities. Thus, resistivity in pure metals is a function of impurity content in the crystal lattice.

The Residual Resistivity Ratio (*RRR*) is defined as the ratio between copper's resistivity at room temperature and its resistivity at 4 K.

$$RRR = \frac{\rho_{300K}}{\rho_{4K}} \qquad \textit{(Eq.2)}$$

High *RRR* values indicate purer copper and low *RRR* values indicate the presence of impurities. In contrast, superconductors exhibit T_c regardless of lattice impurities (as shown in Fig. 3). Below $T_{c,}$ the resistivity of the superconductors is almost 0.

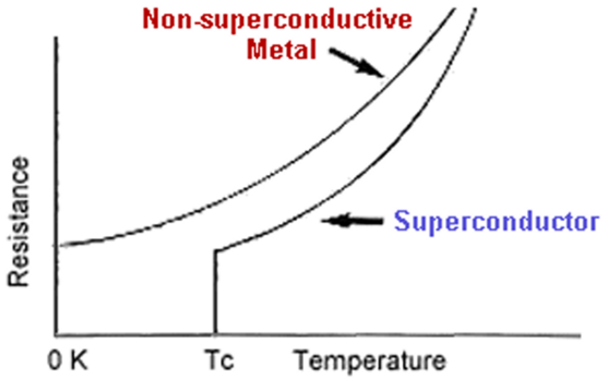

Figure 3 — Resistance vs. Temperature for superconductors and normal conductors; sudden drop in the resistance for Superconductor at T_c

In 1913, lead was also found to become superconducting at 7 K. In 1933, physicists Meissner and Ochsenfeld discovered that superconductors prevented the external magnetic fields from entering due to surface shielding currents. They were called perfect diamagnets.

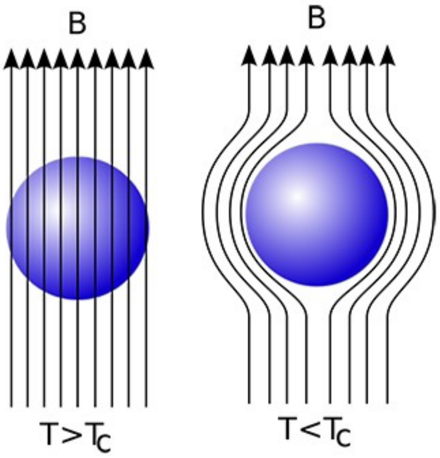

Figure 4 - Superconductor – Expulsion of magnetic field in a superconducting material proposed by Meissner

Diamagnetic materials are those materials that align weakly with an external magnetic field as opposed to paramagnetic materials that align strongly with an external magnetic field. Superconductors are *perfectly diamagnetic* as they do not allow any external magnetic field to pass through the bulk of the material below its critical temperature.

This effect is explained using the relationship between magnetic field induction $\vec{B}$ as a function of the magnetic field $\vec{H}$, magnetization vector $\vec{M}$ and the magnetic permeability of free space μ_0

$$\vec{B} = \mu_0(\vec{H} + \vec{M}) \qquad (Eq.3)$$

$$\text{If } \vec{B} = 0, \text{ then } \vec{H} = -\vec{M} \qquad (Eq.4)$$

This is due to surface screening currents that generate an internal magnetic induction field equal and opposing the external field. As a result, it ensures magnetic shielding. If the superconductor is considered a non-magnetic material and its diamagnetic behaviour is due to the screening currents, according to Maxwell Ampere law:

$$\nabla \times \vec{H} = \vec{J} \qquad (Eq.5)$$

can also be written as

$$\nabla \times \vec{B} = \mu_0\vec{J} \qquad (Eq.6)$$

If the external magnetic induction field ($\vec{B}$) is 0, then current flowing through the material ($\vec{J}$) is also 0. It can only exist on the surface of the superconductor.

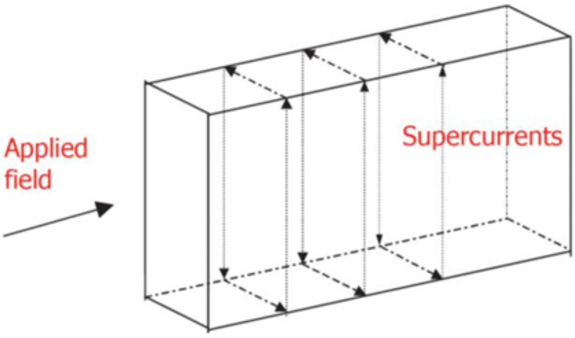

Figure 5- Screening current flowing on the surface of the superconductor

These shielding currents are confined to only a thin surface layer called the penetration depth (λ). Within this layer, the magnetic field decays exponentially.

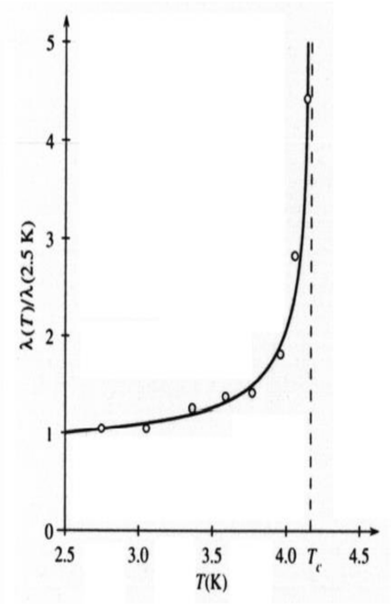

Figure 6 — Penetration depth vs. temperature

Eq.7 conveys that the penetration depth increases as the material approaches T_c . Hence, at critical temperature, the penetration depth becomes infinite, and surface currents start flowing through the bulk of the material. This leads to the penetration of the external magnetic field inside the material, and at this point, the superconductor *transitions*; from a superconducting state to a normal state.

$$\lambda(T) = \frac{\lambda(0)}{\sqrt{1-\left(\frac{T}{T_C}\right)^4}} \qquad \text{(Eq.7)}$$

The magnetization in an ideal conductor, depends on its history of application of the external magnetic field. A static magnetic field will be excluded if the material is cooled after being exposed to the field. But, if the conductor is already in a magnetic field when cooled, the field remains trapped inside due to its property known as ‘flux trapping ‘. (See Fig. 7).

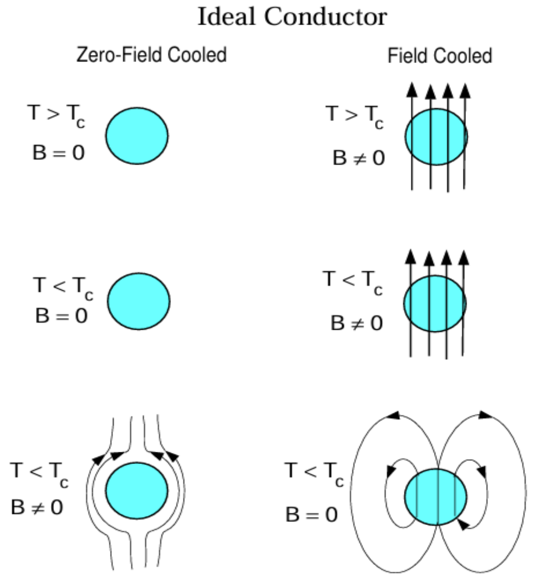

Figure 7 — Magnetic field induction in an ideal conductor;" flux trapping"

Superconductors are different from perfect conductors as a static magnetic field will be excluded if the material is cooled below its critical temperature irrespective of its history.

In 1957, physicists John Bardeen, Leon Cooper, and John Schrieffer developed a microscopic theory, known as the BCS Theory, capable of describing the generation of the superconducting state. BCS theory explains how, at low temperature, electrons in a superconductor form Cooper pair, through their phonon mediated attraction, leading to a collective quantum state. When a conduction electron passes near the ion in the lattice, an attractive interaction occurs due to the opposite charges of the two particles. The ion, which at equilibrium is at equal distances from surrounding ions, shift towards the electron under the influence of this attractive force and pulls some of the surrounding ions towards it. This creates a region of increased positive charge density in the lattice which propagates as an elastic wave possessing momentum and energy. Another conduction electron passing near this region experiences an attractive force due to the positive charge density. As a result, the two electrons experience an overall attractive force mediated through their interaction with the ion lattice as illustrated in Fig. 8. These electrons form a Cooper Pair. Since the binding energy of these electron pairs is weak, thermal agitation can easily break them apart, which is why superconductivity typically occurs at very low temperatures. However, BCS theory cannot fully explain high-temperature superconductivity (HTS), where superconductors remain superconducting at temperatures above 80 K. These materials require alternative theoretical models to describe their mechanisms.[6]

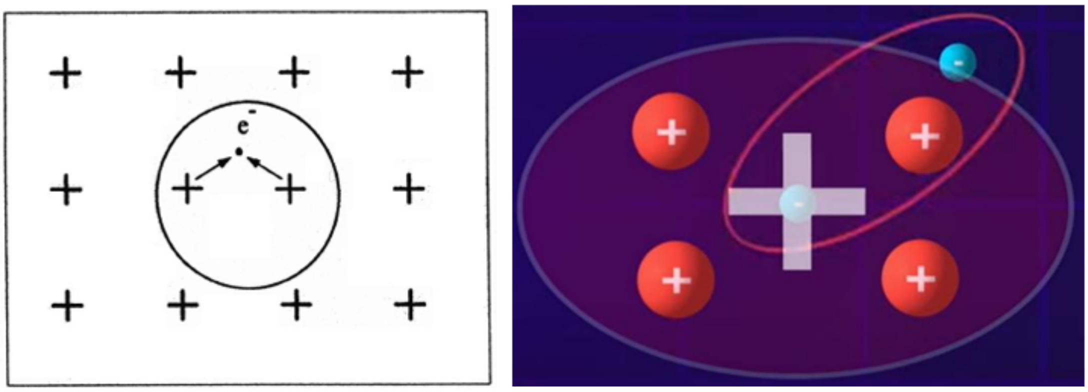

Figure 8- Schematic representation of the formation of a local positive charge density increase in the crystal lattice (left); positive local charge inhomogeneity attracting electrons(right)

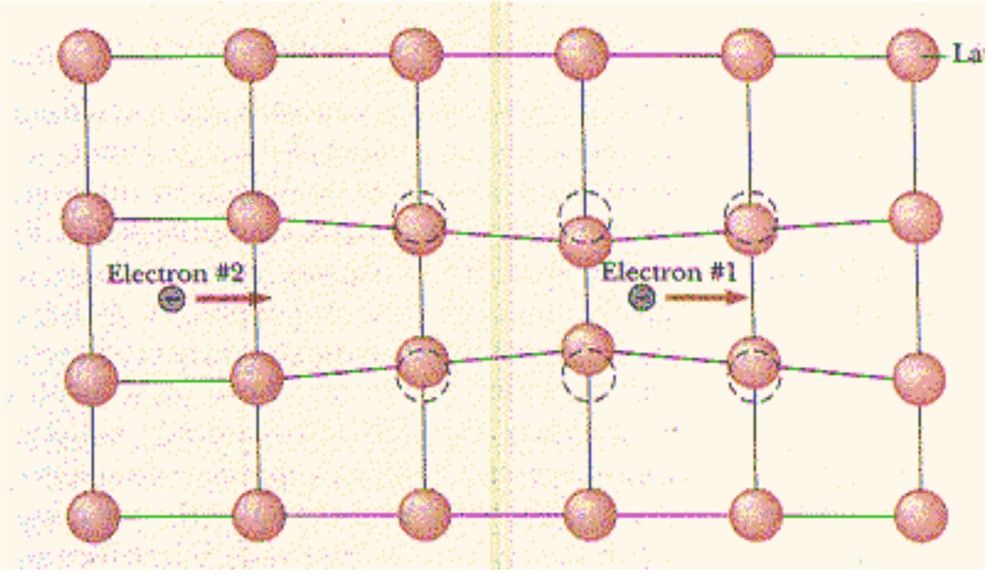

Figure 9 — A Cooper pair moving in a deformed lattice without any loss of energy

Superconductors possess the property of superconductivity only when they remain inside the boundary of '**critical surface'** defined by its critical field, critical temperature and critical current as illustrated in Fig. 10.

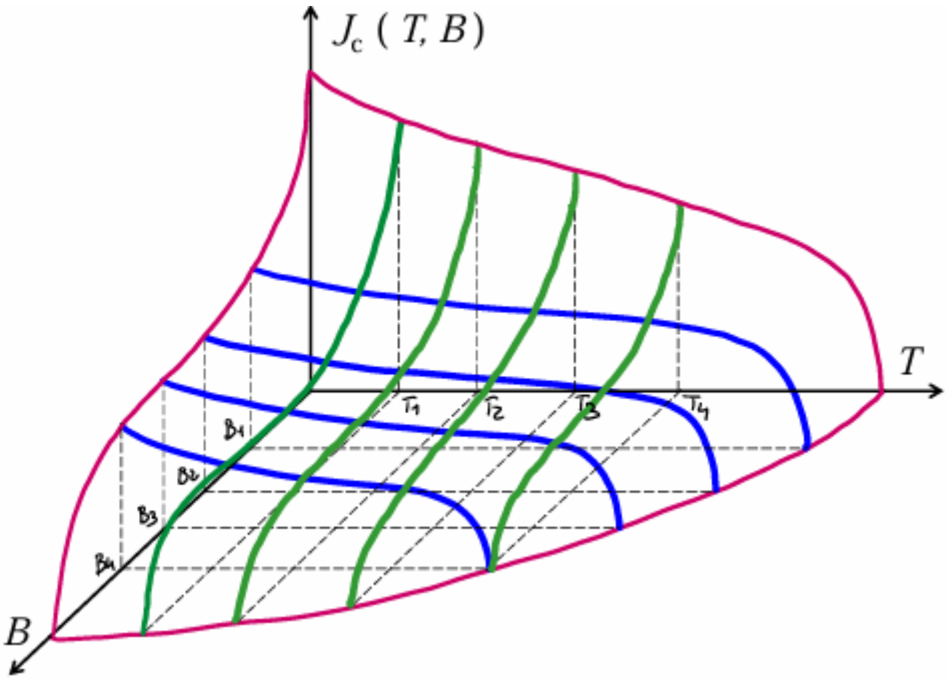

Figure 10 — Superconductivity region diagram; it is bounded by critical current, critical field and critical temperature; each superconductor has a unique critical surface

Superconducting materials can be categorized into two “types” based on their response to magnetic fields and critical temperature. **Type-I superconductors** are usually composed of pure elements (such as Hg, Pb, Sn, Nb). They exhibit lower critical temperatures compared to **Type-II superconductors** and show perfect diamagnetism behaviour below the critical field H_c as shown in Fig. 11. The Type- II superconductors, instead, are composed of metallic alloys (e.g., NbTi, Nb_3Sn, V_3Ga), metal oxides and ceramics (e.g., $YbBa_2Cu_3O_7$, BiSrCaCuO). They exhibit higher critical temperatures and show perfect diamagnetism if the applied external magnetic field remains below the lower critical field H_{c1}. When it exceeds lower critical field H_{c1} but is still lower than the upper critical field, H_{c2}, the material is in a **“mixed state”**, where both superconductive zones and normal zones co-exist. When the external magnetic field exceeds H_{c2}, the material reaches the normal state as shown in Fig. 12.

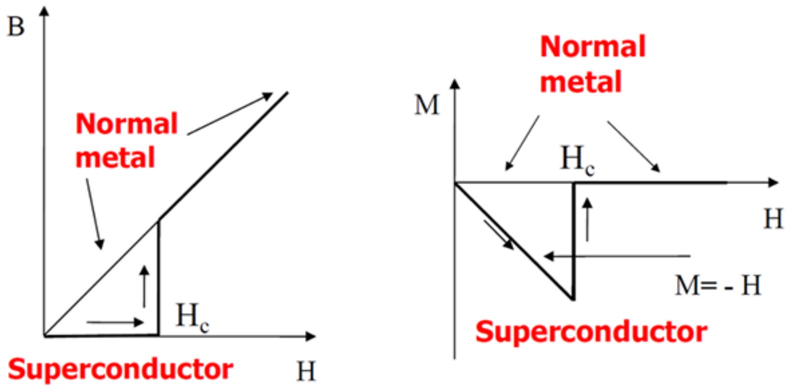

Figure 11- Type 1 superconductors- Transition behaviour with respect to magnetic field induction (left); Transition behaviour with respect to magnetisation (right)

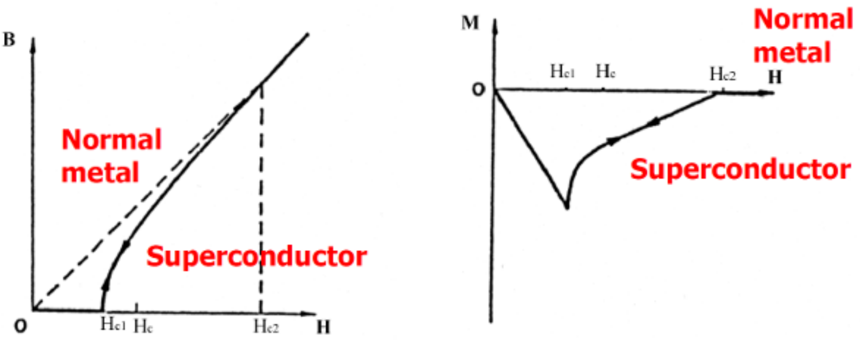

Figure 12-Type II superconductors; Transition behaviour with respect to magnetic field induction (left); Transition behaviour with respect to magnetisation (right)

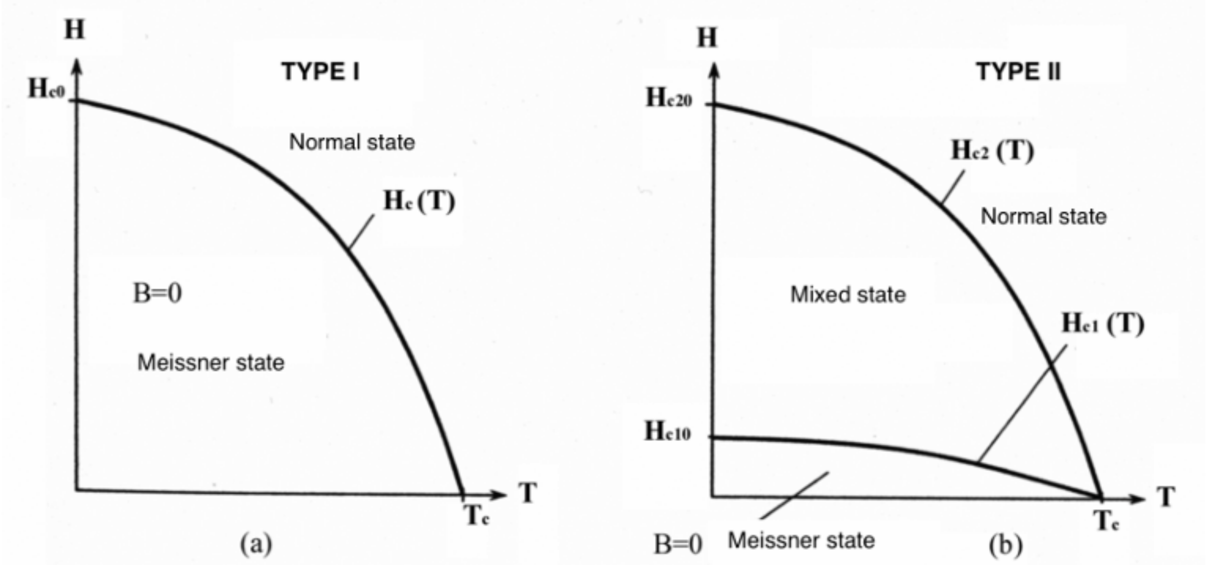

Figure 13- Phase diagram of Type-I (left) and Type-II (right) superconductors. The two graphs are not in scale, Hc1 ≪ Hc ≪ Hc2; Type I superconductors exist only in 2 phases while Type II superconductors exist in 3 phases

HTS materials have a broader critical surface than LTS materials as shown in Fig. 14.

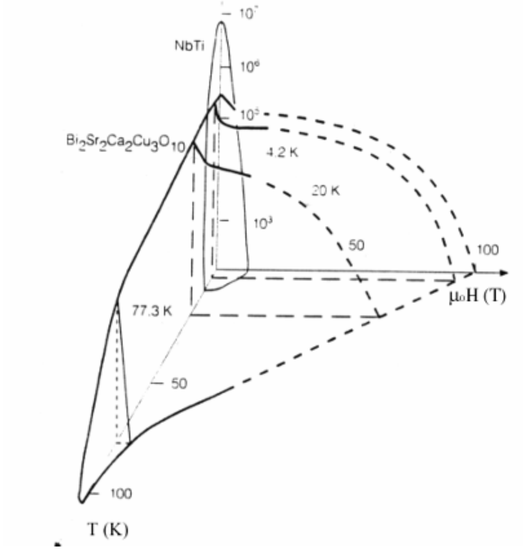

Figure 14- Critical surface of LTS(NbTi) and HTS (BSCCO); NbTi has a narrow critical surface than $Bi_2Sr_2Ca_2Cu_3O_{10}$(BSCCO)

Thereby, the magnets made of HTS materials will retain its superconductivity at higher fields and higher temperatures compared to LTS materials. Applications such as induction heaters, fault current limiters, motors and generators, fusion reactors and magnetic levitation devices employ HTS materials for the same reason [7]. But, in case they are subjected to temperatures and field higher than their critical values, they will *quench*. Quenching is not a problem. Propagation of the quench is our concern.

An essential requirement for the safe and reliable operation of any superconducting magnet is its capacity to tolerate and effectively manage spontaneous quenching, a phenomenon characterized by the abrupt transition of one or more superconducting regions to the normal resistive state. In LTS, quenching leads to a rapid redistribution of current into a metallic stabilizer, typically copper, simultaneously with the development of the normal zone. This zone propagates quickly along the length of the conductor due to the low critical enthalpy of LTS materials. Even a small, local thermal or mechanical disturbance can cause the entire section of an LTS conductor to transition in less than a millisecond. In contrast, HTS materials have a critical enthalpy that is two to three orders of magnitude higher, making them less sensitive to minor disturbances. However, this also implies that normal zones propagate very slowly, which poses significant detection challenges. In HTS conductors, normal zones can arise from localized heating, microscopic pre-existing defects, or gradual mechanical stress over time.

To prevent thermal damage during a quench, several protection strategies are typically employed:

- System de-energization
- Active quench detection
- Use of protection heaters

However, the high critical enthalpy of HTS materials works against conventional voltage-based quench detection systems. Because the normal zone propagation velocity (*NZPV*) is very low, the resulting voltage signal is minimal and difficult to distinguish from background electromagnetic noise.

The electric field E in an HTS conductor during quench can be described by:

$$E = E_c \left(\frac{J}{J_c(T)} \right)^n \qquad \textit{(Eq.8)}$$

where:

- E_c is the minimum experimentally detectable electric field
- J is the current density
- J_c is the critical current density
- n is a parameter depending on temperature, magnetic field, and its orientation

Using this, one can estimate the hot-spot temperature over time. For example, with *n = 40*, the temperature evolution appears as follows:

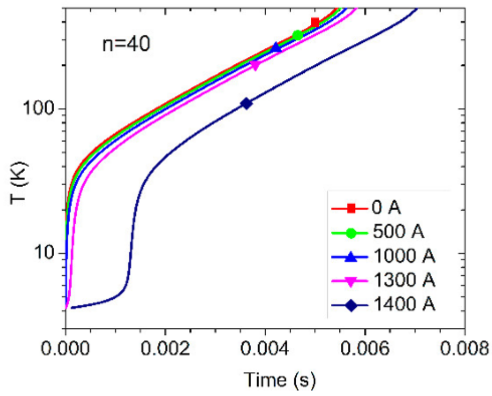

Figure 15 — Hot-spot temperature over time for n = 40

To estimate the voltage generated across the hot spot, we consider *NZPV*. For instance, assuming *NZPV* = 20 mm/s, after 0.0055 s the normal zone spreads 0.11 mm. Combining this with the conductor's resistivity at 500 K yields a voltage drop of only 24 mV.

Such low voltage makes voltage-based detection very difficult, especially since:

- 24 mV is close to the detection limit used in LTS magnets
- Background noise often exceeds this signal
- System validation and shutdown takes time, which cannot be easily reduced due to the magnet's size and stored energy

The typical current decay during a quench extraction follows [8]:

$$I(t) = I_0 e^{-\frac{t\left(R_{Magnet}(t)+R_{Dump}\right)}{L}} \qquad \text{(Eq.9)}$$

where:

- R_{Magnet} is the magnet's resistance
- R_{Dump} is the external dump resistance
- L is the inductance

The extraction time constant is:

$$\tau_e = \frac{L}{R_{Magnete}(t)+R_{Dump}} \qquad \text{(Eq.10)}$$

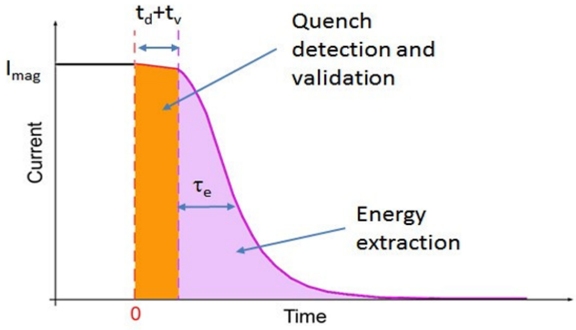

Figure 16 — Current decay during detection, validation, and discharge phases.[8]

where:

- t_d: detection time (depends on system sensitivity and threshold)
- t_v: validation time (hardware-defined)

As L (magnet inductance) scales with system size, τ_e can be reduced by:

- Increasing R_{Dump}, though this raises voltage across the magnet
- Using heaters
- Cabling HTS conductors to reduce inductance and increase operating current

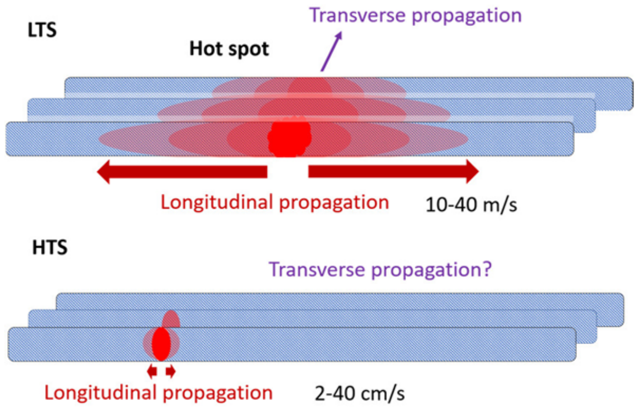

Figure 17 — Comparison of NZPV in HTS and LTS materials. In HTS, longitudinal propagation is slower i.e., of the order 2-40 cm/s[8]

Currently, superconductors are widely used in energy transmission. Due to their nearly zero resistance, they can carry very large currents through smaller sized cables and produce reduced energy waste due to negligible resistive losses. The only drawback, though, is facilitating the cryogenic system which increases the overall cost of the cables. Another promising application of superconductors is in nuclear fusion reactor. A way to deal with the growing energy demands on the horizon 2050, limiting the emission of greenhouse gases is the development of fusion reactors. In Table 1, it is evident that nuclear fusion reactor is a very efficient source of fuel for production of electric power.

1 GigaWatt of electric power requires	2.7 million tonnes of coal
	1.8 Megatonne of petroleum
	25 tons of Uranium (fission reactor)
	350 kg of Deuterium-tritium mix (fusion reactor)
	70 km^2 of solar panels
	3000 x 1 MegaWatt(MW) wind turbines

Table 1 – 1 GW electricity requirement from different sources of fuel.

The largest existing fusion machine is the Joint European Torus (JET) Tokamak, in Culham, UK. It is based on conventional magnets and requires up to 500 MW of electric power. Larger machines, hence, prefer to use superconducting magnets, as they consume less power than conventional magnets. International Thermo Nuclear Experimental Reactor (ITER) was proposed during the Superpower Summit in November 1985 in Geneva, Switzerland. Secretary General of Soviet Union, Gorbatchev, after discussions with French President Mitterrand, proposed to US President Reagan to start a collaboration for the development of fusion energy for peaceful purposes. China, the European Union, India, Japan, Korea, Russia and the United States are **participating** in the decades-long project to build and operate ITER at Cadarache, nearby Aix-en Provence, South of France, and to train the fusion scientists, engineers and operators of the future. The goal of ITER is to achieve **fusion power** production at power plant scale, breaking new ground in fusion science and demonstrating fusion reactor technology. [9]

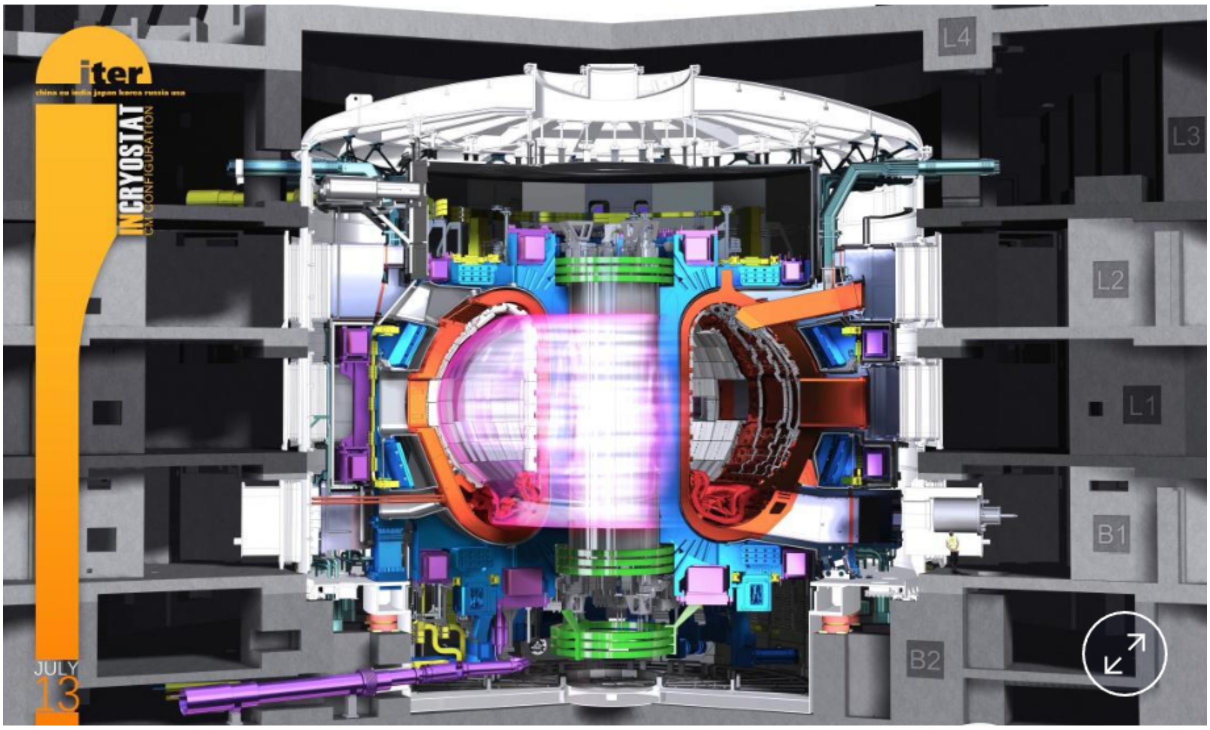

Figure-18-A cross section view of ITER; nuclear fusion reactor of TOKAMAK type; this project is being built jointly by China, the European Union, India, Japan, Korea, Russia and the United States[9]

High-Field Superconducting Magnets is the most common application as they can generate much stronger magnetic fields than conventional ones. A conventional magnet consists of:

- A ferromagnetic core,
- A solenoid that generates the magnetic field when current passes through.

The magnetic field strength B in a solenoid is given by:

$$\vec{B} = \mu_0 \frac{N\vec{I}}{L} \qquad \text{(Eq. 11)}$$

(where N = number of turns, I = current, L = length)

However, an increase in the number of turns N for a constant voltage, increases the length of the wire L, reduces the circulating current I according to Ohm’s Law. A greater wire length results in higher heat generation due to Joule heating.

If, instead of copper wire, superconducting wire is used:

- Joule losses vanish.
- Much higher current can circulate.
- Very intense and stable magnetic fields are produced.

These magnets consist of one or more superconducting wire coils immersed in cryogenic fluid. When energized, they maintain extremely high magnetic fields for long durations with minimal power input.

Today, NHMFL’s magnet design and engineering group is considered the best in the world, supplying cutting-edge equipment not only for research but also for industry and other research institutions globally. As defined by the National Science Foundation (NSF), NHMFL's mission includes:

- Producing high magnetic fields and offering services for scientific research across all disciplines
- Developing user facilities open to all qualified scientists and engineer.
- Advancing magnetic technologies in partnership with industry.
- Promoting a multidisciplinary research environment and running an internal research program to further develop its infrastructure.

It holds the record of building the most powerful hybrid magnet in the world that generates a magnetic field of up to 45.5 T. This magnet is compact and light [10].

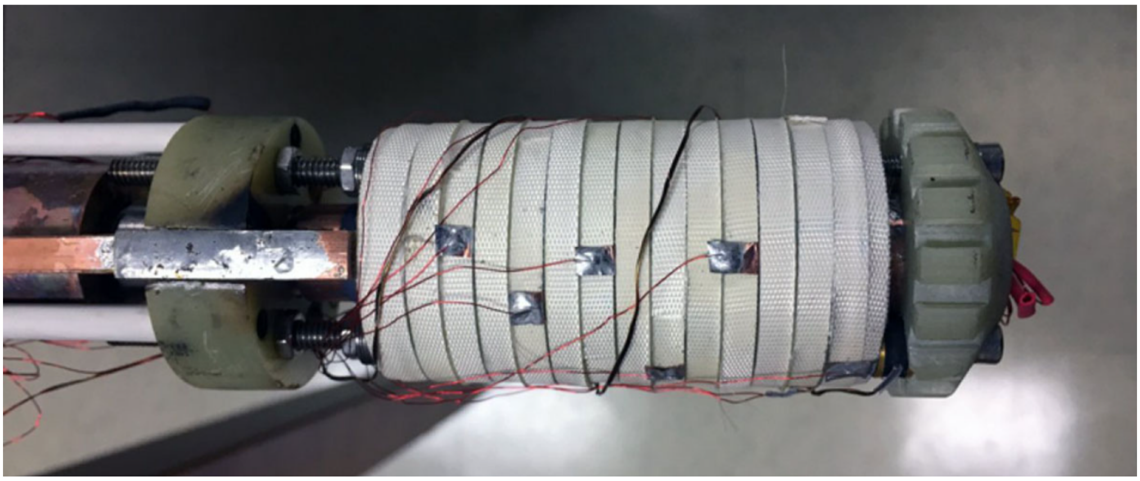

Figure 19 — 45.5 T Hybrid Magnet developed by NHMFL; it is compact and light [10]

The miniature magnet uses REBCO (a compound of rare earths, barium, copper, and oxygen), unlike earlier magnets built from niobium-based superconductors. This new model has many advantages over traditional superconductors:

- REBCO can carry twice the current of niobium-based materials of the same cross-section.
- Since magnetic field strength depends directly on current, this enables stronger magnetic fields.

Additionally, REBCO was fabricated as thin tapes and wound into coils. And most importantly, the coil was not insulated. In typical magnets, insulation ensures that current flows along a controlled path. In this design, no insulation allows the current to bypass local damage and helps avoid quench events. The small superconducting coil was then placed inside a larger resistive magnet, creating a combined field of 45.5 T, with 14.5 T contributed by the superconducting insert.

Superconducting magnets can be configured in different shapes based on its application. Solenoids are the most common configuration for the magnets intended to be tested in high field laboratory. Fig. 20 provides a schematic diagram of a thick solenoid.

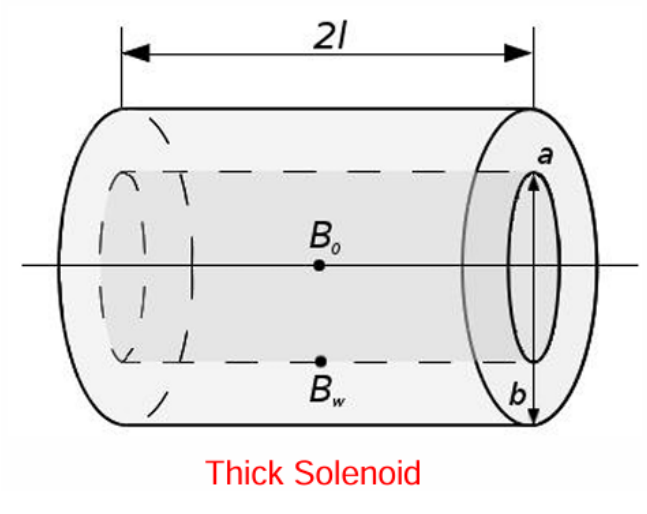

Figure 20-Thick solenoid with inner radius $\boldsymbol{a}$*, outer radius* $\boldsymbol{b}$*, length* $\boldsymbol{2l}$*, field at the centre of the solenoid (*$\boldsymbol{B_0}$*), peak field of the solenoid (*$\boldsymbol{B_w}$*)*

The choice of the appropriate configuration depends on the desired ratio of the peak field (B_w) of the magnet and the field at the centre of the solenoid (B_0), which is crucial for its design and for the definition of the working conditions of the superconductor.

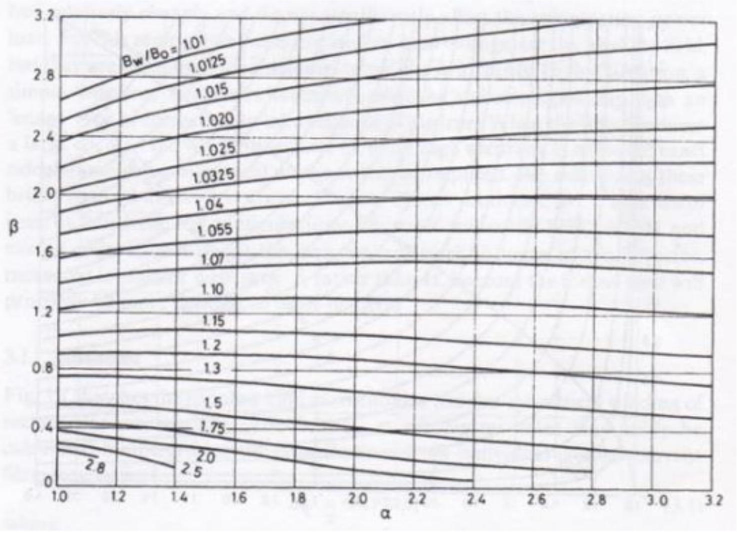

Figure 21- Ratio between the peak field and the field at the center of the solenoid;

$\boldsymbol{\alpha = \frac{b}{a}}$, $\boldsymbol{\beta = \frac{l}{a}}$*[12]*

Fig. 22(a) shows the magnetic field map of a typical thick solenoid winding, and Fig. 22(b) depicts the Lorentz forces when it is energized.

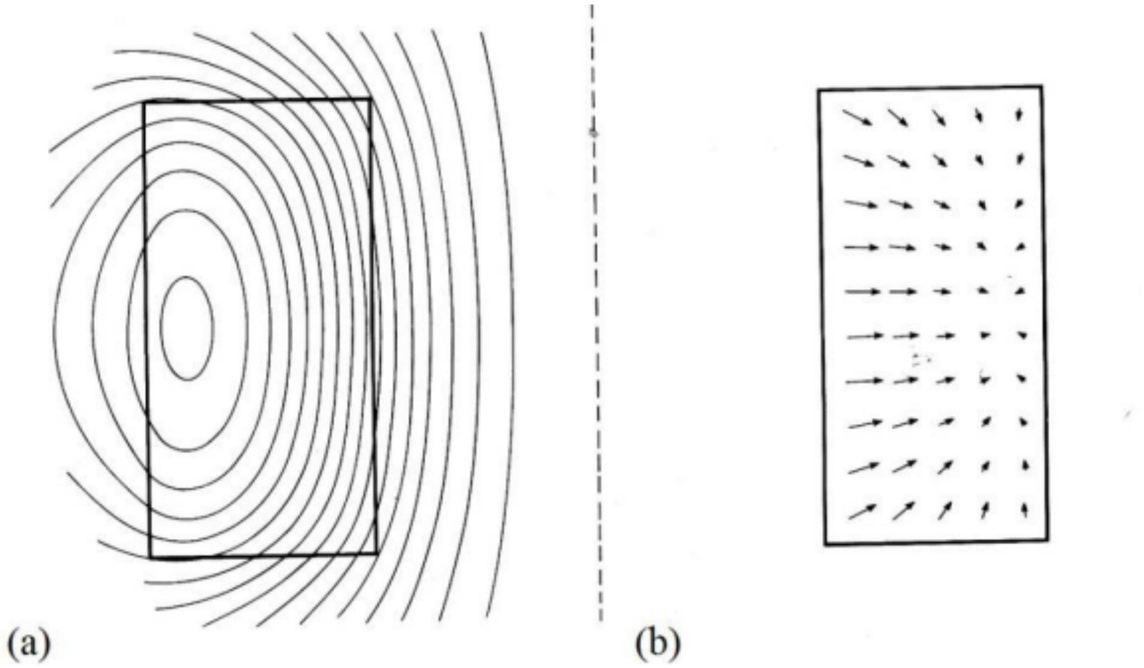

Figure 22- (a) Magnetic field lines created by a thick solenoid winding (b) Lorentz force $(F_L = q(\nu\ B))$ *in the direction by right hand rule; graphs from [12]*

The wall thickness is not negligible compared with the length. The electromagnetic forces (called the *Lorentz force*) tend to push the coil:

- outwards in the radial direction ($F_r > 0$);
- towards the mid-plane in the axial direction ($F_y < 0$ in the upper half coil, and the opposite in the lower half).[11]

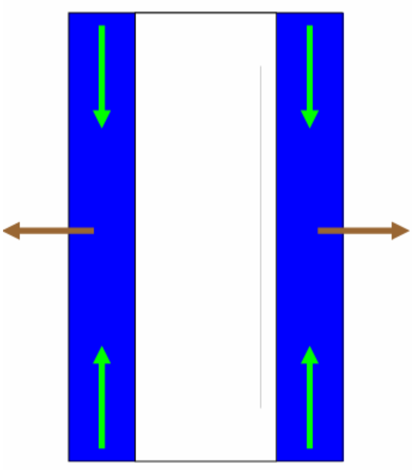

Figure 23 - Lorentz force in the radial direction (brown arrows) pushes the coil outwards and Lorentz force in the axial direction (green arrows) pushes the coil towards the midplane

Since the axial field component changes sign at the outer radius of the winding, the radial component of the force is null and is directed inwards, thus generating small compressive effects on the outer turns of its winding. In this case, if the Lorentz forces are not considered in the design, it will break the coil due to stress.

Solenoids are wound either by layer winding or pancake winding. In layer winding, the solenoid is wound layer by layer, passing from the lower to the upper turns, and from the upper to the lower ones, until each layer is formed. In pancake winding, the solenoid is wound in concentric turns to form thick and short solenoids (*pancakes*) which are then positioned on top of each other and connected in series as shown in Fig. 24.

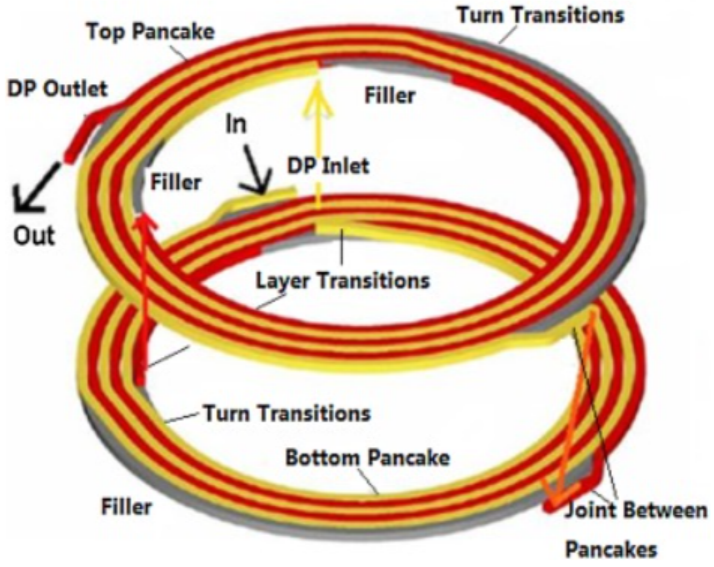

Figure 24 – Double pancake (DP) winding in a solenoid [13]

Windings could be made of either LTS wires or HTS tapes. HTS tapes can carry high current densities even at field strengths of 30 T and due to the Hastelloy substrate, severe mechanical stresses are tolerable. Recently available in long lengths, they are now studied in several research projects, especially for high field magnet applications [15]. This thesis mentions rare earth barium copper oxide called REBCO HTS tapes. The most well-known rare earth used for REBCO is yttrium because YBCO was the first to be discovered with a critical temperature above 77 K, similar to the liquid nitrogen temperature. This promised a considerable decrease in the cost of superconducting applications. My thesis is based on the magnet that uses a tape made of yttrium, but there are other commercially available tapes, made with different materials such as gadolinium for example. Second generation superconductors are, for now, only commercially available in the shape of a tape with a thickness of 0.1–0.2 mm, width of 4–12 mm and are made of a stack of layers as shown in Fig. 25 [16]. The superconducting layer thickness is about 1 or 2 μm, making up only 1% of the total thickness. The critical radius of curvature is limited by the superconducting layer. It is approximately 6 mm, meaning that if the tape is bent beyond this point, the superconducting layer will be permanently damaged.

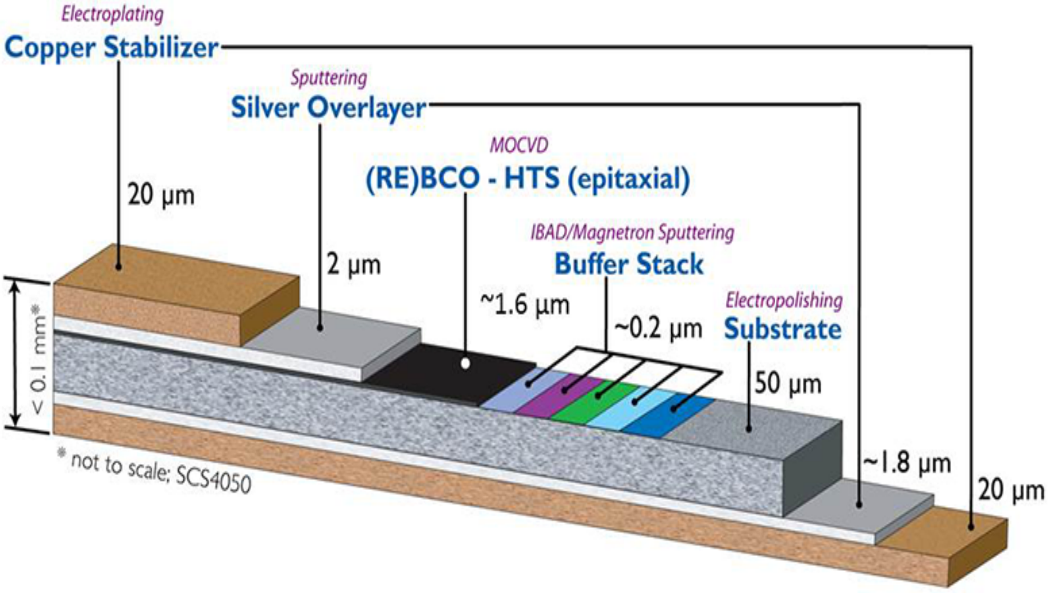

Figure 25 – Schematic of REBCO tape architecture[20]; Each pancake is composed of multiple tapes of REBCO; REBCO tape is manufactured by RABiTS (Rolling Assisted Bi axially Textured Substrates)

High temperature superconductors can carry high currents even under high magnetic field, especially at low temperature. Nevertheless, the critical current decreases with increasing field. It is also highly linked to the orientation of the tape with respect to the field [17]. It is not uncommon that the amount of current carried under transverse field is 1.5–4 times lower than under the same field amplitude but parallel to the tape [18] because REBCO is highly anisotropic i.e., its superconductivity is strongest in a-b planes and weakest in the c plane. Hence, it needs biaxial texturing – both in-plane and out-of-plane alignment. For high critical current, the a-b planes must align along the tape’s length. The most popular method to achieve biaxial texturing is RABiTS (Rolling Assisted Bi Axially Textured Substrates). REBCO is grown epitaxially (atom by atom) on specially prepared textured substrates. A buffer stack is placed between the substrate and the REBCO layer to transfer texturing, and to prevent the chemical reaction between substrate and REBCO.

3. PROBLEM STATEMENT AND METHOD

My work focuses on a computational comparison between experimental data obtained from NHMFL and quench simulations performed at the Department of Electrical, Electronic and Information Engineering (DEI), University of Bologna (UniBO), Italy. A 40 T superconducting magnet with high field REBCO inner coils is under development at NHMFL. Multiple quench tests were performed on the prototype coil named LSC in the year 2024 at 4.2 K, in self-field by activating a set of quench protection heaters. The analysis of the LSC is the subject of this work. It is important to consider a few pre-requisites before delving into the numerical analysis of the LSC magnet in detail. And understanding the 32 T magnet model developed by the University of Bologna in 2016, facilitates better comprehension as it shares multiple methodological similarities with the quench study of the 40 T magnet. This section is divided into 5 parts:

- 32 T NHMFL magnet model and analysis revisited
- LSC Magnet - Geometry
- LSC Magnet – Homogenized Physical Properties of the Magnet.
- LSC Magnet - Magnetic Field and Critical Current computation.
- LSC Magnet – Quench simulations and result analysis

32 T NHMFL MAGNET MODEL AND ANALYSIS REVISITED

The 32 T magnet consisted of:

- an insert (inner magnet), composed of two concentric HTS coils (Coil 1 and Coil 2) and
- an outsert (outer magnet) with LTS coils

The insert was made of YBCO, an HTS material, structured as an ultrathin multilayer tape wound into circular pancakes with a 34 mm central hole.

- Insert Coil 1: consisted of 20 modules i.e. 40 stacked pancakes and capable of generating a total field of 10.7 T
- Insert Coil 2: consisted of 36 modules i.e. 72 stacked pancakes and capable of generating a total field of 6.3 T

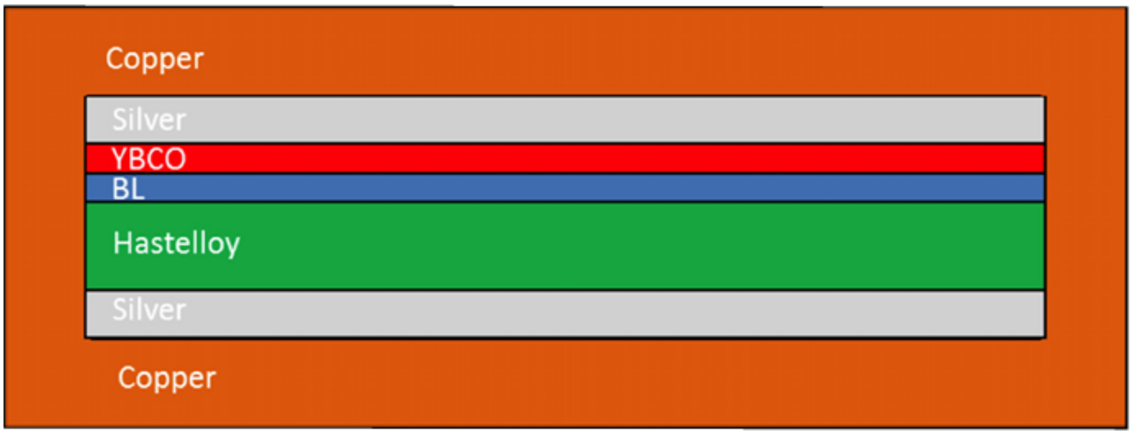

Figure 26— Simplified schematic of the HTS tape layers used in 32 T NHMFL Magnet (not to scale).

The LTS outer winding were provided by the Oxford Instruments, Inc. It consisted of 17 sections operating at 268 A, contributing 15 T to the total magnetic field. (as shown in Fig. 27).

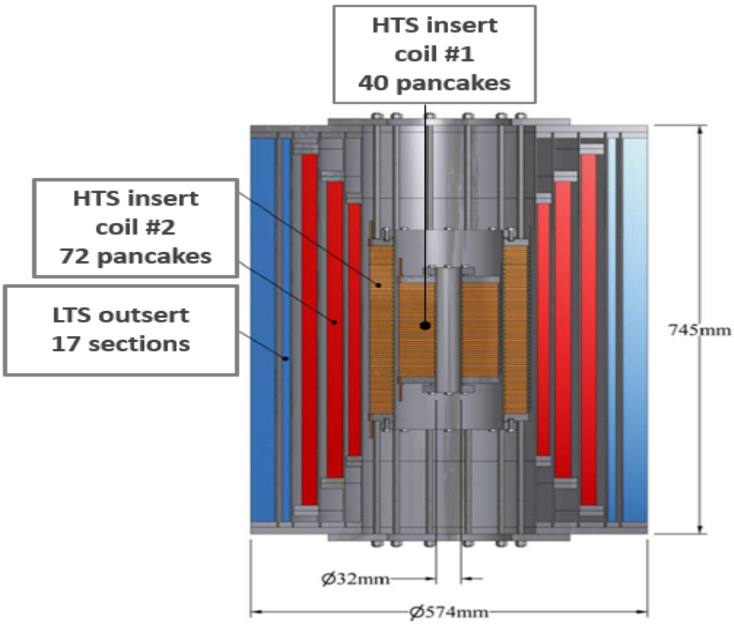

Figure 27 — Structure of the 32T NHMFL magnet [14]

The geometry of the tape is provided in Table 2.

- Insert pancakes were wound with a 4-mm wide YBCO tape co-wound with a sol-gel insulated stainless steel strip as a turn-to-turn insulation;
- Pancakes were separated by a 0.25 mm G-10 insulating layer;
- Heaters were placed between modules (two pancakes = one module), sandwiched between layers of Kapton and G-10;
- Heaters covered only a specific surface region (not the full circumference);
- Each pancake was reinforced with an outer stainless steel band, identical for all pancakes;
- The entire system was kept at 4.2 K.

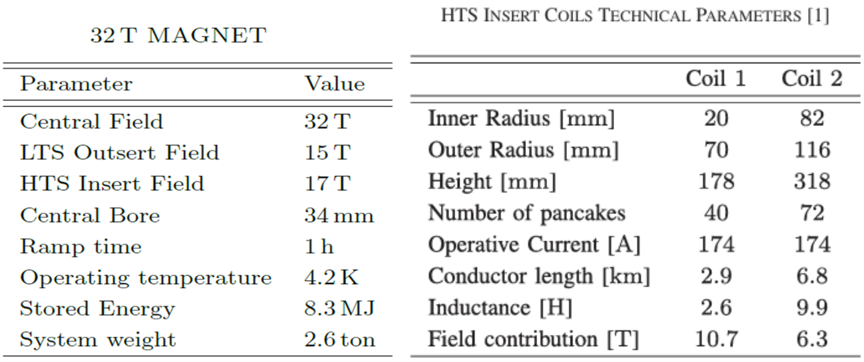

32 T MAGNET

Parameter	Value
Central Field	32 T
LTS Outsert Field	15 T
HTS Insert Field	17 T
Central Bore	34 mm
Ramp time	1 h
Operating temperature	4.2 K
Stored Energy	8.3 MJ
System weight	2.6 ton

HTS INSERT COILS TECHNICAL PARAMETERS [1]

	Coil 1	Coil 2
Inner Radius [mm]	20	82
Outer Radius [mm]	70	116
Height [mm]	178	318
Number of pancakes	40	72
Operative Current [A]	174	174
Conductor length [km]	2.9	6.8
Inductance [H]	2.6	9.9
Field contribution [T]	10.7	6.3

Table 2 — General data of the 32 T magnet and HTS insert coil technical parameters [14]

The LTS outsert quench protection system consisted of both a passive diode-resistor network and an active system of quench detection and power units and quench protection heaters embedded in the winding. The outsert quench protection could also be triggered manually by a TTL signal from the quench detection unit of the YBCO insert. This quench study focused on the HTS insert as, slow quench propagation in HTS could result in localized normal zones thereby leading to Joule heating and potentially transitioning parts of the conductor to resistive state.

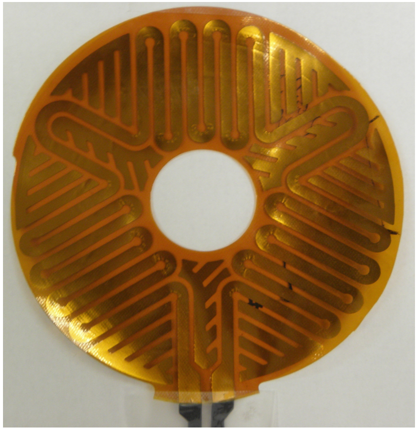

Figure 28 — Heater placement on a pancake [14]

The electromagnetic-thermal quasi-3D Finite Element quench model of the HTS insert coils were coupled with the magnet lumped parameter electrical circuit model. This represented the inductive coupling between the dual coil insert and the multi-section outsert [14].

- Each pancake was modelled in 2D, assuming temperature is distributed uniformly along the axial direction within a given pancake
- A mesh covered only half the pancake, due to symmetry of the solenoid and heater geometry
- Each mesh point solved a heat balance equation (Eq. 12), yielding a temperature vector: $T_i(x, y, t)$ corresponding to time t and to the position of the i-th pancake ($i=1,2\ldots72$) given by the coordinates x, y.[14]

$$\rho(T_i)C_p(T_i)\frac{dT_i(x,y,t)}{dt} - \nabla\cdot(\boldsymbol{k}(T_i)\nabla T_i) = \frac{J^2}{\sigma_i(T_i,B_i,E_i)} + Q_{heat,\ i}(x,y,t) + Q^{cond}_{axial,\,i}(x,y,t) \qquad (Eq.12)$$

$$T = [T_1(x,y,t) \dots T_{72}(x,y,t)] \quad \textit{(Eq.13)}$$

Eq. 12 is the core of any quench simulation as, it equates the heat produced due to its homogenised material properties and the sum of Joules heat, heater heat and heat transfer between layers. The heat balance equation was solved by imposing **adiabatic boundary conditions** for the system and an **initial temperature condition of T=4.2K**. Each of these properties i.e. density (ρ), specific heat (C_p), thermal conductivity tensor (K), electrical conductivity (σ) were derived using tabulated empirical equation. The superconductor was considered homogeneous. Without this assumption, the calculation of these properties would become more complex and time consuming, since it would require discretizing every layer of the superconducting tape [14].

The calculation of the magnetic flux density generated by the prototype coil (self-field) and by the large bore resistive magnet of the NHMFL (background field) were computed through a 3D semi-analytical, numerical approach. The total magnetic flux density is axially symmetric with respect to the prototype coil axis. The radial and axial components of the magnetic flux density vector were computed at each point of the mesh in the finite element discretization during the simulations as shown in Eq. 14 and Eq.15

$$B_i^{r/z}(x,y,t) = b_i^{r/z}(x_i,y_i)I_{op} + \sum_{j=1}^{17} b_{ext,\,j}^{r/z}(x_j,y_j)I_j \quad \textit{(Eq.14)}$$

where:

- $b_{ext,\,j}^{r/z}(t,x,y)$ = coefficients accounting for the field of the outsert on the insert computed for each mesh point
- I_j = current flowing through the outsert
- b^r, b^z = coefficients accounting for the self-field of the insert computed for each mesh point
- I_{op} = current flowing through the insert

$$B_i = [B_i^r(x,y,t),\ B_i^z(x,y,t)] \quad \textit{(Eq.15)}$$

Solving Eq.14 and Eq.15 provided the magnetic field. Its components were used in Eq. 16 to compute the field angle (θ_i). The tape critical current exhibited a strong dependence on the angle θ_i

$$\theta_i = tan^{-1}\left(\frac{B_i^z(x,y,t)}{B_i^r(x,y,t)}\right) \tag{Eq.16}$$

After the magnetic induction field was calculated, it was possible to calculate the electric field. The electric field is useful for the computation of the homogenized electrical conductivity. The electric field was assumed uniform across each layer of the superconducting tape and were modelled in parallel. It was computed as:

$$E = E_c\left(\frac{I_{op}}{I_c}\right)^n = \frac{I_{op}-I_c}{\sum_{i\neq YBCO}\sigma_i(T_i,|\boldsymbol{B}_i|,|\boldsymbol{E}_i|)S_i} \tag{Eq.17}$$

where:

- I_c = critical current
- S_i = surface area of the i-th layer of the tape
- σ_i = electrical conductivity of the i-th layer of the superconducting tape as a function of temperature, magnetic flux density and electric field

The critical current I_c was parameterized as in Eq.18:

$$\mathbf{I_c}(\mathbf{B},\theta) = \frac{\mathbf{b_0}}{(\mathbf{B}+\beta_0)^{\alpha_0}} + \frac{\mathbf{b_1}}{(\mathbf{B}+\beta_1)^{\alpha_1}}\left[\omega_1^2(\mathbf{B})\cos^2(\theta-\phi_1)+\sin^2(\theta-\phi_1)\right]^{-1/2} \tag{Eq .18}$$

where b_0, α_0, b_1, β_1, α_1, ω_1, φ_1 were temperature-dependent parameters

Upon obtaining the electric field, the homogenized electrical conductivity for each pancake, was computed longitudinally, (not radially), as each turn of the superconducting tape was electrically insulated from the rest by a layer of alumina (Al_2O_3) in the radial direction.

$$\sigma_i^{hom} = \frac{I_{op}}{(\Sigma_i S_i)E_i} \tag{Eq.19}$$

The thermal exchange between pancakes in the axial direction was calculated as shown in Eq.20:

$$Q_{axial,i}^{cond} = \frac{T_{i+1}-T_i}{V_p(R_{G10}^{i,i+1}+R_{cz})} - \frac{T_i-T_{i-1}}{V_p\left(R_{G10}^{i,i+1}+R_{cz}\right)} \qquad \text{(Eq.20)}$$

where:

- $Q_{axial,i}^{cond}$ = The heat exchanged between the *i*-th pancake and its adjacent ones
- V_p = pancake volume
- R_{G10} = resistance of G-10 insulation
- R_{cz} = contact resistance between pancakes and G-10 (in series) (shown in Fig. 29)

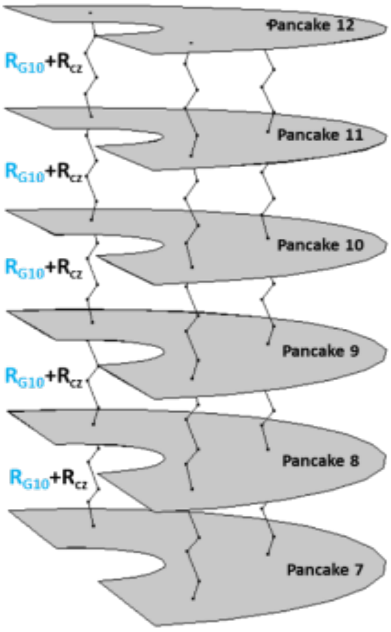

Figure 29 — Conceptual resistance diagram to calculate the heat exchange between pancakes [14]

The constitutive equation of the coil (Eq. 21) describes the system during quench. After the heater activation, the resistance of the HTS coils increases (due to transition of the coils from the superconducting to the normal state) and the current decreases exponentially as in an *LR* circuit. The value of the current and the resistance at each instant of time were calculated using the constitutive equation of the insert setting V_{ground} = 0.

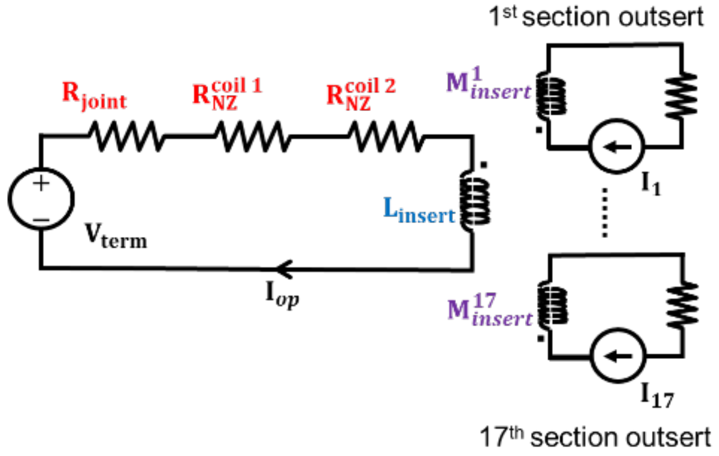

Figure 30 — Equivalent circuit of the solenoid arrangement

$$V_{ground} = \left(R_{NZ}^{coil\,1}(t) + R_{NZ}^{coil\,2}(t) + R_{joint}\right) I_{op} + L_{insert}\frac{dI_{op}}{dt} + \sum_{j=1}^{17} M_{insert}^{j}\frac{dI_j}{dt}$$

(Eq.21)

where $R_{NZ}^{coil\,1}$ and $R_{NZ}^{coil\,2}$ represent the resistances of two HTS insert coils, L_{insert} is the self-inductance of the HTS coils (connected in series), and M_{insert}^{j} is the mutual inductance between the insert and the outsert.

Fig. 31 shows the results obtained by assuming I_{op} (t = 0) = 173 A, and all heaters activated simultaneously with a 0.8 second pulse and a current of 22 A.

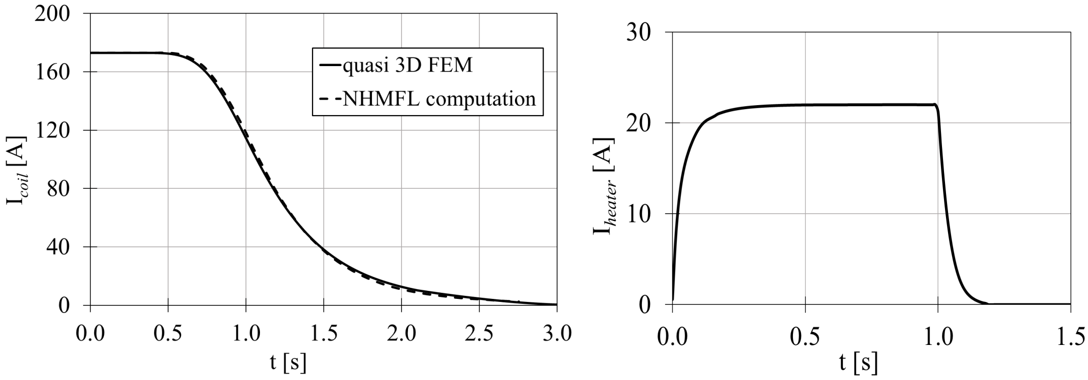

Figure 31 — I_{op} decay and I_{heater} pulse[14]

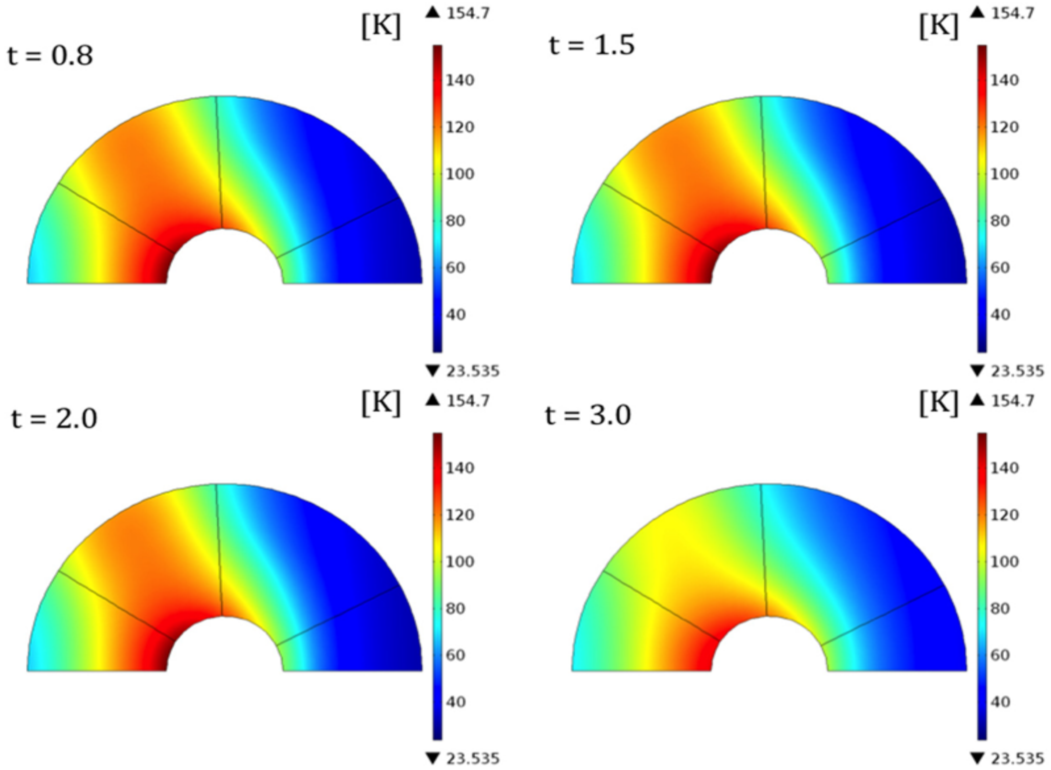

Figure 32 — Temperature distribution in pancake number 8 over time [14]

Based on the observation, the temperature reached a value of 150 K from 4.2K - in some regions of the pancakes, as soon as the heaters were turned off at t = 1.05 s.

The areas with the highest temperatures correspond to the locations where the heaters are placed, as outlined in Fig. 32 by the radial lines extending to the circular edges.

LSC MAGNET – GEOMETRY

The magnet system consists of two superconducting magnets:

- An HTS insert (High-Temperature Superconductor) composed of 22 modules (1 module = 2 double pancakes)
- An LTS outsert (Low-Temperature Superconductor) surrounding it

The geometric dimensions of the HTS insert are shown in Table 3 and 4.

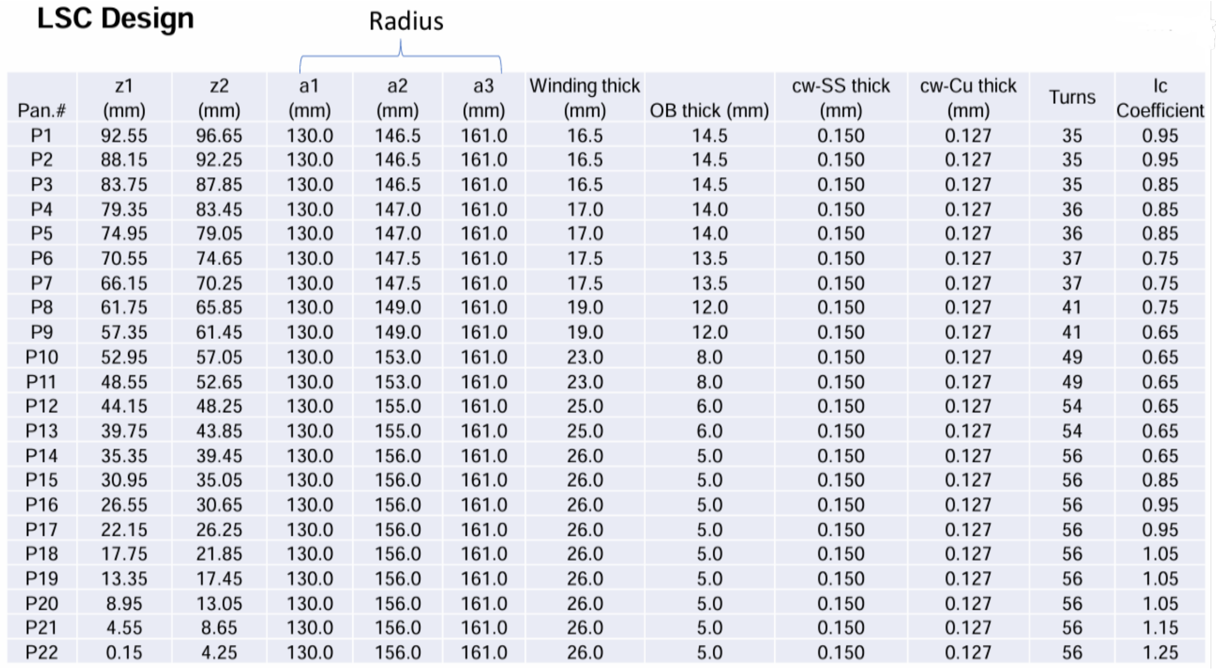

Pan.#	z1 (mm)	z2 (mm)	a1 (mm)	a2 (mm)	a3 (mm)	Winding thick (mm)	OB thick (mm)	cw-SS thick (mm)	cw-Cu thick (mm)	Turns	Ic Coefficient
P1	92.55	96.65	130.0	146.5	161.0	16.5	14.5	0.150	0.127	35	0.95
P2	88.15	92.25	130.0	146.5	161.0	16.5	14.5	0.150	0.127	35	0.95
P3	83.75	87.85	130.0	146.5	161.0	16.5	14.5	0.150	0.127	35	0.85
P4	79.35	83.45	130.0	147.0	161.0	17.0	14.0	0.150	0.127	36	0.85
P5	74.95	79.05	130.0	147.0	161.0	17.0	14.0	0.150	0.127	36	0.85
P6	70.55	74.65	130.0	147.5	161.0	17.5	13.5	0.150	0.127	37	0.75
P7	66.15	70.25	130.0	147.5	161.0	17.5	13.5	0.150	0.127	37	0.75
P8	61.75	65.85	130.0	149.0	161.0	19.0	12.0	0.150	0.127	41	0.75
P9	57.35	61.45	130.0	149.0	161.0	19.0	12.0	0.150	0.127	41	0.65
P10	52.95	57.05	130.0	153.0	161.0	23.0	8.0	0.150	0.127	49	0.65
P11	48.55	52.65	130.0	153.0	161.0	23.0	8.0	0.150	0.127	49	0.65
P12	44.15	48.25	130.0	155.0	161.0	25.0	6.0	0.150	0.127	54	0.65
P13	39.75	43.85	130.0	155.0	161.0	25.0	6.0	0.150	0.127	54	0.65
P14	35.35	39.45	130.0	156.0	161.0	26.0	5.0	0.150	0.127	56	0.65
P15	30.95	35.05	130.0	156.0	161.0	26.0	5.0	0.150	0.127	56	0.85
P16	26.55	30.65	130.0	156.0	161.0	26.0	5.0	0.150	0.127	56	0.95
P17	22.15	26.25	130.0	156.0	161.0	26.0	5.0	0.150	0.127	56	0.95
P18	17.75	21.85	130.0	156.0	161.0	26.0	5.0	0.150	0.127	56	1.05
P19	13.35	17.45	130.0	156.0	161.0	26.0	5.0	0.150	0.127	56	1.05
P20	8.95	13.05	130.0	156.0	161.0	26.0	5.0	0.150	0.127	56	1.05
P21	4.55	8.65	130.0	156.0	161.0	26.0	5.0	0.150	0.127	56	1.15
P22	0.15	4.25	130.0	156.0	161.0	26.0	5.0	0.150	0.127	56	1.25

Table 3 - Geometric data for the double pancake magnet received from NHMFL

Inner radius [mm]	130
Outer radius [mm]	161
Height [mm]	196
Number of pancakes	44
Operative current[A]	645
Inductance[mH]	0.124

Table 4 – Technical parameters of the HTS insert internal coil

The internal coil is made up of 44 stacked pancakes with a total height of ~196 mm. These are alternately separated by:

- A 0.3 mm thick G-10 insulating layer
- A 0.15 mm thick heater, sandwiched between two 0.15 mm G-10 insulating layers

Heaters in the 32T magnet were only placed in the radial area as shown in Fig.28. But in this configuration, the heaters cover the entire surface of each pancake (see Fig. 33). This helps in better distribution of Joules heat after quench initiation. Each pancake also has a variable thickness stainless steel over-band that offers mechanical reinforcement.

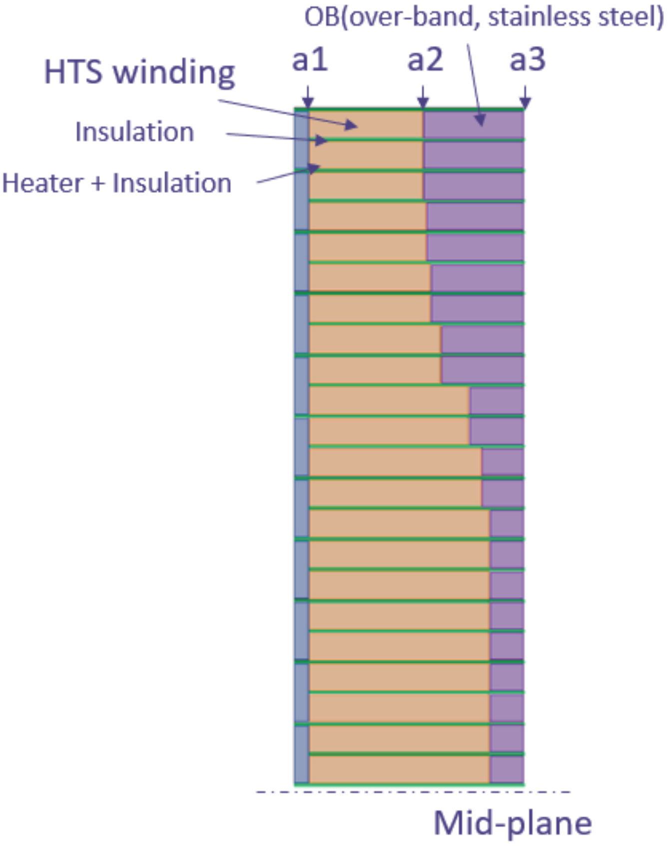

Figure 33 - HTS Half Magnet 2D structure with heater, insulation and over-band details

Each pancake is composed of:

- Two REBCO superconducting tapes (0.095 mm thick each)
- One copper tape (0.127 mm)
- One stainless steel tape (0.15 mm)

Each REBCO tape has the following layers as shown in Fig. 25 and Table 5.

Copper layer	20 μm
Silver overlayer	2 μm
REBCO layer	1.6 μm
Buffer layer	0.2 μm
Substrate layer	50 μm
Silver overlayer	2 μm
Copper layer	20 μm

Table 5 – REBCO tape layers from top to bottom

Each module contains 2 pancakes as shown in Fig. 34.

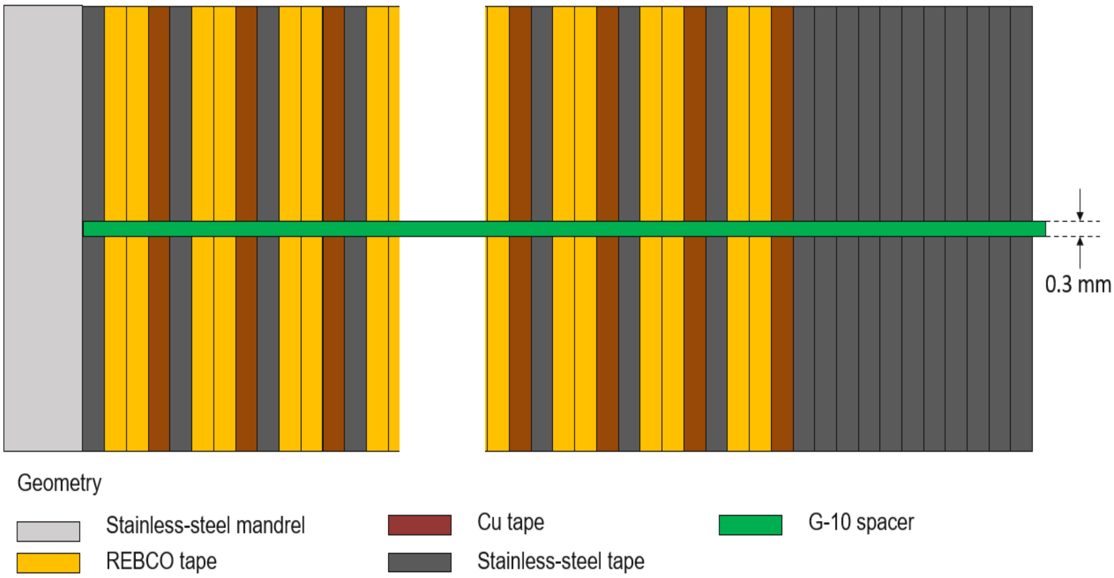

Figure 34 - Module geometry; 2 pancakes; Each pancake has 2 REBCO tapes between a layer of Cu tape and stainless steel tape

A 2D model of this magnet system was built on COMSOL Multiphysics[21]. The COMSOL model of the LSC magnet has some difference with respect to the model of the 32 T magnet described in the previous section. This model is built in cylindrical coordinates (r, z, ϑ) as opposed to the Cartesian coordinate system (x, y, z) used for the 32T magnet model. Text files (*.txt*) of all the geometrical parameters such as *a1, a2, a3, z1, z2* were generated using MATLAB. These *.txt* files were uploaded on COMSOL '*geometry*' tab to build the geometry of the magnet as shown in Fig. 35. Since the magnet geometry has cylindrical symmetry along the z axis and axial symmetry along the r axis, this model can be converted to a 2D $r - z$ plane model in COMSOL, where each pancake is represented as a rectangle. This approach allows the heat balance equation to be solved for a single mesh of points with one temperature value per point, assuming that temperature is uniform over the surface of the pancake. Due to its symmetry across mid-plane, only 22 pancakes are modelled instead of 44 pancakes. Hence, the bottom most pancake in the model represents the middle pancake in the actual magnet.

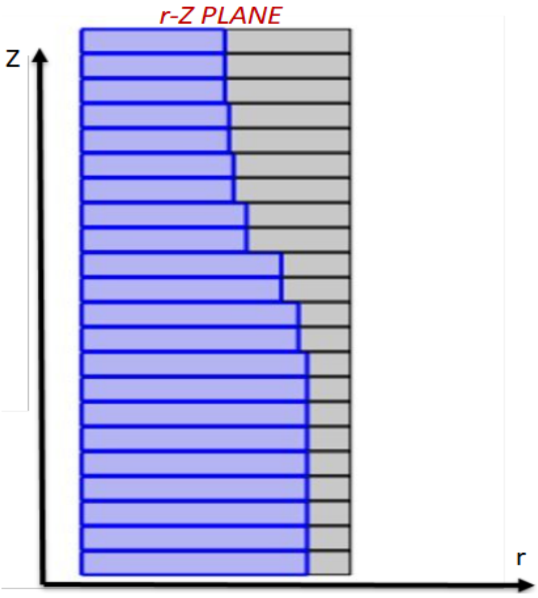

Figure 35 – 2D model of the magnet on $r - z$ plane

LSC MAGNET - HOMOGENIZED PHYSICAL PROPERTIES OF THE MAGNET

The main goal is to solve the heat balance equation in cylindrical coordinates $(r - z)$:

$$\rho(T)C_p(T)\frac{dT(r,z,t)}{dt} - \nabla \cdot (k(T)\nabla T) = \frac{J^2}{\sigma_i(T,B,E)} + Q_{heat,\,i}(r,z,t) \qquad \text{(Eq.22)}$$

where, heat produced due to its homogenised material properties (on left hand side of Eq.22) is equated to the sum of Joules heat and the heater heat (right hand side of Eq.22). The heat balance equation is solved under adiabatic boundary conditions for the system, and an initial temperature condition of 4.2 K. The model uses the following material properties:

- density (ρ)
- specific heat (C_p)
- thermal conductivity (K)

And requires the computation of:

- surface current density (J)
- magnetic field (B)
- electric field (E)

It is assumed that the material is homogenised and anisotropic**.** This simplifies the model and avoids time-consuming discretization of all the tape layers. Material properties for conductor, insulation, stabilizer and support structure are defined using homogenized parameters derived from layered material combinations.

Homogenised specific heat is computed with a MATLAB script using the following equation:

$$C_{p,hom}(T) = \sum_{i=1}^{n} C_{p,i}(T) \cdot \frac{t_i}{t_{TOT}} \qquad \text{(Eq. 23)}$$

where n is the number of layers, and t_i is the thickness of each tape, considering that one winding consists of one stainless steel tape, one copper tape, and two REBCO tapes.

It is important to recall that the REBCO tape itself is composed of several overlapping layers. t_{TOT} is the total thickness, given by the sum of all layer thicknesses, while $C_{p,i}(T)$ is the specific heat of each material, calculated using tabulated empirical equations found in various handbooks.

$$C_{p,REBCO} = g \cdot T^5 + h \cdot T^4 + i \cdot T^3 + l \cdot T^2 + m \cdot T + n \qquad \text{(Eq. 24)}$$

where:

- g, h, i, l, m, n are constants depending on the metal
- $C_{p,REBCO}$ is calculated for a temperature ranging from 4K to 300K.

A data (*.dat)* file named *HomogenizedSpecificHeat* was generated using a MATLAB code that was thereby used as an input to COMSOL definitions.

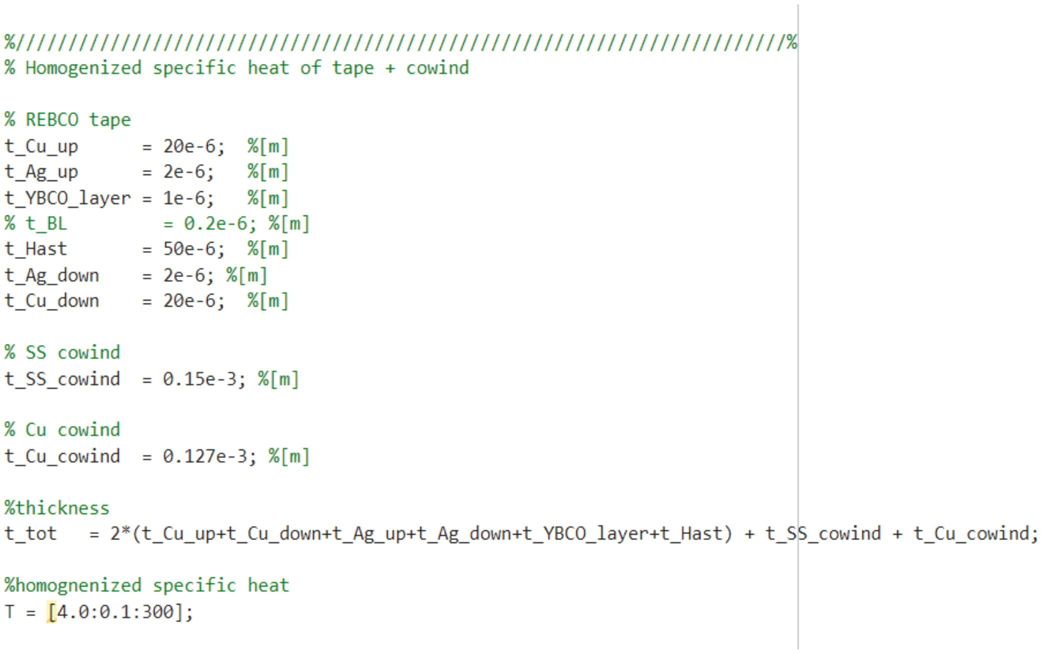

```
%///////////////////////////////////////////////////////////////////////%
% Homogenized specific heat of tape + cowind

% REBCO tape
t_Cu_up      = 20e-6;   %[m]
t_Ag_up      = 2e-6;    %[m]
t_YBCO_layer = 1e-6;    %[m]
% t_BL         = 0.2e-6; %[m]
t_Hast       = 50e-6;   %[m]
t_Ag_down    = 2e-6; %[m]
t_Cu_down    = 20e-6;   %[m]

% SS cowind
t_SS_cowind  = 0.15e-3; %[m]

% Cu cowind
t_Cu_cowind  = 0.127e-3; %[m]

%thickness
t_tot    = 2*(t_Cu_up+t_Cu_down+t_Ag_up+t_Ag_down+t_YBCO_layer+t_Hast) + t_SS_cowind + t_Cu_cowind;

%homognenized specific heat
T = [4.0:0.1:300];
```

Figure 36- MATLAB code for Homogenised specific heat (initial part of code)

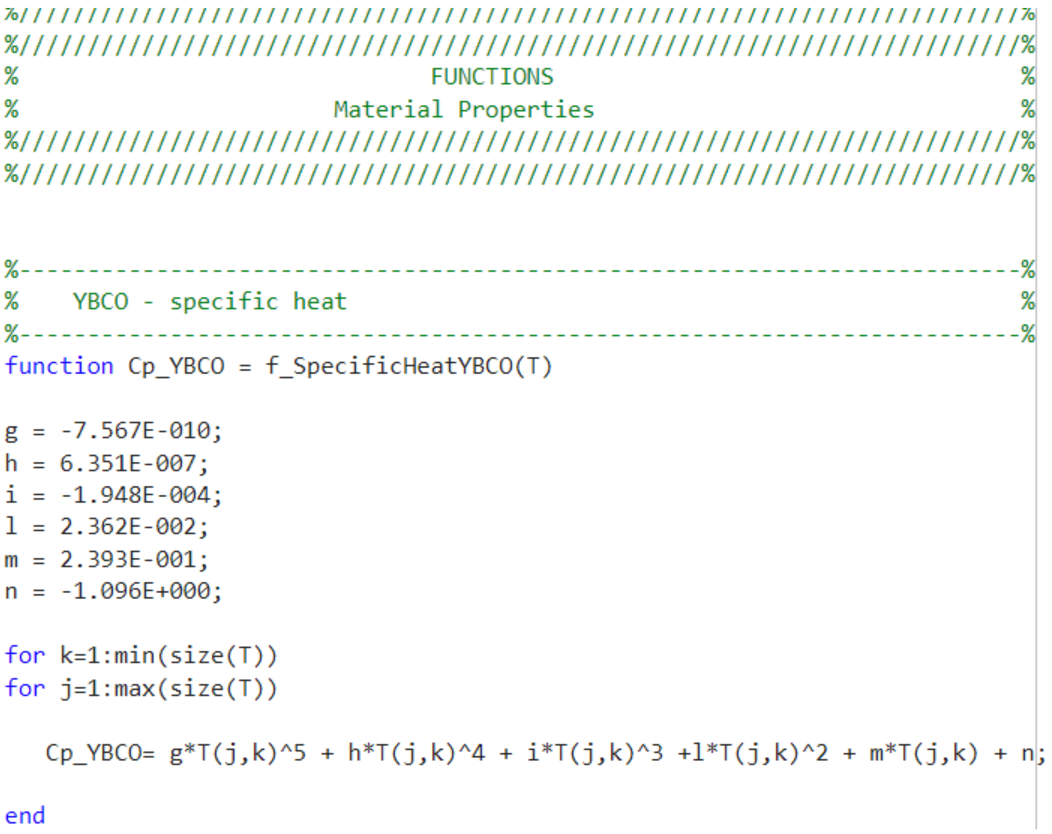

```
%/////////////////////////////////////////////////////////////////////////%
%/////////////////////////////////////////////////////////////////////////%
%                                FUNCTIONS                                %
%                          Material Properties                            %
%/////////////////////////////////////////////////////////////////////////%
%/////////////////////////////////////////////////////////////////////////%


%-------------------------------------------------------------------------%
%    YBCO - specific heat                                                 %
%-------------------------------------------------------------------------%
function Cp_YBCO = f_SpecificHeatYBCO(T)

g = -7.567E-010;
h = 6.351E-007;
i = -1.948E-004;
l = 2.362E-002;
m = 2.393E-001;
n = -1.096E+000;

for k=1:min(size(T))
for j=1:max(size(T))

   Cp_YBCO= g*T(j,k)^5 + h*T(j,k)^4 + i*T(j,k)^3 +l*T(j,k)^2 + m*T(j,k) + n;

end
```

Figure 37- MATLAB code for Homogenised specific heat (specific materials)

Fig. 38 shows the temperature dependence of the homogenized specific heat, which increases sharply with temperature.

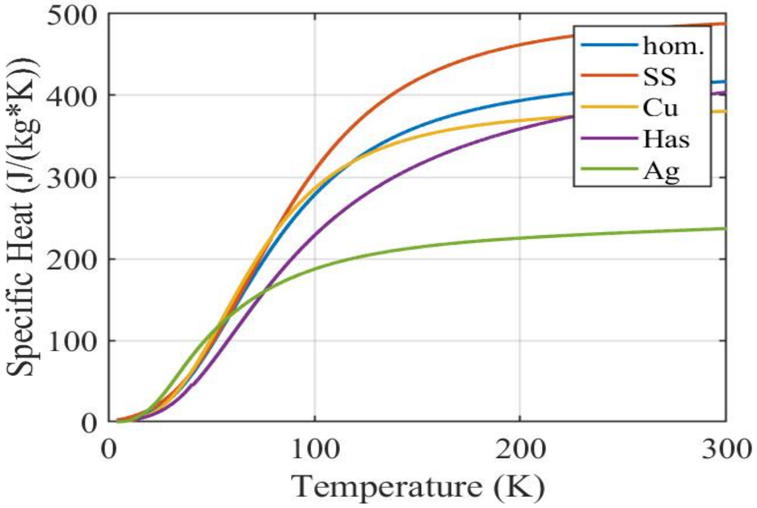

Figure 38 - Temperature dependence of the homogenized specific heat

Homogenised density of each pancake is calculated using Eq. 25:

$$\rho_{hom} = \sum_{i=1}^{n} \frac{t_i}{t_{TOT}} \cdot \rho_i \qquad \text{(Eq.25)}$$

here, ρ_i represents the density of the *i*-th material calculated using tabulated empirical equations. An important clarification is that the temperature dependence of material density has been neglected,

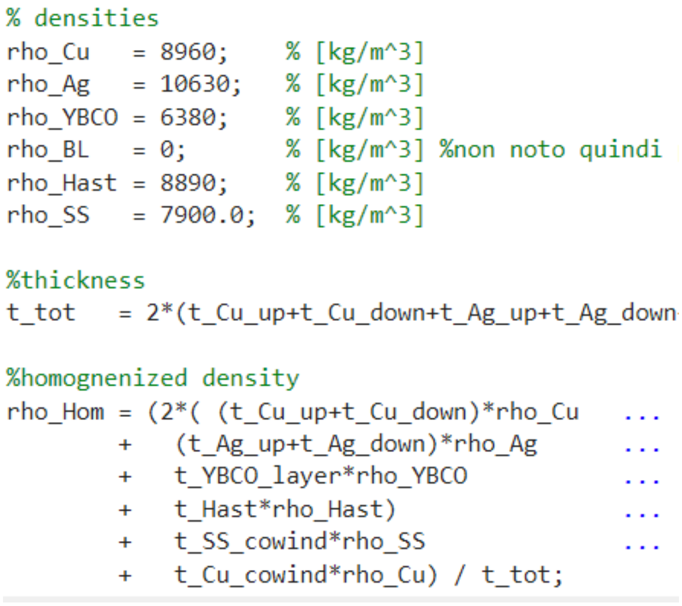

```
% densities
rho_Cu   = 8960;    % [kg/m^3]
rho_Ag   = 10630;   % [kg/m^3]
rho_YBCO = 6380;    % [kg/m^3]
rho_BL   = 0;       % [kg/m^3] %non noto quindi
rho_Hast = 8890;    % [kg/m^3]
rho_SS   = 7900.0;  % [kg/m^3]

%thickness
t_tot   = 2*(t_Cu_up+t_Cu_down+t_Ag_up+t_Ag_down

%homognenized density
rho_Hom = (2*( (t_Cu_up+t_Cu_down)*rho_Cu   ...
        +   (t_Ag_up+t_Ag_down)*rho_Ag      ...
        +   t_YBCO_layer*rho_YBCO           ...
        +   t_Hast*rho_Hast)                ...
        +   t_SS_cowind*rho_SS              ...
        +   t_Cu_cowind*rho_Cu) / t_tot;
```

Figure 39 – MATLAB code of homogenised density

For the calculation of homogenized thermal and electrical conductivities, a distinction was made between the transverse and longitudinal directions relative to the magnet.

Thermal conductivity is highly anisotropic. Longitudinal direction includes contributions from copper and silver. Radial direction is limited by epoxy and other insulating layers.

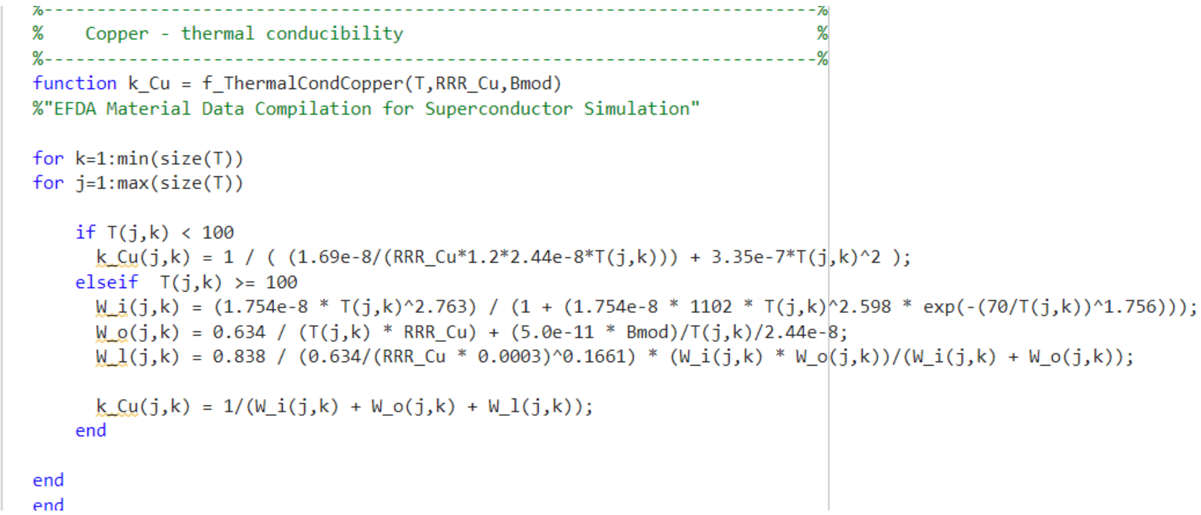

```
%------------------------------------------------------------------------%
%    Copper - thermal conducibility                                     %
%------------------------------------------------------------------------%
function k_Cu = f_ThermalCondCopper(T,RRR_Cu,Bmod)
%"EFDA Material Data Compilation for Superconductor Simulation"

for k=1:min(size(T))
for j=1:max(size(T))

    if T(j,k) < 100
      k_Cu(j,k) = 1 / ( (1.69e-8/(RRR_Cu*1.2*2.44e-8*T(j,k))) + 3.35e-7*T(j,k)^2 );
    elseif  T(j,k) >= 100
      W_i(j,k) = (1.754e-8 * T(j,k)^2.763) / (1 + (1.754e-8 * 1102 * T(j,k)^2.598 * exp(-(70/T(j,k))^1.756)));
      W_o(j,k) = 0.634 / (T(j,k) * RRR_Cu) + (5.0e-11 * Bmod)/T(j,k)/2.44e-8;
      W_l(j,k) = 0.838 / (0.634/(RRR_Cu * 0.0003)^0.1661) * (W_i(j,k) * W_o(j,k))/(W_i(j,k) + W_o(j,k));

      k_Cu(j,k) = 1/(W_i(j,k) + W_o(j,k) + W_l(j,k));
    end

end
end
```

Figure 40 *– MATLAB code for homogenised thermal conductivity of Copper in longitudinal direction*

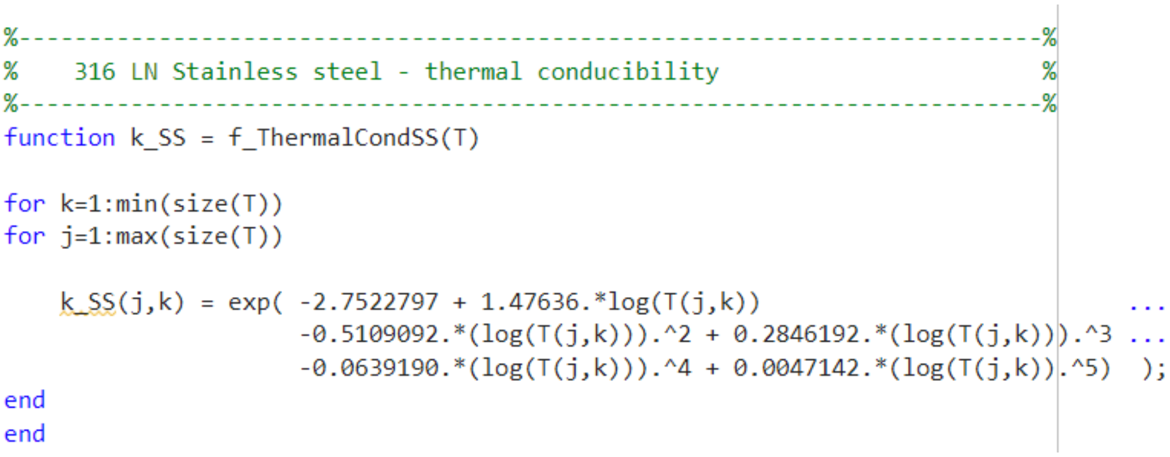

```
%------------------------------------------------------------------------%
%    316 LN Stainless steel - thermal conducibility                     %
%------------------------------------------------------------------------%
function k_SS = f_ThermalCondSS(T)

for k=1:min(size(T))
for j=1:max(size(T))

    k_SS(j,k) = exp( -2.7522797 + 1.47636.*log(T(j,k))                       ...
                    -0.5109092.*(log(T(j,k))).^2 + 0.2846192.*(log(T(j,k))).^3 ...
                    -0.0639190.*(log(T(j,k))).^4 + 0.0047142.*(log(T(j,k))).^5)  );
end
end
```

Figure 41 - MATLAB code for homogenised thermal conductivity of Stainless steel in radial direction

It is calculated in the transverse direction based on considerations of the system, (as shown in Fig. 42). If we consider the heat flux q in the transverse direction, the thermal resistances of each layer of the superconductor can be modelled as being in series shown in Fig. 42:

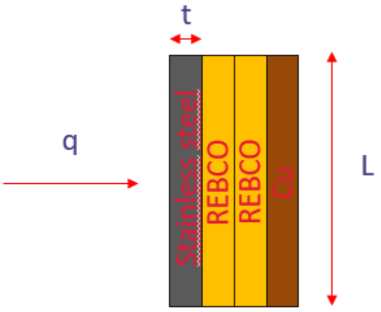

Figure 42- Thermal resistances in series

These properties are pre-dominantly temperature-dependent and implemented into COMSOL using polynomial fits of the form:

The equivalent thermal resistance can be written as

$$R_{eq}(T) = \sum_{i=1}^{n} R_i(T) \qquad \text{(Eq.26)}$$

where n is the number of layers, and $R_i(T)$ is the thermal resistance of the *i*-th layer, which can be calculated using the formula 27

$$R_i(T) = \frac{t_i}{k_i(T)Lw} \qquad \text{(Eq.27)}$$

where t_i is the thickness, L the length, and w the width of a tape, while $k_i(T)$ is the thermal conductivity of the *i*-th layer. While deriving the inverse, we calculate the homogenized transverse thermal conductivity,

$$k_{hom,Trasversale}(T) = \left(\sum_{i=1}^{n} \frac{1}{k_i(T)} \cdot \frac{t_i}{t_{Tot}}\right)^{-1} \qquad \text{(Eq.28)}$$

where:

$k_i(T)$ is thermal conductivity of each material, calculated using tabulated empirical equations based on the same temperature vector considerations as we did for homogenised specific heat and t_{Tot} is the total thickness.

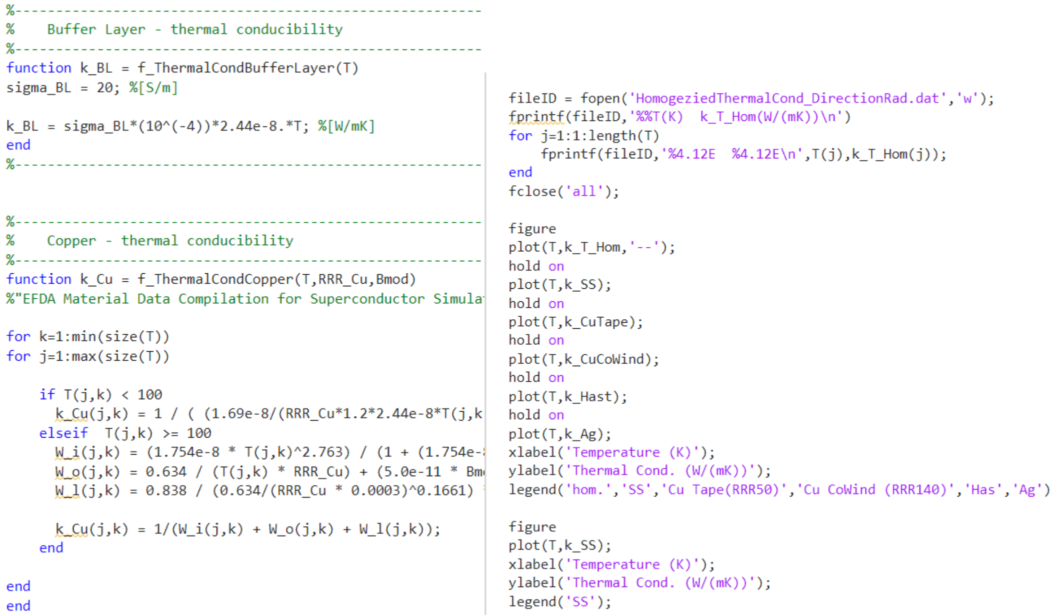

```
%----------------------------------------------------------
%    Buffer Layer - thermal conducibility
%----------------------------------------------------------
function k_BL = f_ThermalCondBufferLayer(T)
sigma_BL = 20; %[S/m]

k_BL = sigma_BL*(10^(-4))*2.44e-8.*T; %[W/mK]
end
%----------------------------------------------------------


%----------------------------------------------------------
%    Copper - thermal conducibility
%----------------------------------------------------------
function k_Cu = f_ThermalCondCopper(T,RRR_Cu,Bmod)
%"EFDA Material Data Compilation for Superconductor Simula

for k=1:min(size(T))
for j=1:max(size(T))

    if T(j,k) < 100
      k_Cu(j,k) = 1 / ( (1.69e-8/(RRR_Cu*1.2*2.44e-8*T(j,k
    elseif  T(j,k) >= 100
      W_i(j,k) = (1.754e-8 * T(j,k)^2.763) / (1 + (1.754e-
      W_o(j,k) = 0.634 / (T(j,k) * RRR_Cu) + (5.0e-11 * Bm
      W_l(j,k) = 0.838 / (0.634/(RRR_Cu * 0.0003)^0.1661)

      k_Cu(j,k) = 1/(W_i(j,k) + W_o(j,k) + W_l(j,k));
    end

end
end
```

```
fileID = fopen('HomogeziedThermalCond_DirectionRad.dat','w');
fprintf(fileID,'%%T(K)  k_T_Hom(W/(mK))\n')
for j=1:1:length(T)
    fprintf(fileID,'%4.12E  %4.12E\n',T(j),k_T_Hom(j));
end
fclose('all');

figure
plot(T,k_T_Hom,'--');
hold on
plot(T,k_SS);
hold on
plot(T,k_CuTape);
hold on
plot(T,k_CuCoWind);
hold on
plot(T,k_Hast);
hold on
plot(T,k_Ag);
xlabel('Temperature (K)');
ylabel('Thermal Cond. (W/(mK))');
legend('hom.','SS','Cu Tape(RRR50)','Cu CoWind (RRR140)','Has','Ag')

figure
plot(T,k_SS);
xlabel('Temperature (K)');
ylabel('Thermal Cond. (W/(mK))');
legend('SS');
```

Figure 43 – MATLAB code for the transversal homogenised thermal conductivity

The homogenized longitudinal conductivity is computed as a weighted average of parallel conductances. Fig. 44 shows the thermal conductivity *vs*. temperature graph, which drops significantly beyond 100 K, especially due to REBCO degradation.

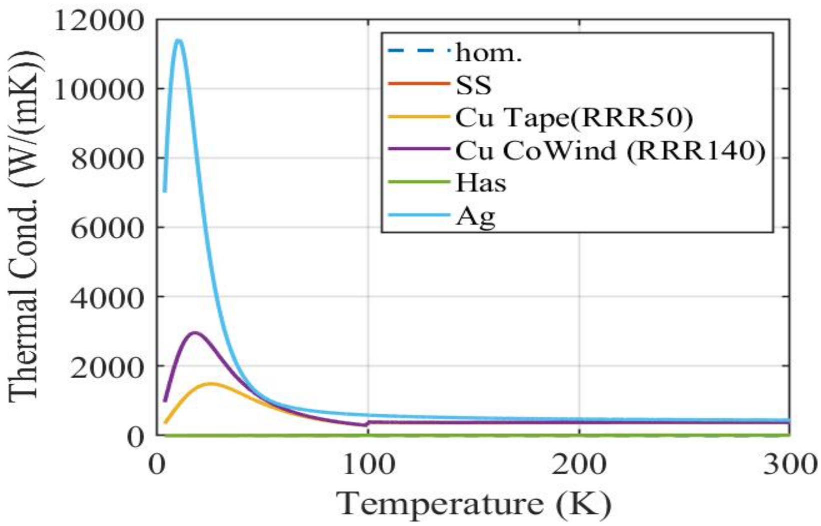

Figure 44- Thermal conductivity vs temperature

Similarly, the system can also be modelled considering the thermal resistances in parallel (as shown in Fig. 44).

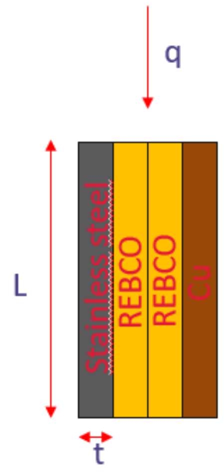

Figure 45 - Conceptual model for thermal resistances in parallel

The final equivalent resistance is calculated by the following equation:

$$R_{eq}(T) = \left(\sum_{i=1}^{n} \frac{1}{R_i(T)}\right)^{-1} \quad \text{(Eq.29)}$$

where $R_i(T)$ is calculated using Eq.27

Similarly, it can be shown that:

$$k_{hom,longitudinale} = \sum_{i=1}^{n} k_i \left(\frac{t_i}{t_{Tot}}\right) \quad \text{(Eq.30)}$$

where thermal conductivity is expressed in terms of temperature

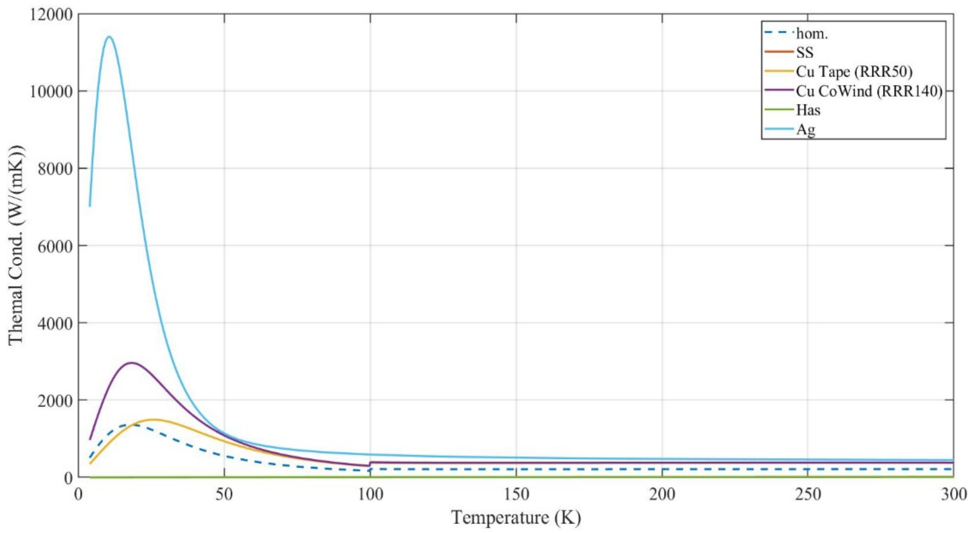

Fig 46- Plot of longitudinal thermal conductivity vs. temperature

In the case of electrical conductivity, it is not calculated in the transverse direction, since each turn is electrically insulated from the others, resulting in a very low value (about 10^{-8} S/m). The electrical conductivity for *Ag*, *Cu* and *Hastelloy* is modelled only in the longitudinal direction and the code is written in *C programming.*

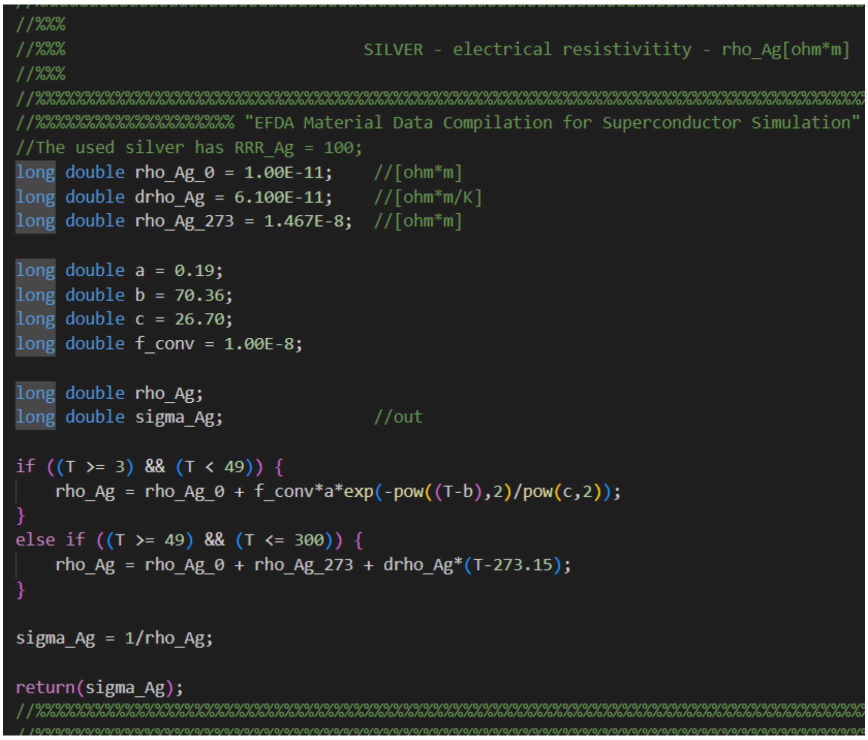

```c
//%%%
//%%%                          SILVER - electrical resistivitity - rho_Ag[ohm*m]
//%%%
//%%%%%%%%%%%%%%%%%%%%%%%%%%%%%%%%%%%%%%%%%%%%%%%%%%%%%%%%%%%%%%%%%%%%%%%%%%%%%%%%%%
//%%%%%%%%%%%%%%%%%%%% "EFDA Material Data Compilation for Superconductor Simulation"
//The used silver has RRR_Ag = 100;
long double rho_Ag_0 = 1.00E-11;    //[ohm*m]
long double drho_Ag = 6.100E-11;    //[ohm*m/K]
long double rho_Ag_273 = 1.467E-8;  //[ohm*m]

long double a = 0.19;
long double b = 70.36;
long double c = 26.70;
long double f_conv = 1.00E-8;

long double rho_Ag;
long double sigma_Ag;               //out

if ((T >= 3) && (T < 49)) {
    rho_Ag = rho_Ag_0 + f_conv*a*exp(-pow((T-b),2)/pow(c,2));
}
else if ((T >= 49) && (T <= 300)) {
    rho_Ag = rho_Ag_0 + rho_Ag_273 + drho_Ag*(T-273.15);
}

sigma_Ag = 1/rho_Ag;

return(sigma_Ag);
//%%%%%%%%%%%%%%%%%%%%%%%%%%%%%%%%%%%%%%%%%%%%%%%%%%%%%%%%%%%%%%%%%%%%%%%%%%%%%%%%%%
```

Figure 47- C code of electrical conductivity of Silver

The calculation of electrical conductivity is performed only in the longitudinal direction, like the method used for longitudinal thermal conductivity. The electrical resistances of the system are modelled in parallel, according to the following equation:

$$R_{eq}(T) = \left(\sum_{i\neq REBCO}^{n} \frac{1}{R_i(t)} + \frac{1}{R_{REBCO}(T)}\right)^{-1} \qquad \textit{(Eq.31)}$$

where $R_i(t)$ is given by the formula:

$$R_i(T) = \frac{L}{\sigma_{i\neq REBCO}(T_i,|\boldsymbol{B}_i|,|\boldsymbol{E}_i|)S} \qquad \textit{(Eq.32)}$$

The final homogenised electrical conductivity can be expressed as

$$\sigma_{hom}(B,E,T) = \sum_{i\neq REBCO}^{n} \sigma_i \cdot \frac{t_i}{t_{Tot}} + \sigma_{REBCO} \cdot \frac{t_{REBCO}}{t_{Tot}} \qquad \text{(Eq.33)}$$

The electrical conductivity of REBCO is calculated differently than the other materials. For the latter, the electrical conductivity is once again obtained from tabulated empirical equations whereas for REBCO, a different and a more complex reasoning is applied bearing in mind, the superconductor tape is made of multiple layers of REBCO and other materials. Starting with electric field given by *power law*,

$$E_z = E_c \left(\frac{J_{REBCO}}{Jc(B,T,\theta)}\right)^n \qquad \text{(Eq.34)}$$

Where E_c, J_{REBCO} ,Jc $(\mathrm{B},\mathrm{T},\theta)$, and n are the critical electric field, the current density in the REBCO tape, the critical current density, and a constant respectively. The critical electric field of HTS is a constant value. E_z can also be written as

$$E_z = \frac{dV}{dz} \qquad \text{(Eq.35)}$$

Upon knowing this value, we can also find the electrical conductivity of REBCO with the following equation:

$$\sigma_{REBCO} = E_Z^{\frac{1-n}{n}} \cdot \frac{J_c}{E_c^{1/n}} \qquad \text{(Eq.36)}$$

Once, σ_{REBCO} is calculated, $\sigma_{\mathrm{hom}}(B,E,T)$ can be calculated. All these equations necessary for the calculation of the physical properties, were implemented in C subroutines linked to COMSOL respectively.

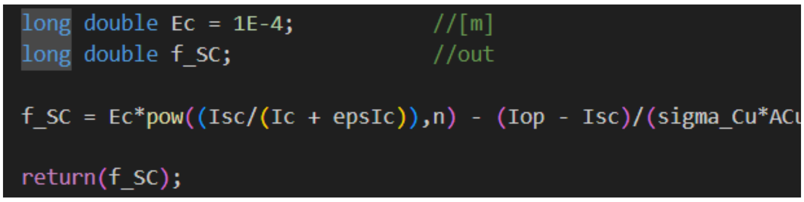

```
long double Ec = 1E-4;              //[m]
long double f_SC;                   //out

f_SC = Ec*pow((Isc/(Ic + epsIc)),n) - (Iop - Isc)/(sigma_Cu*ACu

return(f_SC);
```

Figure 48 - C script for electrical conductivity of REBCO

It is possible to plot the distribution of σ_{REBCO} across the magnet cross-section, as shown in Fig. 49.

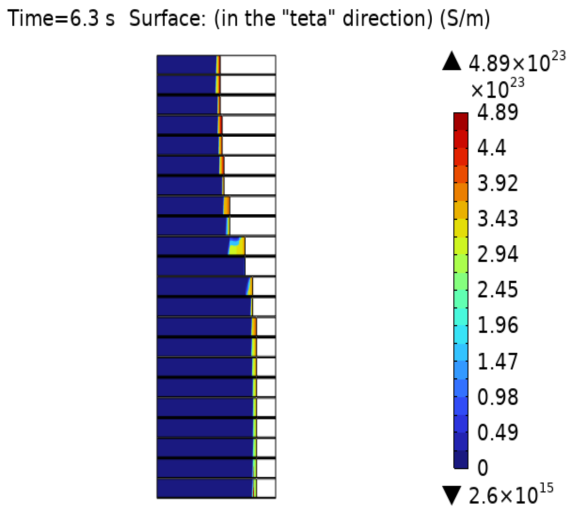

Figure 49 - Conductivity distribution

It can be observed from Fig.49, that the electrical conductivity is extremely high throughout the superconducting material, with a minimum electrical conductivity in the order of 10^{15} S/m.

The output data (*.dat)* files of each homogenised property of the materials are the input to the COMSOL in *'definitions'* for thermal, electrical properties of pancakes, heaters, SS and G10 insulation.

C programs such as *HomSigmaL.c*, *HomSigmaLtest_Ic40Tnew.c*, and others in the *C* function directory perform the calculation of the homogenised electrical conductivity and of the critical current as a function of the field, field angle and temperature. These programs are compiled into dynamic link libraries *(.dll)*, which are then linked to COMSOL as external material functions.

This step ensures that the COMSOL model dynamically updates the electrical conductivity during the simulation based on local field and orientation, improving physical accuracy.

LSC MAGNET - MAGNETIC FIELD AND CRITICAL CURRENT COMPUTATION

The magnetic field was calculated along r and z plane. Initially, the magnetic field was calculated only along the inner edge of the magnet (representing the magnet with its total ampere-turns). This represents the maximum magnetic field in the coil and offers a preliminary understanding of field behaviour. The magnetic field was calculated by two methods - homogeneous and discretized:

1. **Homogeneous model**: Each pancake was represented by a single value at its centre height of the pancake. So, 44 points were considered in total for 44 pancakes.

2. **Discretized model**: In this method, the magnetic field was evaluated at 1 mm intervals along its height

These two methods allow the calculation of coefficients in the radial and zeta direction, named $b^r(t,r,z)$ and $b^z(t,r,z)$ respectively, computed with a reference current of 1 A.
The calculation of the field in COMSOL is then based on the following equations:

$$B_i^r(t,r,z) = b^r(r,z)I_{op}(t) + B_{ext,j}^r(r,z) \qquad \text{(Eq.37)}$$

$$B_i^z(t,r,z) = b^z(r,z)I_{op}(t) + B_{ext,j}^z(r,z) \qquad \text{(Eq.38)}$$

where the radial component $B_i^r(t,r,z)$ and axial components $B_i^z(t,r,z)$ of the magnetic field for each pancake is equal to the product of pre-computed values for each mesh point $b^r(r,z)$ and $b^z(r,z)$ with the operating current of the coil I_{op} . The terms $B_{ext,\,j}^r(r,z)$ and $B_{ext,\,j}^z(r,z)$ include the contribution of the background magnetic field of 11.4 T (from the LTS magnet).

B_i^r and B_i^z are computed given the following geometrical parameters:

- Internal and external radii (RI, RE)
- Pancake centre height (HCOIL)
- Global system height (ZCOIL)
- Operating current

- Number of turns
- Number of evaluation points

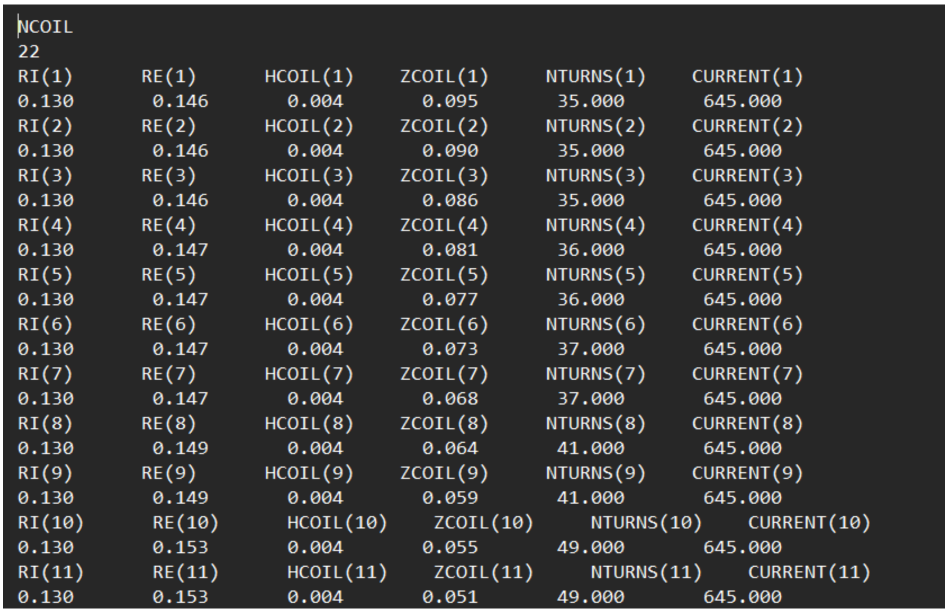

```
NCOIL
22
RI(1)      RE(1)      HCOIL(1)    ZCOIL(1)     NTURNS(1)    CURRENT(1)
0.130       0.146       0.004       0.095       35.000       645.000
RI(2)      RE(2)      HCOIL(2)    ZCOIL(2)     NTURNS(2)    CURRENT(2)
0.130       0.146       0.004       0.090       35.000       645.000
RI(3)      RE(3)      HCOIL(3)    ZCOIL(3)     NTURNS(3)    CURRENT(3)
0.130       0.146       0.004       0.086       35.000       645.000
RI(4)      RE(4)      HCOIL(4)    ZCOIL(4)     NTURNS(4)    CURRENT(4)
0.130       0.147       0.004       0.081       36.000       645.000
RI(5)      RE(5)      HCOIL(5)    ZCOIL(5)     NTURNS(5)    CURRENT(5)
0.130       0.147       0.004       0.077       36.000       645.000
RI(6)      RE(6)      HCOIL(6)    ZCOIL(6)     NTURNS(6)    CURRENT(6)
0.130       0.147       0.004       0.073       37.000       645.000
RI(7)      RE(7)      HCOIL(7)    ZCOIL(7)     NTURNS(7)    CURRENT(7)
0.130       0.147       0.004       0.068       37.000       645.000
RI(8)      RE(8)      HCOIL(8)    ZCOIL(8)     NTURNS(8)    CURRENT(8)
0.130       0.149       0.004       0.064       41.000       645.000
RI(9)      RE(9)      HCOIL(9)    ZCOIL(9)     NTURNS(9)    CURRENT(9)
0.130       0.149       0.004       0.059       41.000       645.000
RI(10)      RE(10)      HCOIL(10)    ZCOIL(10)      NTURNS(10)    CURRENT(10)
0.130       0.153       0.004       0.055       49.000       645.000
RI(11)      RE(11)      HCOIL(11)    ZCOIL(11)      NTURNS(11)    CURRENT(11)
0.130       0.153       0.004       0.051       49.000       645.000
```

Figure 50 – Calculation of radial and axial field based on geometrical parameters as an input

The field magnitude is then calculated as:

$$\vec{B}_i = \sqrt{(B_i^r)^2 + (B_i^z)^2} \qquad \text{(Eq.39)}$$

In the discretized model, the magnetic field is calculated across the entire $r - z$ cross-section of the magnet as before.

$$B_i^r(t,r,z) = b^r(r,z)I_{op}(t) + B_{ext,\,j}^r(r,z) \qquad \text{(Eq.40)}$$

$$B_i^z(t,r,z) = b^z(r,z)I_{op}(t) + B_{ext,\,j}^z(r,z) \qquad \text{(Eq. 41)}$$

In this case, the coefficients $b^r(r,z)$ and $b^z(r,z)$ are computed with a detailed discretization of each pancake as mentioned above.

Fig. 51 shows the field of only HTS insert, without the contribution of the LTS outsert. This figure demonstrates how both methods yield nearly identical results away from the centre. The percentage error does not exceed 2% (see Fig. 52). At the centre of solenoid, though, the error reaches 11% which is expected due to high field gradient and the idealised assumptions in the continuous approximation. The peak field from the HTS insert alone is ~**7** T, centered around pancakes 22 and 23 as shown in Fig. 51.

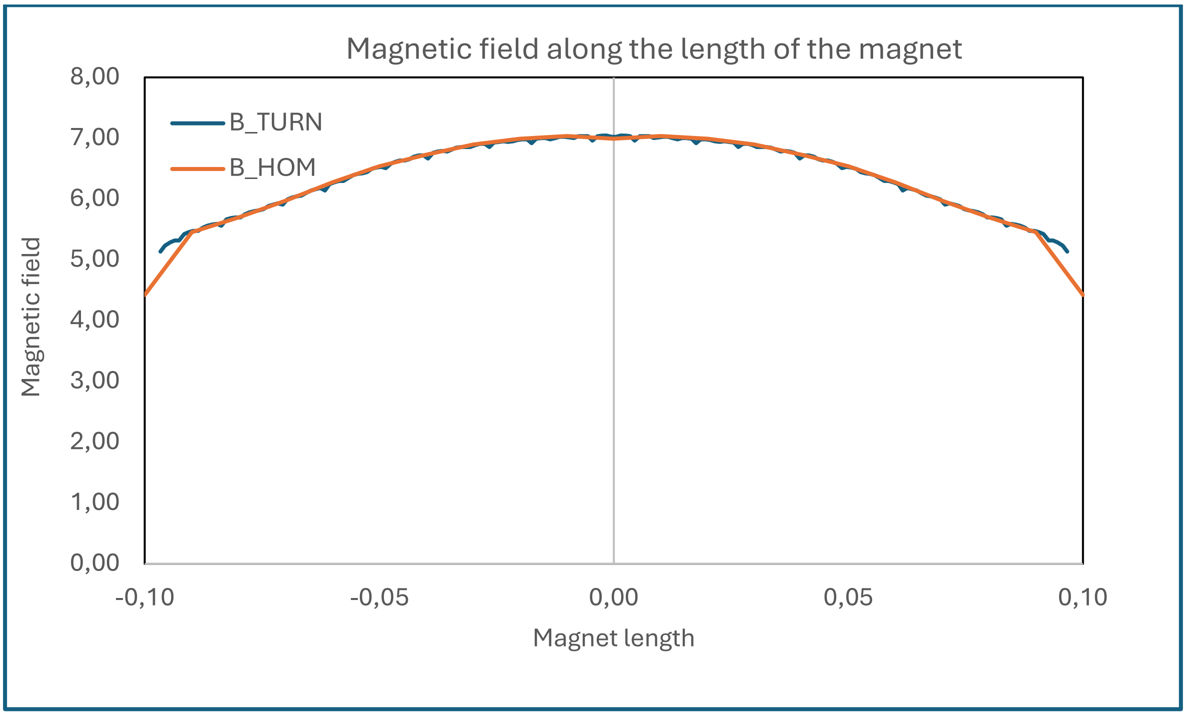

Figure 51 - peak field by homogeneous and discretised model

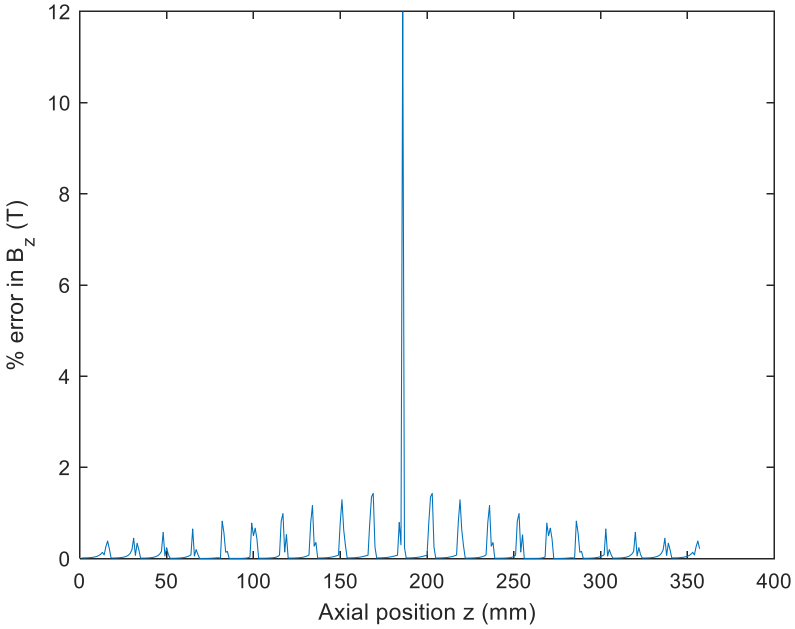

Figure 52- percentage error between homogeneous and discretised model

The calculation of the magnetic field of the insert and outsert are written in the form of a MATLAB code and the output are stored in the *.dat* files *solenoid_insert* and *solenoid_outsert.* These output files are used to calculate $B_i^r(t,r,z)$ and $B_i^z(t,r,z)$with Eq.37 and Eq.38 on MATLAB. Axial and radial magnetic fields produced by both the insert and outsert coils are computed beforehand using MATLAB scripts and analytical tools. These are stored in tabulated *.dat* files such as *BzInsert.dat, BrInsert.dat, BzOutsert.dat, BrOutsert.dat, BzSum.dat* and *BrSum.dat*. These files represent interpolated spatial fields over the mesh grid.

The radial field and axial field are named as *Bper* and *Bpar* respectively and are computed in COMSOL to generate the complete magnetic field distribution.

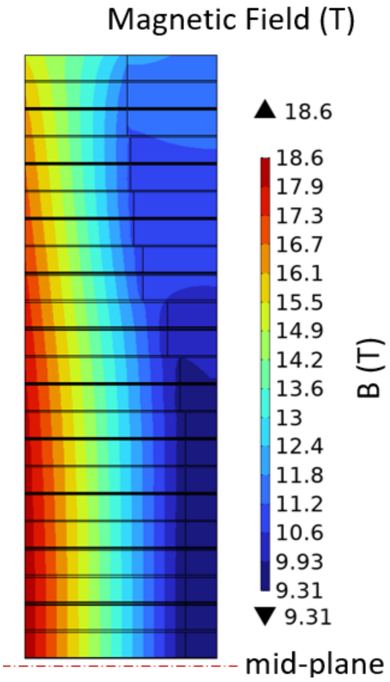

Figure 53- Magnetic field distribution across all pancakes

Fig. 53 shows the resulting field accounting also for the LTS outsert. The highest intensity (~18.6 T) can be observed in the central section of the pancakes (22 and 23).

From the magnetic field calculation, we proceed to calculate the field angle θ_B, the angle between the magnetic field vector and the *z*-axis using the trigonometric equation:

$$\theta_B = atan\left(\frac{B_r}{Bz}\right) \qquad \text{(Eq. 42)}$$

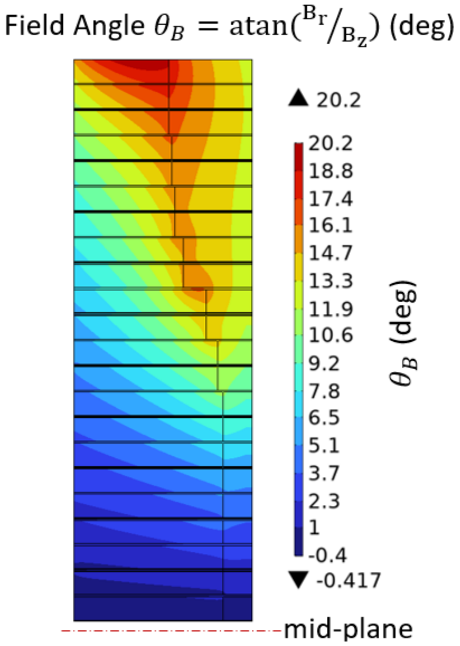

Figure 54- spatial distribution of θ_B with higher angles in the upper-left corner—typical for solenoidal fields.

The critical current (I_C) across the entire superconducting region is computed, excluding the steel over-band (as it is not a superconducting material). Here, the critical current is a function of field, angle and temperature given by the following equation:

$$I_C(B,\theta,T) = I_C(B,\theta,4.2K)\cdot \exp\left(-k(\theta^*)(T-4.2)^{n(T)}\right) \qquad \text{(Eq.43)}$$

where $I_C(B,\theta,4.2K)$ is the critical temperature at 4.2 K and is defined by this equation:

$$I_C(B_a,B_b,4.2\ K) = \frac{I_{CO}}{\left(1+\frac{\sqrt{k^2B_a^2+B_b^2}}{B_0}\right)^{\alpha}}\cdot NC\cdot CF \qquad \text{(Eq.44)}$$

The critical current of each pancake was calculated using the *Kim's* function and the fitting parameters in this equation are provided in Table 6.

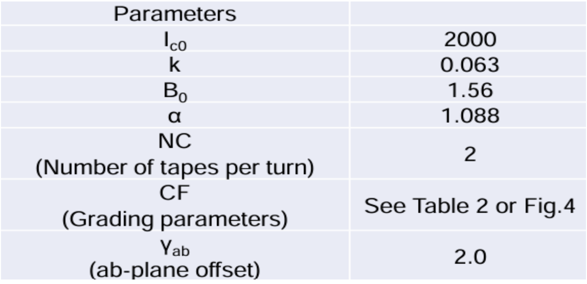

Parameters	
I_{c0}	2000
k	0.063
B_0	1.56
α	1.088
NC (Number of tapes per turn)	2
CF (Grading parameters)	See Table 2 or Fig.4
γ_{ab} (ab-plane offset)	2.0

Table 6 - Fitting parameters to calculate critical current

CF (grading parameter) is the I_c coefficient also mentioned in Table 3.

B_a and B_b are the components of the magnetic field relative to the *ab* offset plane since each tape in the pancake is tilted by an angle (γ_{ab}) $i.e$ 2 degrees as per Table 6. This angle is shown as ϑ_{ab} in the Fig. 55.

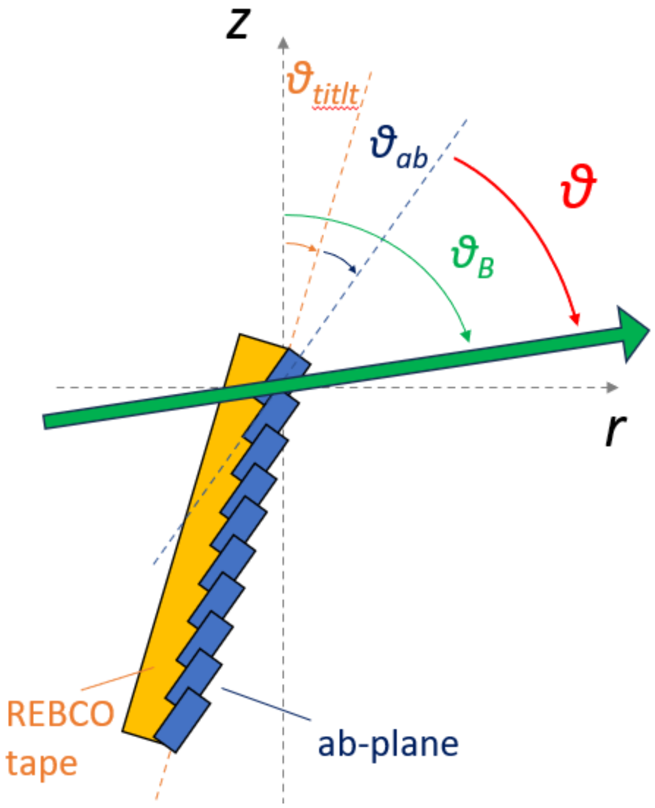

Figure 55- the dependence of current on REBCO tape plane in r-z plane

ϑ_{ab} – the angle of each tape of the pancake with respect to *ab* plane

ϑ_{tilt} – the angle of tilt of the tape with respect to the *z* axis

ϑ_B – the angle between the field and the *z* axis

ϑ - the angle because of the difference of the field angle and the sum of tilt and ab offset angle.

For all practical purposes, we have assumed the ϑ_{tilt} as 0 so that ϑ_{ab} coincides with the angle between z axis and the offset plane. Furthermore, ϑ is the difference between the field angle and the ab offset angle.

$$B_a = B\,cos(\theta_B - \theta_{ab}) \qquad \textit{(Eq.45)}$$

$$B_b = B\,sin(\theta_B - \theta_{ab}) \qquad \textit{(Eq.46)}$$

B_a and B_b are now calculated as per Eq. 45 and Eq. 46.

The *field-angle dependence function* $k(\vartheta^*)$ and the n-value $n(T)$ are computed via empirical fits:

$$k(\vartheta^*) = k1(1.0 - e^{(k2(\vartheta^*+k3))}) \qquad \textit{(Eq.47)}$$

$$n(T) = 2 \quad for\ T < 8K \qquad \textit{(Eq.48)}$$

$$n(T) = n11 + T\big(n12 + T(n13.T + n14)\big)for8\ K < T < 15\ K \qquad \textit{(Eq.49)}$$

$$n(T) = n21 + n22.T(n23 + T(n24 + T(n25.T + n26)))\ \ for\ T > 15\ K \quad \textit{(Eq.50)}$$

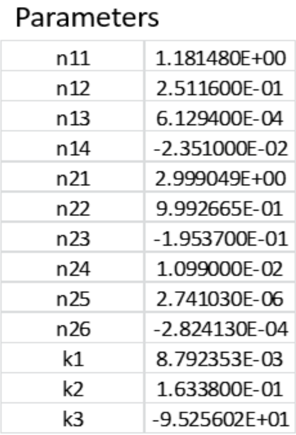

Parameters

n11	1.181480E+00
n12	2.511600E-01
n13	6.129400E-04
n14	-2.351000E-02
n21	2.999049E+00
n22	9.992665E-01
n23	-1.953700E-01
n24	1.099000E-02
n25	2.741030E-06
n26	-2.824130E-04
k1	8.792353E-03
k2	1.633800E-01
k3	-9.525602E+01

Table 7- Empirical fits to solve the critical current

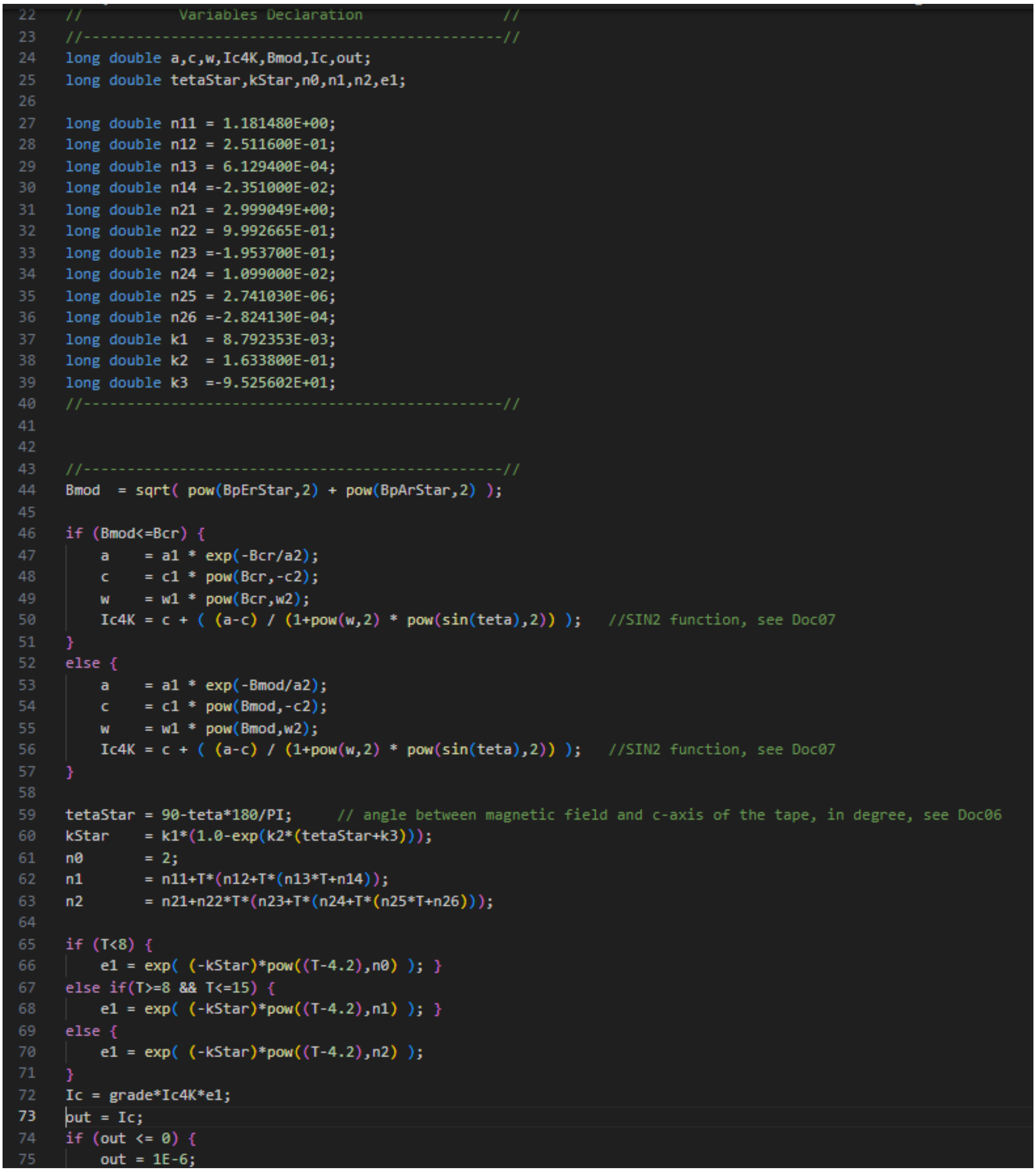

```
//             Variables Declaration               //
//-----------------------------------------------//
long double a,c,w,Ic4K,Bmod,Ic,out;
long double tetaStar,kStar,n0,n1,n2,e1;

long double n11 = 1.181480E+00;
long double n12 = 2.511600E-01;
long double n13 = 6.129400E-04;
long double n14 =-2.351000E-02;
long double n21 = 2.999049E+00;
long double n22 = 9.992665E-01;
long double n23 =-1.953700E-01;
long double n24 = 1.099000E-02;
long double n25 = 2.741030E-06;
long double n26 =-2.824130E-04;
long double k1  = 8.792353E-03;
long double k2  = 1.633800E-01;
long double k3  =-9.525602E+01;
//-----------------------------------------------//



//-----------------------------------------------//
Bmod  = sqrt( pow(BpErStar,2) + pow(BpArStar,2) );

if (Bmod<=Bcr) {
    a    = a1 * exp(-Bcr/a2);
    c    = c1 * pow(Bcr,-c2);
    w    = w1 * pow(Bcr,w2);
    Ic4K = c + ( (a-c) / (1+pow(w,2) * pow(sin(teta),2)) );   //SIN2 function, see Doc07
}
else {
    a    = a1 * exp(-Bmod/a2);
    c    = c1 * pow(Bmod,-c2);
    w    = w1 * pow(Bmod,w2);
    Ic4K = c + ( (a-c) / (1+pow(w,2) * pow(sin(teta),2)) );   //SIN2 function, see Doc07
}

tetaStar = 90-teta*180/PI;     // angle between magnetic field and c-axis of the tape, in degree, see Doc06
kStar    = k1*(1.0-exp(k2*(tetaStar+k3)));
n0       = 2;
n1       = n11+T*(n12+T*(n13*T+n14));
n2       = n21+n22*T*(n23+T*(n24+T*(n25*T+n26)));

if (T<8) {
    e1 = exp( (-kStar)*pow((T-4.2),n0) ); }
else if(T>=8 && T<=15) {
    e1 = exp( (-kStar)*pow((T-4.2),n1) ); }
else {
    e1 = exp( (-kStar)*pow((T-4.2),n2) );
}
Ic = grade*Ic4K*e1;
out = Ic;
if (out <= 0) {
    out = 1E-6;
```

Figure 56 - C code for the critical current computation; variables declaration as per empirical fits; calculation of critical current at 4 K; calculation of the critical current

The critical current is calculated using C and implemented into **COMSOL** through the *.dll* file *HomSigmaLtest_Ic40Tnew* resulting in the critical current distribution as shown in Fig. 57-*left*.

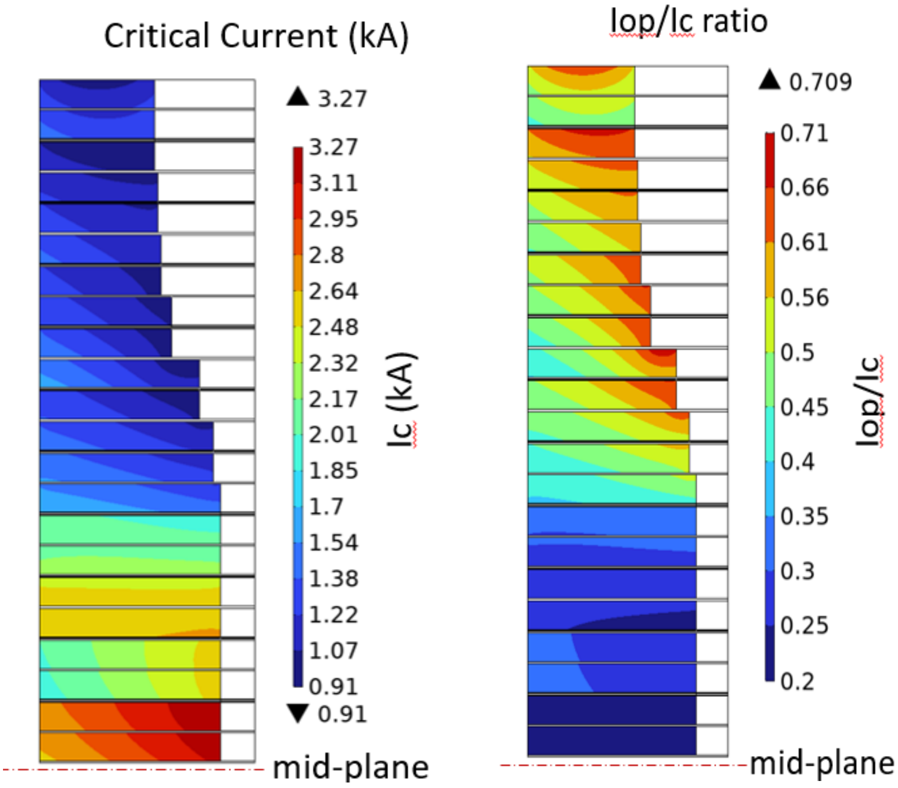

Figure 57- I_c distribution (left); ratio ${}^{I_{op}}/_{I_c}$ (right)

It is important to consider that the highest critical current values correspond to the central pancakes, which is consistent with the field distribution values. The critical current distribution gives an insight to the ratio between operating current and the critical current. This ratio should never exceed 1 as this would mean the material would lose its superconducting properties.

Upon plotting the ratio ${}^{I_{op}}/_{I_c}$ as seen in Fig. 57(*right)* all the values are below 1. This confirms that the material will retain its superconducting properties throughout the operation.

The lowest values of the ratio appear in the central pancakes where the value of I_c is the highest and as we move to the top pancakes, the ratio keeps increasing owing to the decrease of critical current.

The correction coefficients, provided by NHMFL, for the calculation of critical currents for each upper and lower pancake, are tabulated in the Table 8.

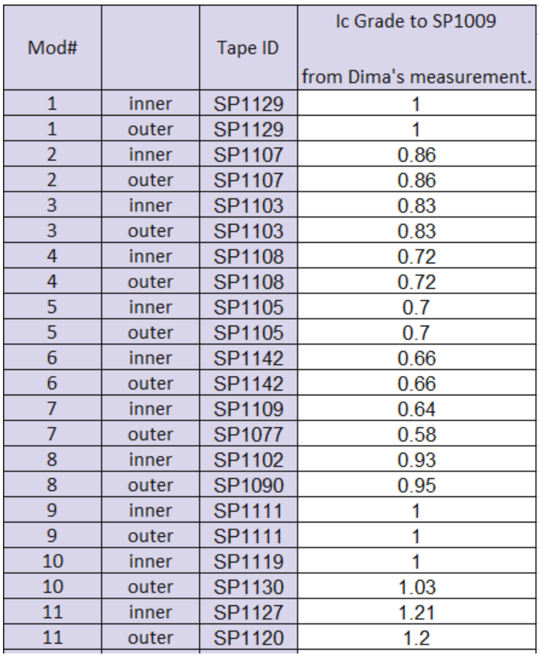

Mod#		Tape ID	Ic Grade to SP1009 from Dima's measurement.
1	inner	SP1129	1
1	outer	SP1129	1
2	inner	SP1107	0.86
2	outer	SP1107	0.86
3	inner	SP1103	0.83
3	outer	SP1103	0.83
4	inner	SP1108	0.72
4	outer	SP1108	0.72
5	inner	SP1105	0.7
5	outer	SP1105	0.7
6	inner	SP1142	0.66
6	outer	SP1142	0.66
7	inner	SP1109	0.64
7	outer	SP1077	0.58
8	inner	SP1102	0.93
8	outer	SP1090	0.95
9	inner	SP1111	1
9	outer	SP1111	1
10	inner	SP1119	1
10	outer	SP1130	1.03
11	inner	SP1127	1.21
11	outer	SP1120	1.2

Table 8 - Correction coefficients of each pancake

Table 9 is a comparison between the critical currents from NHMFL experiments and UniBO simulations. It is observed that the maximum discrepancy is 6.5%, confirming high consistency between both models. To be noted, in this comparison, the correction coefficient has been considered as 1. We will see in the next chapter, the impact of the I_c variation in the quench.

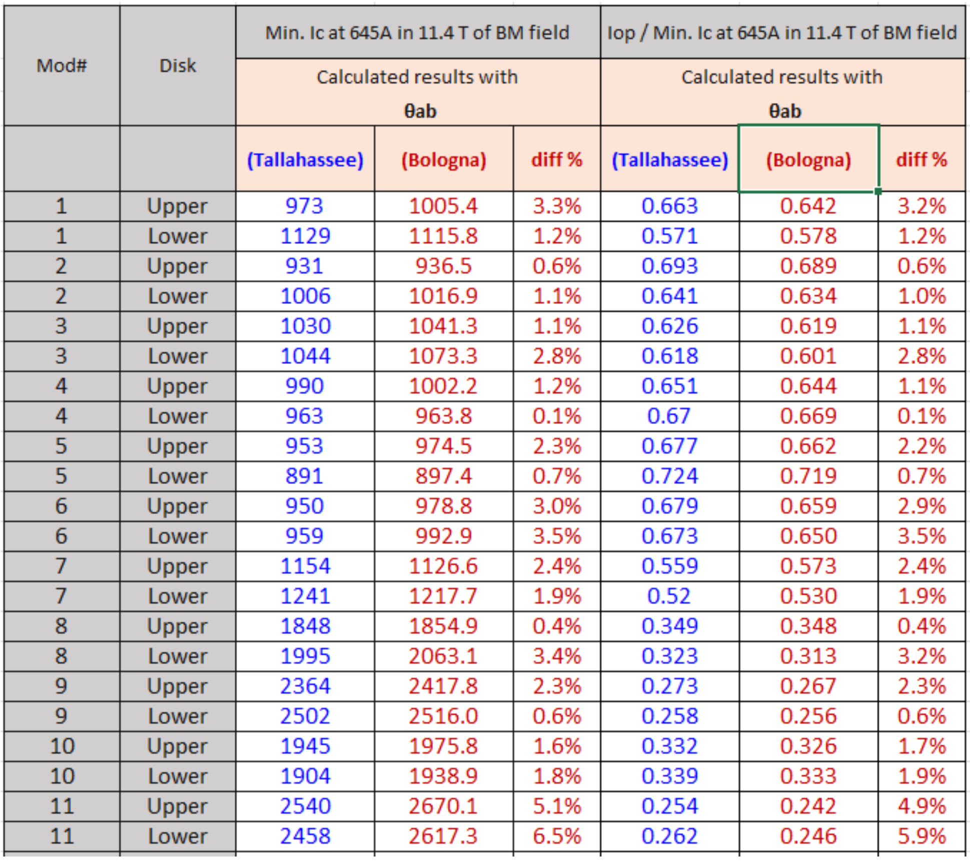

Mod#	Disk	Min. Ic at 645A in 11.4 T of BM field			Iop / Min. Ic at 645A in 11.4 T of BM field		
		Calculated results with θab			Calculated results with θab		
		(Tallahassee)	(Bologna)	diff %	(Tallahassee)	(Bologna)	diff %
1	Upper	973	1005.4	3.3%	0.663	0.642	3.2%
1	Lower	1129	1115.8	1.2%	0.571	0.578	1.2%
2	Upper	931	936.5	0.6%	0.693	0.689	0.6%
2	Lower	1006	1016.9	1.1%	0.641	0.634	1.0%
3	Upper	1030	1041.3	1.1%	0.626	0.619	1.1%
3	Lower	1044	1073.3	2.8%	0.618	0.601	2.8%
4	Upper	990	1002.2	1.2%	0.651	0.644	1.1%
4	Lower	963	963.8	0.1%	0.67	0.669	0.1%
5	Upper	953	974.5	2.3%	0.677	0.662	2.2%
5	Lower	891	897.4	0.7%	0.724	0.719	0.7%
6	Upper	950	978.8	3.0%	0.679	0.659	2.9%
6	Lower	959	992.9	3.5%	0.673	0.650	3.5%
7	Upper	1154	1126.6	2.4%	0.559	0.573	2.4%
7	Lower	1241	1217.7	1.9%	0.52	0.530	1.9%
8	Upper	1848	1854.9	0.4%	0.349	0.348	0.4%
8	Lower	1995	2063.1	3.4%	0.323	0.313	3.2%
9	Upper	2364	2417.8	2.3%	0.273	0.267	2.3%
9	Lower	2502	2516.0	0.6%	0.258	0.256	0.6%
10	Upper	1945	1975.8	1.6%	0.332	0.326	1.7%
10	Lower	1904	1938.9	1.8%	0.339	0.333	1.9%
11	Upper	2540	2670.1	5.1%	0.254	0.242	4.9%
11	Lower	2458	2617.3	6.5%	0.262	0.246	5.9%

Table 9 — Comparison of I_c provided by NHMFL and I_c computed by University of Bologna

.

LSC MAGNET – QUENCH SIMULATIONS AND RESULT ANALYSIS

The heat balance equation in Eq. 22 is coupled with the magnet's constitutive equation Eq.51:

$$V_{ground} = R_{LSC}(t) \cdot I_{op}(t) + L_{LSC}\frac{dI_{op}(t)}{dt} \qquad \textit{(Eq.51)}$$

where:

- V_{ground} = ground voltage (set to 0)
- I_{op} = operating current
- L_{LSC} = total inductance (sum of all mutual inductances)

The total resistance R_{LSC} is computed as in Eq.52:

$$R_{\mathrm{LSC}}(\mathrm{t}) = \frac{1}{I_{op}^{2}(t)} \cdot \sum_{i=1}^{44} \int_{V_i} \frac{J^2(t)}{\sigma_i(t,r,z)}\, dV_i \qquad \textit{(Eq.52)}$$

where:

- J: current density,
- V_i: resistive voltage,
- σ_i: electrical conductivity

Following the calculation of all necessary properties and parameters, it is possible to solve the energy balance equation Eq.22 together with the constitutive equation of the coil Eq.51.

From Eq. 22, the temperature distribution is obtained, while from Equation Eq.51, by setting the ground voltage to zero, it is possible to derive the values of the operating current over time during the discharge phase.

The aim is to evaluate how the system behaves thermally and electrically when a quench event is triggered, and the heaters are activated. This section focuses on the results obtained from multiple quench simulations of the superconducting magnet using the COMSOL model.

All the magnetic field data, geometry coordinates, conductivity profiles, and angle mappings are exported using MATLAB scripts in the *Write* folder. The outputs are formatted into COMSOL-readable *.dat* files using structured mesh definitions from *geometry.dat* and *zcoord.dat*.

The quench is simulated by cutting off the power supply at 0.5 second and activating all the heaters simultaneously for 7.2 seconds. It takes 170 milliseconds for the heaters to reach their maximum heat flux level. There are 21 heaters between 22 modules, one heater per module, where each module contains 2 pancakes as per Fig. 58. Quench triggering is modelled using heater power injection. Time-dependent profiles of heater activation current and resistance are defined in *HeaterCurrent.dat* and *HeaterResistance.dat.*

These inputs are incorporated in the COMSOL model as *heat sources* are applied on specific domains or boundaries. The heater behaviour is crucial for initiating the quench and studying its propagation.

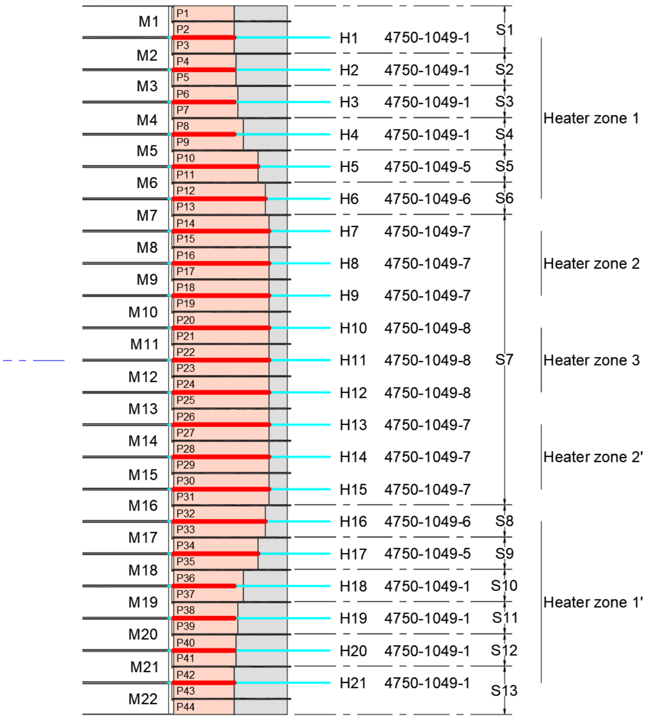

Figure 58 — Positioning of heaters in the magnet

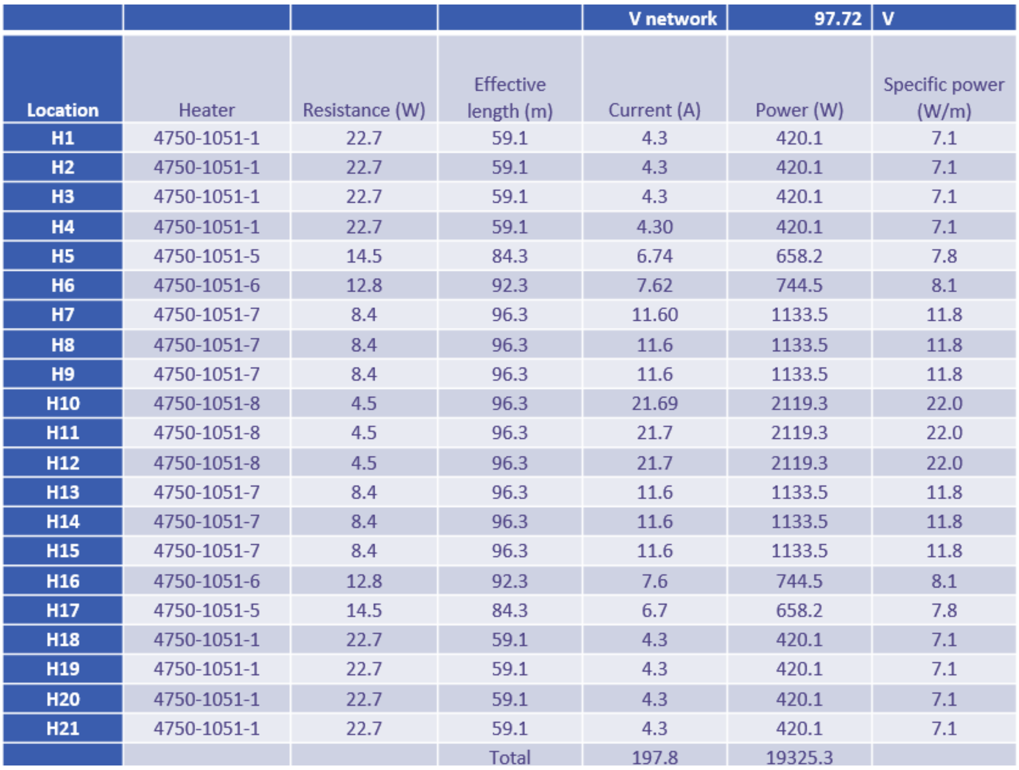

				V network	97.72	V
Location	Heater	Resistance (W)	Effective length (m)	Current (A)	Power (W)	Specific power (W/m)
H1	4750-1051-1	22.7	59.1	4.3	420.1	7.1
H2	4750-1051-1	22.7	59.1	4.3	420.1	7.1
H3	4750-1051-1	22.7	59.1	4.3	420.1	7.1
H4	4750-1051-1	22.7	59.1	4.30	420.1	7.1
H5	4750-1051-5	14.5	84.3	6.74	658.2	7.8
H6	4750-1051-6	12.8	92.3	7.62	744.5	8.1
H7	4750-1051-7	8.4	96.3	11.60	1133.5	11.8
H8	4750-1051-7	8.4	96.3	11.6	1133.5	11.8
H9	4750-1051-7	8.4	96.3	11.6	1133.5	11.8
H10	4750-1051-8	4.5	96.3	21.69	2119.3	22.0
H11	4750-1051-8	4.5	96.3	21.7	2119.3	22.0
H12	4750-1051-8	4.5	96.3	21.7	2119.3	22.0
H13	4750-1051-7	8.4	96.3	11.6	1133.5	11.8
H14	4750-1051-7	8.4	96.3	11.6	1133.5	11.8
H15	4750-1051-7	8.4	96.3	11.6	1133.5	11.8
H16	4750-1051-6	12.8	92.3	7.6	744.5	8.1
H17	4750-1051-5	14.5	84.3	6.7	658.2	7.8
H18	4750-1051-1	22.7	59.1	4.3	420.1	7.1
H19	4750-1051-1	22.7	59.1	4.3	420.1	7.1
H20	4750-1051-1	22.7	59.1	4.3	420.1	7.1
H21	4750-1051-1	22.7	59.1	4.3	420.1	7.1
			Total	197.8	19325.3	

Table 10 – Heater power data

Table 10 shows the data of each heater placed between the modules. Fig. 59 shows the simplified sketch of the superconducting magnet during a quench event.

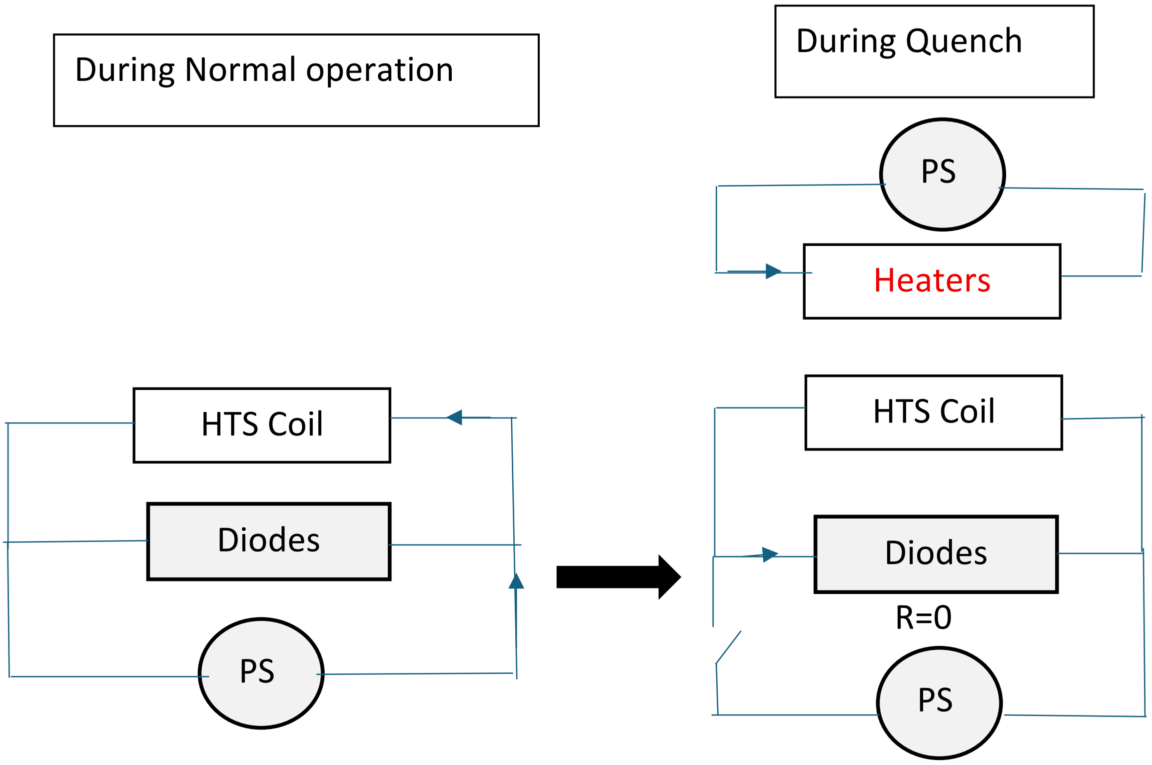

Figure 59- Simplified sketch of the Superconducting magnet - normal operation and quench

When the operation is within the superconducting zone (i.e., during normal operation), the R_{LSC} is almost negligible. Hence, the power supply (PS) delivers current to the HTS coil while the diode remains inactive. But, during the onset of quench, the superconducting state (which initiates locally) transitions into a normal resistive state (R_{LSC}), and the stored magnetic energy in the inductance 'L_{LSC}' starts dissipating rapidly in the form of Joule's heat in the resistive zone. It starts expanding with time due to the increase in the Joules heat. To prevent the localised heating, the heaters are activated, distributing the quench in the system and uniformly driving the coil into normal state. The current does not fall instantly but decays exponentially like that in an RL circuit. Simultaneously, the diode network provides a bypass path, diverting current away from the power supply and ensuring that the system behaves like R≈0 along the bypass path.

SIMULATION - I

For this simulation run, the operating current $I_{0p}(t = 0)$ was imposed at 645 A and held constant for 0.5 seconds(s).

The results obtained are then analysed on three major parameters: Current decay, temperature distribution across the pancake cross-section during the quench and the voltage trend of each module over time.

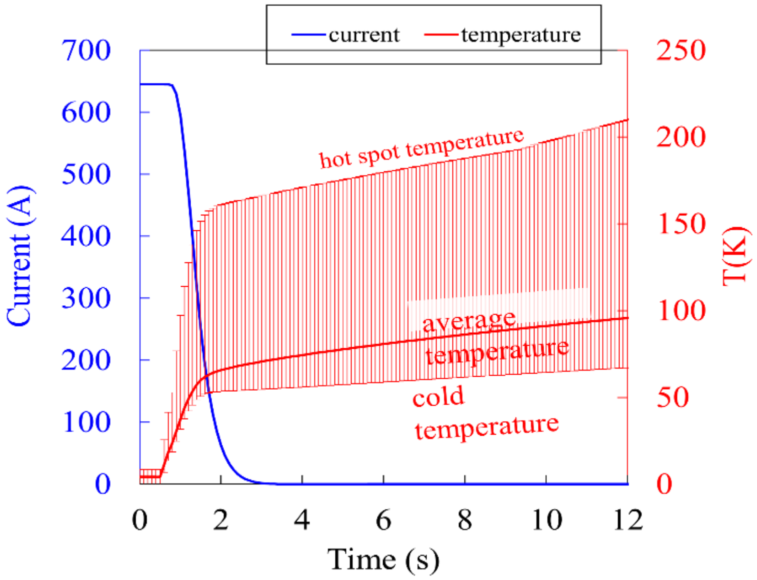

Figure 60- Current decay and temperature evolution over time for $I_{0p} = 645A$

Fig. 60 is a dual graph illustrating the current decay ('*blue*') and the temperature spread across all pancakes('*red*'). We note that, with the operating current of 645A, held constant for 0.5 seconds, there is a quench within 2 seconds.

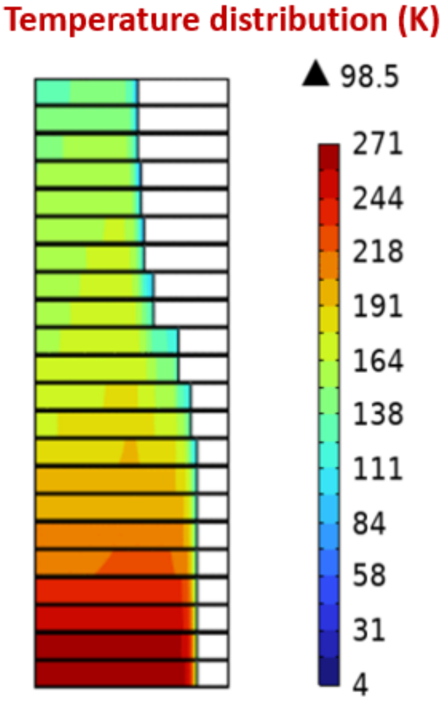

Figure 61- Temperature distribution across each pancake for $I_{0p} = 645\ A$

The maximum temperature reached is 271 K (as seen in Fig. 61) near the central pancakes since the power delivered by the central heaters (H10, H11, H12 in Table 7) is the highest. The temperature distribution during the quench is spread extensively. The hotspot temperature peak is 200 K while the cold temperature drops to 75 K. The average temperature is 100 K.

The total voltage drop of the modules is given by the sum of resistive and inductive voltages.

The resistances are derived from the model, while the voltage of each pancake is calculated using the Eq. 53(for i = 1, 2, ..., 44):

$$V_{p,i}(t) = R_{p,i}(t) \cdot I_{op}(t) + \sum_{j=1}^{44} M_{i,j} \cdot \frac{dI_{op}(t)}{dt} \qquad \textit{(Eq.53)}$$

Where $R_{p,i}(t) \cdot I_{op}(t)$ is the resistive voltage drop and $\sum_{j=1}^{44} M_{i,j} \cdot \frac{dI_{op}(t)}{dt}$ is the inductive voltage drop. Particularly, $M_{i,j}$ is the mutual inductance between pancake i and j with $M_{i,i}$ equals the self inductance of the i-th pancake. Fig. 62 exhibits the resistances of each module.

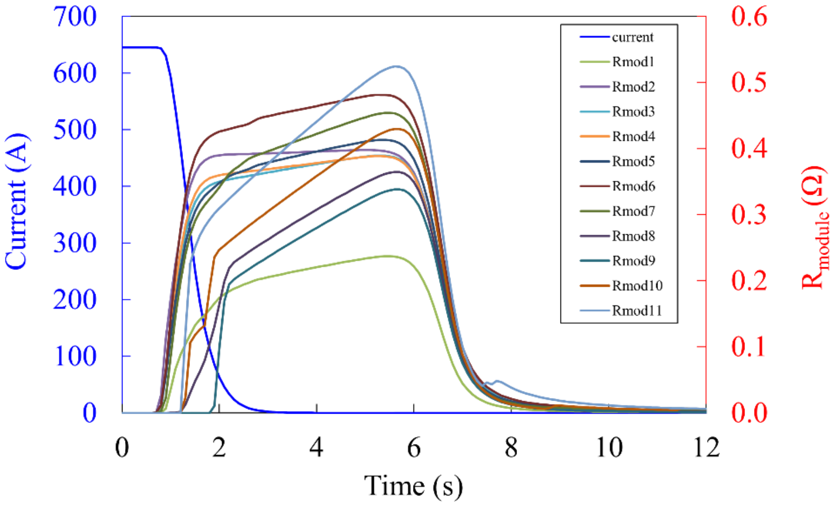

Figure 62 - Resistance distribution over time for $I_{0p} = 645\ A$

The resistance of the modules starts increasing from 0.5 second to 1.5 seconds indicating the quench initiation. After about 7.2 seconds, the module resistance drops rapidly to zero, corresponding to the current reaching ~ 0 and the end of quench dissipation. The combination of the resistive and the inductive voltage drop, gives the resultant voltage drop as displayed in Fig. 63.

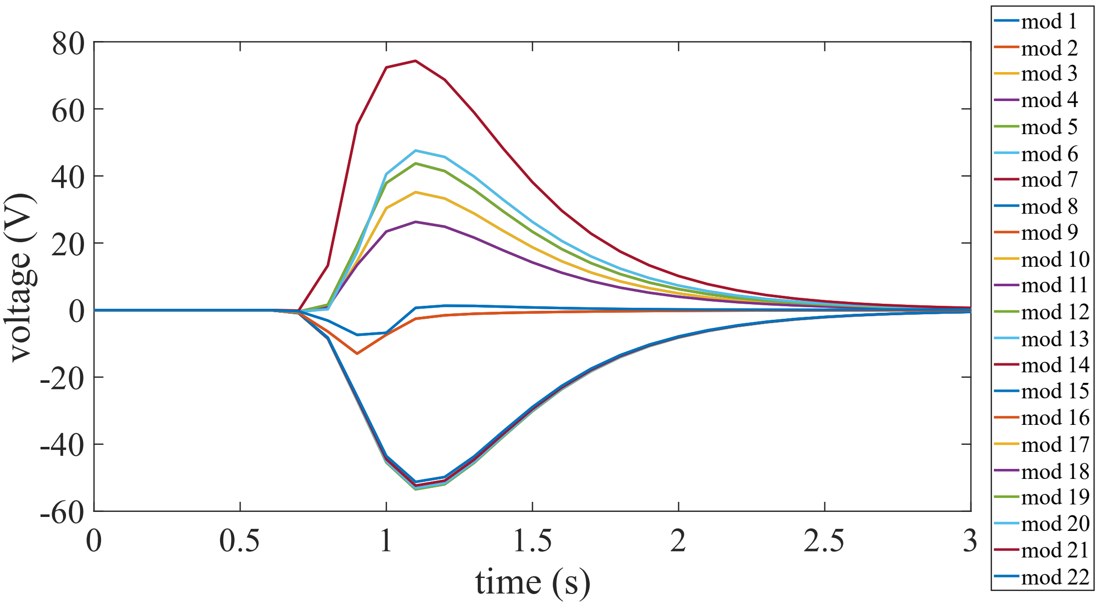

Figure 63 - Trend of modular voltage over time for $I_{0p} = 645A$

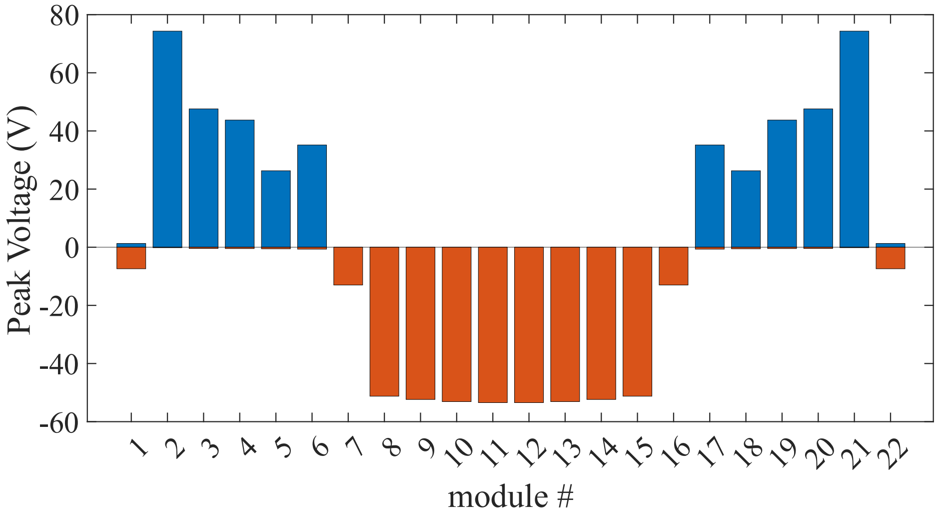

Figure 64 - Peak Modular voltage for $I_{0p} = 645A$

From Fig. 63 and Fig. 64, we observe that the peak voltage is observed on modules 2 and 21 at approximately 75 V.

SIMULATION II

In this simulation run, the operating current $I_{0p}(t = 0)$ is imposed at 355 A and held constant for 0.5 seconds(s).

NHMFL quench tests were performed at operational current of 355A, 465A and 609A. Our initial check intended to observe whether the results of the simulation run performed in UniBO mimics the experimental results of NHMFL. For 355A and 465A, the correction coefficient is assumed as 1 while for 609A, the correction coefficients is changed for a few pancakes.

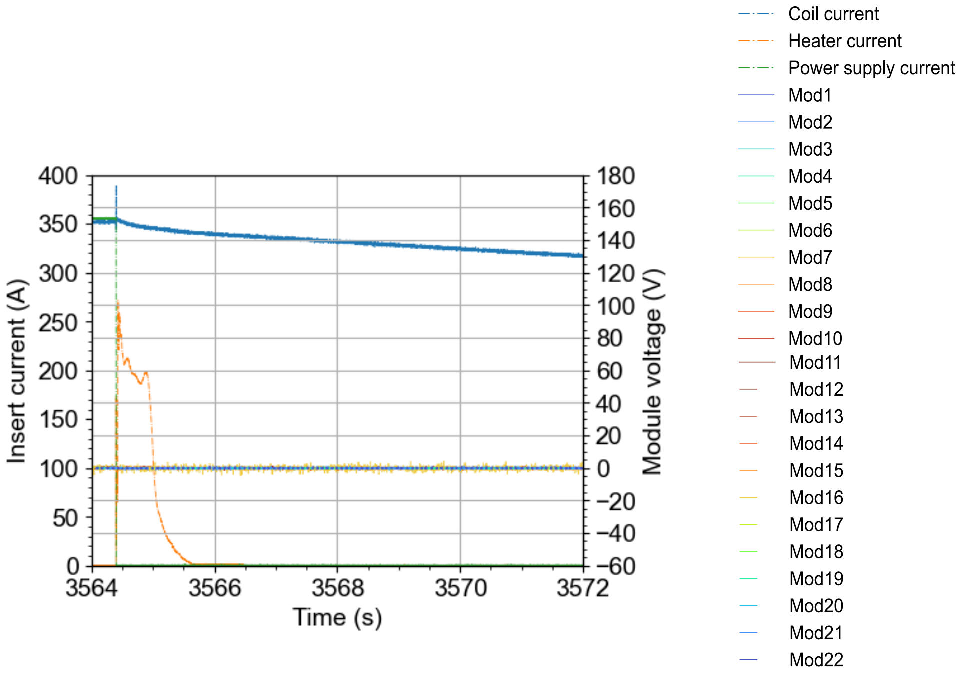

Figure 65 - NHMFL results for current decay for $I_{0p} = 355A$

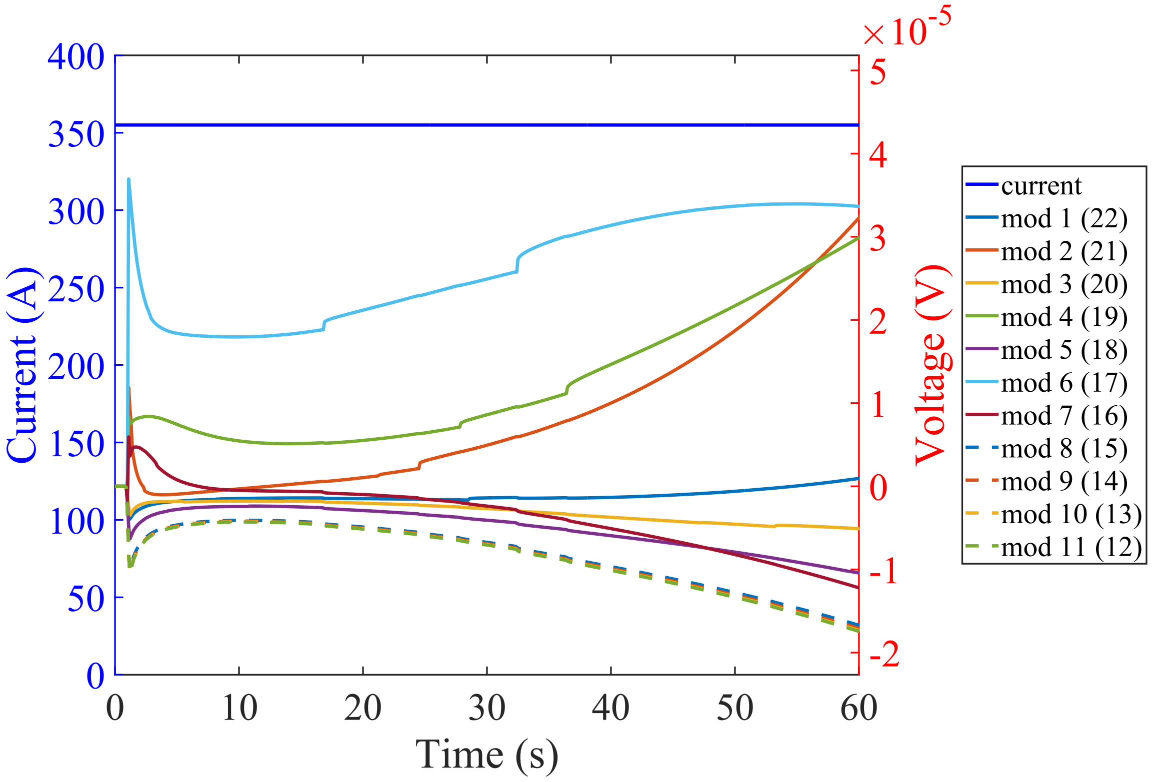

Figure 66 - UniBO results of current decay for I_{0p} = 355A

No quench is observed in either of the results, the current remains constant at 355A as expected. So, the resultant voltage drop in the modules is only due to the resistive effect. The temperature variation is shown in the Fig. 67 and the hotspot temperature is around 37 K.

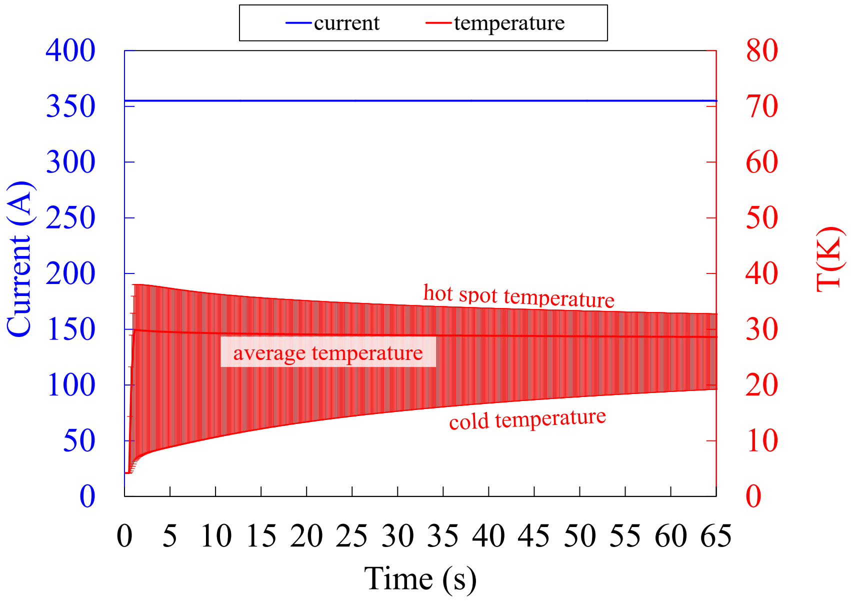

Figure 67 - Temperature variation for I_{0p} =355A

SIMULATION III

The operating current $I_{0p}(t = 0)$ was changed to 465 A and held constant for 0.5 seconds(s)

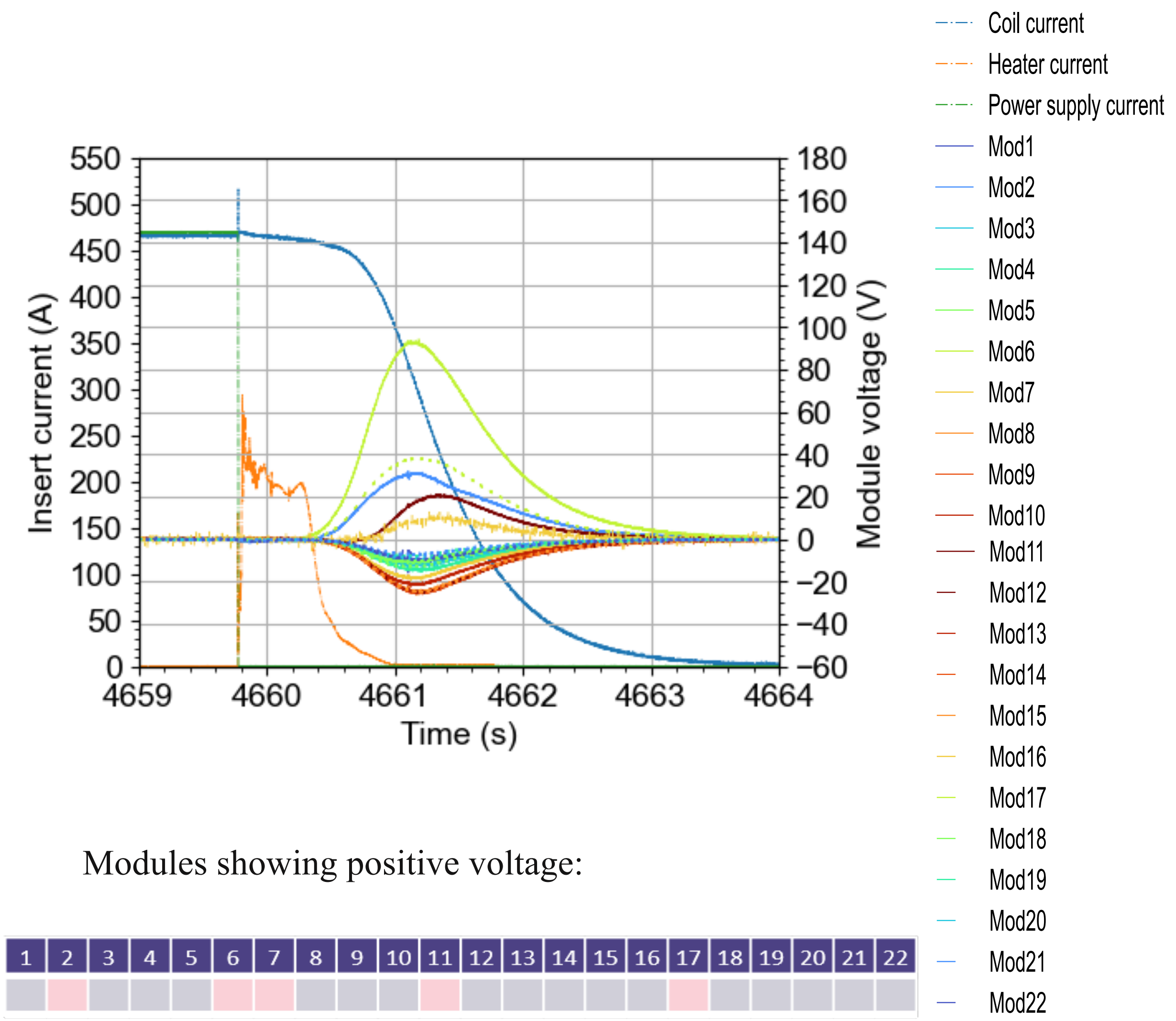

Modules showing positive voltage:

1	2	3	4	5	6	7	8	9	10	11	12	13	14	15	16	17	18	19	20	21	22
⬜	🟥	⬜	⬜	⬜	🟥	🟥	⬜	⬜	⬜	🟥	⬜	⬜	⬜	⬜	⬜	🟥	⬜	⬜	⬜	⬜	⬜

Figure 68 - NHMFL results of current decay and modular voltage for I_{op}=465A

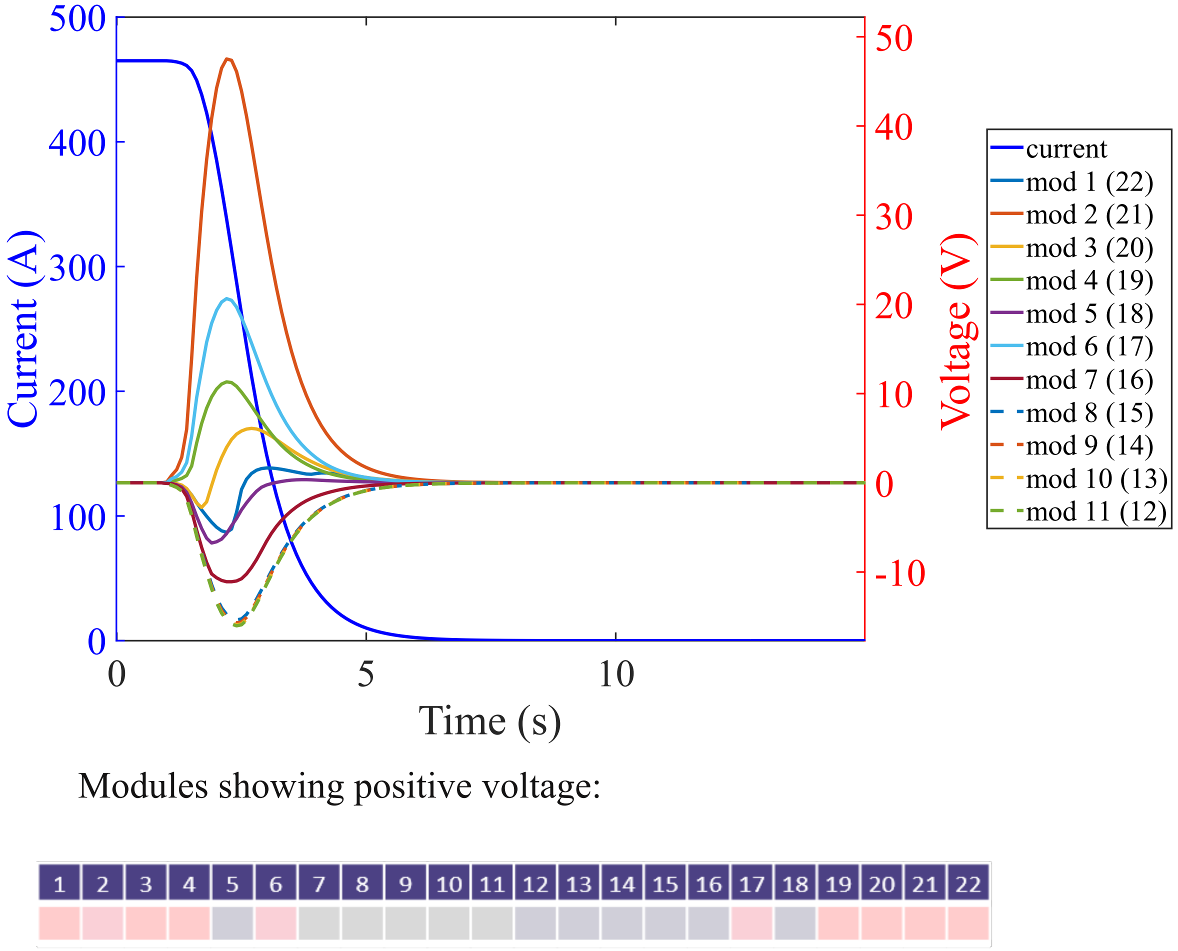

Figure 69 - UniBO results of current decay and modular voltage over time

We observe in Fig. 68 and Fig.69 that with I_{op} as 465 A, there is a quench in both the results. However, there are differences in the modules showing positive voltages and the peak voltages thereby. According to the results obtained from NHMFL, the highest peak voltage is noted corresponding to module 6 to be around 90 V and for UniBO, it is noted for module 2 to be around 50 V. Module 6 is noted to have the second highest peak voltage at around 20 V. The temperature distribution is shown in Fig. 70. Hot spot temperature is approximately at 92 K.

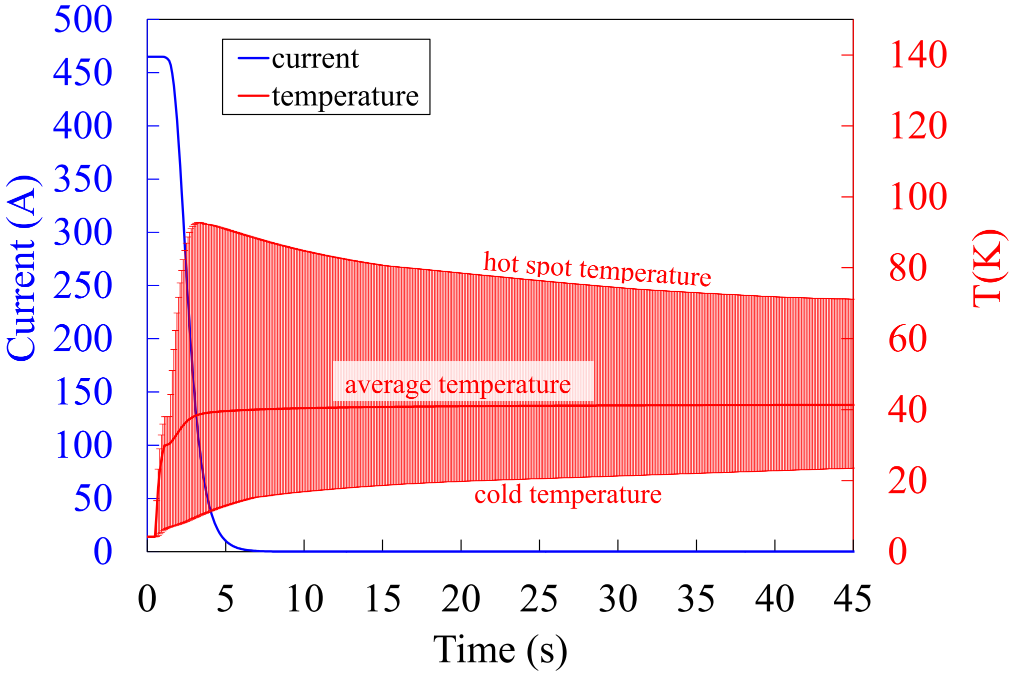

Figure 70 - Temperature distribution for I_{op} *= 465A*

SIMULATION IV

In this run, we simulate the quench with I_{op} = 609A. Unlike the previous cases, the correction coefficients were changed from 1 to 0.6 only for modules 6 and 7. Rest of the modules were maintained as is. NHMFL results showed that the highest peak voltage module was 6.

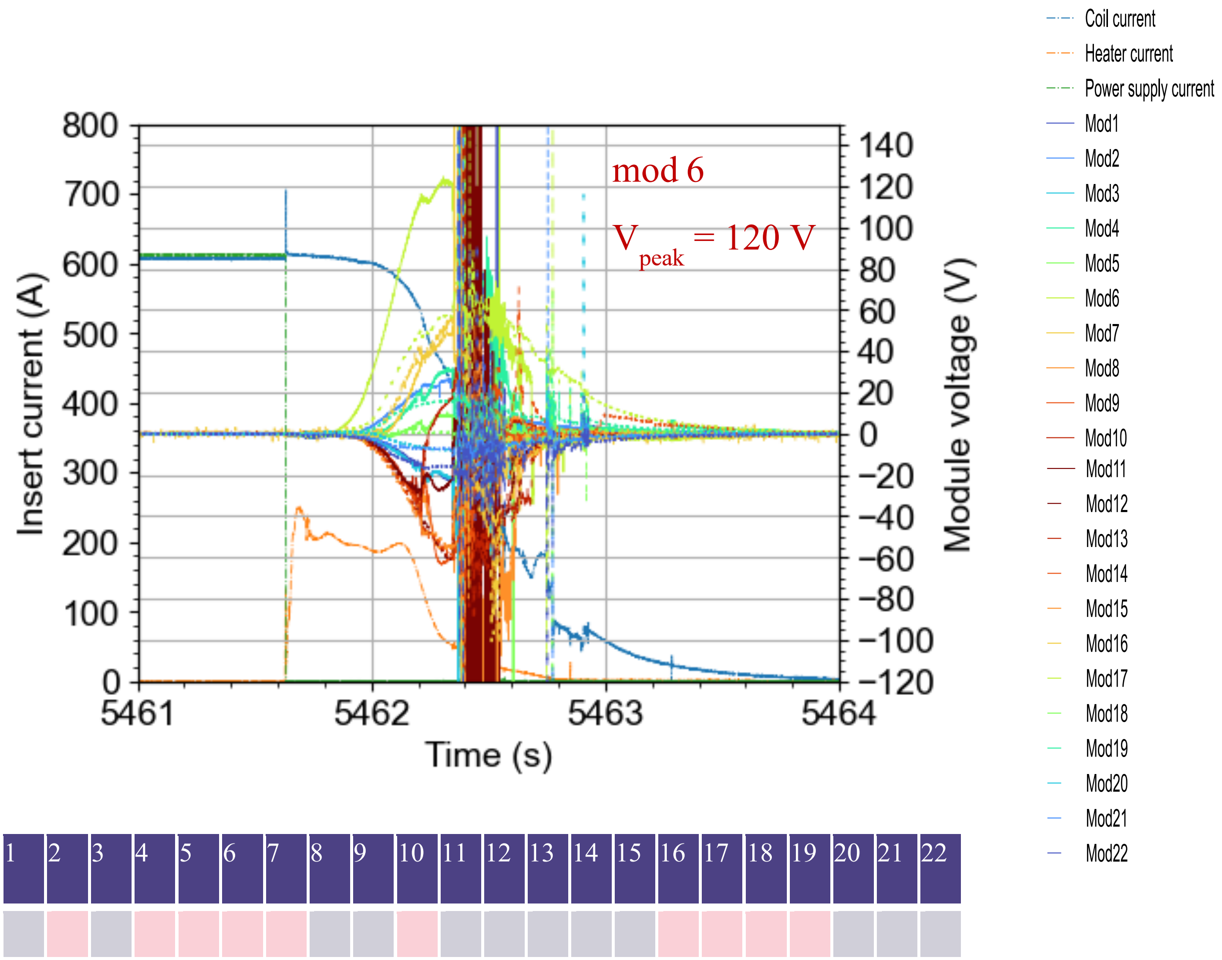

1	2	3	4	5	6	7	8	9	10	11	12	13	14	15	16	17	18	19	20	21	22
⬜	🟥	⬜	🟥	🟥	🟥	🟥	⬜	⬜	🟥	⬜	⬜	⬜	⬜	⬜	🟥	🟥	🟥	🟥	⬜	⬜	⬜

Modules showing positive voltage:

Peak voltage Module: Mod 6

Figure 71 – NHMFL results for modular voltages for I_{op} =609A

UniBO results showed the same (see. Fig.72). The peak voltage was observed in Module 6 at around 120 V.

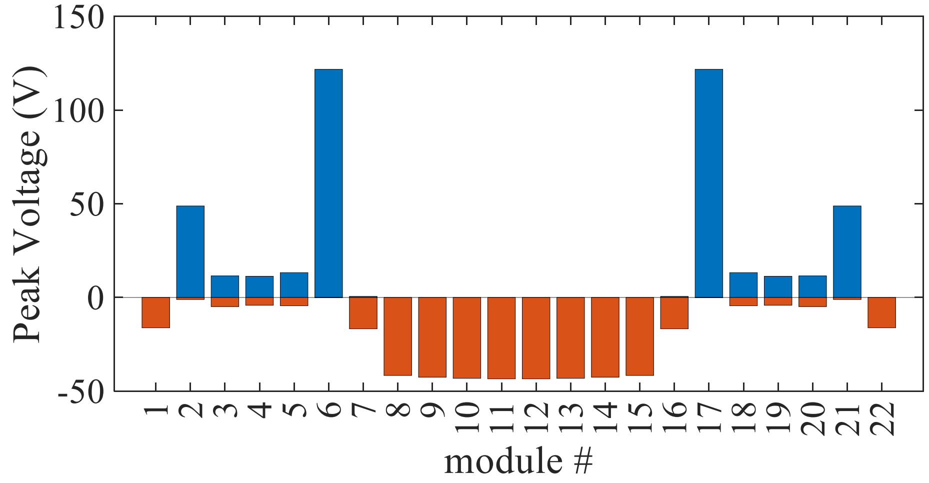

Figure 72 - UniBO results of modular voltages for I_{op} =609A

Furthermore, a comparison of the current decay was conducted between the NHMFL results and UniBO results for operational current equal to 609 A. In the first instance, the operational current was considered as 609 A and the correction coefficients (I_c coefficient) for all modules were kept as per Fig. 73. The resultant current decay curves are compared in Fig. 74. There are three current decay curves shown in the comparison. The red solid line indicates the current decay achieved through the experimental result at NHMFL; the blue solid line denotes the UniBO simulation of the quench where the correction coefficients have been kept as per Fig. 73 and the blue dashed line represents the UniBO simulation of the quench where the correction coefficients are considered as 1.

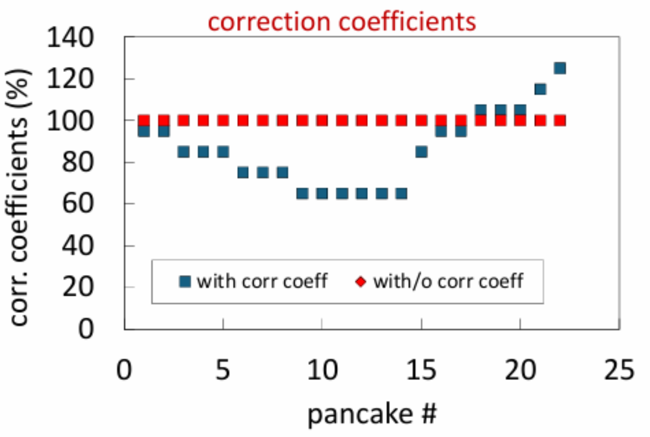

Figure 73- Correction coefficients for $I_{0p} = 609A$

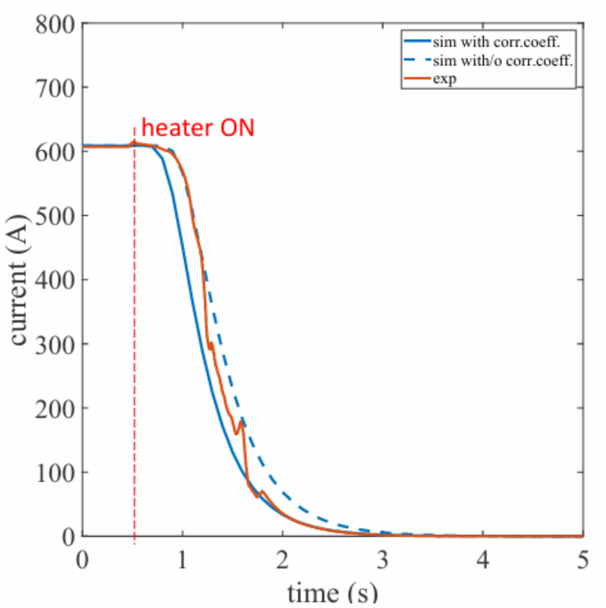

Figure 74 - Current decay comparison of NHMFL experiments and UniBO simulations

A persistent error was observed between the simulation results and the experimental current decay. The simulation run without the correction coefficient graph follows the experimental current decay until 1.5 seconds and then deviates. To reach closer to the experimental curve, the correction coefficient on modules 6 and 7 was changed to 0.6 and the correction coefficient of the rest of the modules were fixed at 1. And the quench was simulated.

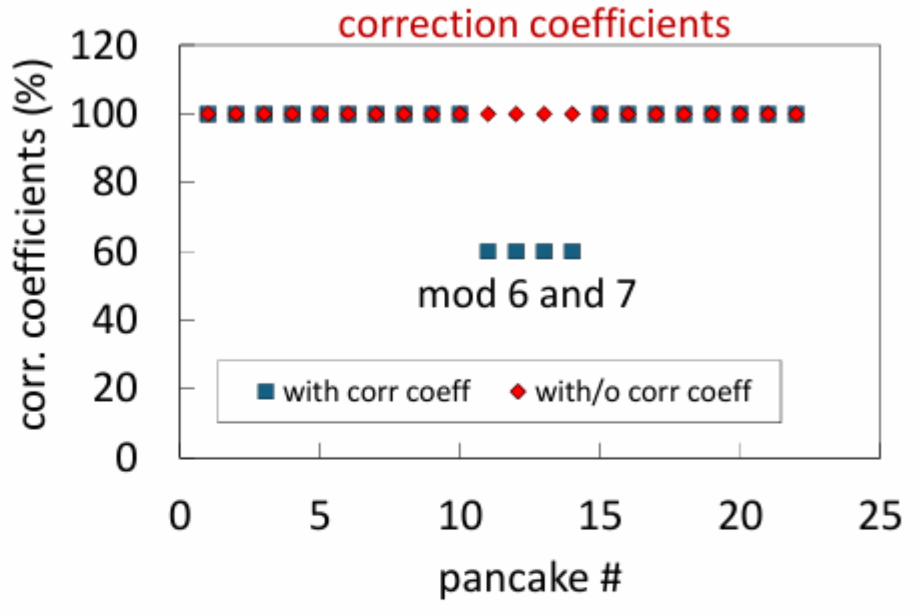

Figure 75 - Correction coefficient for $I_{0p} = 609A$

A significant reduction in the error between the experimental and the simulation current decay values was observed in this quench simulation run. (See Fig.76).

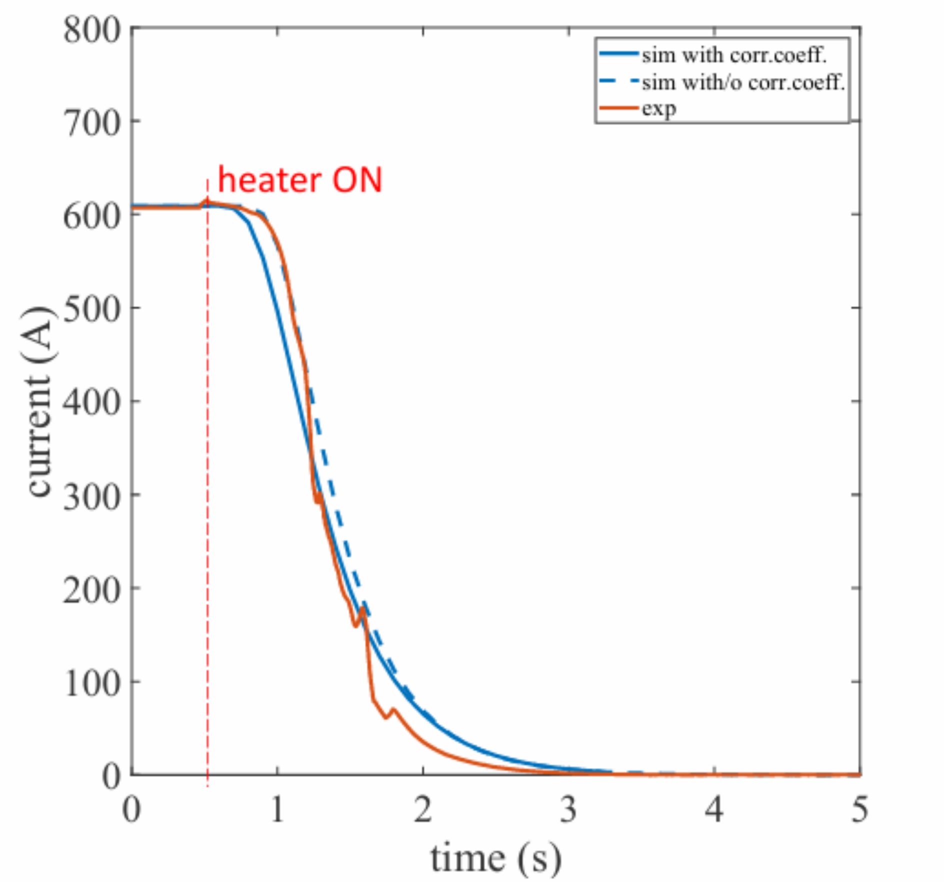

Figure 76 - Current decay values

Upon comparing cases 1 and 2, classified as one where the correction coefficients were kept as per Fig. 73 and another where the correction coefficients were kept as per Fig. 75, the $^{I}/_{I_c}$ ratio for both the cases, were compared. Case 2 seems to be more critical than Case 1, as it suggests imminent quench risk. Nonetheless, Case 2 is more conservative and highlights the need for robust quench protection methods. These results are thereby shown in Fig. 77.

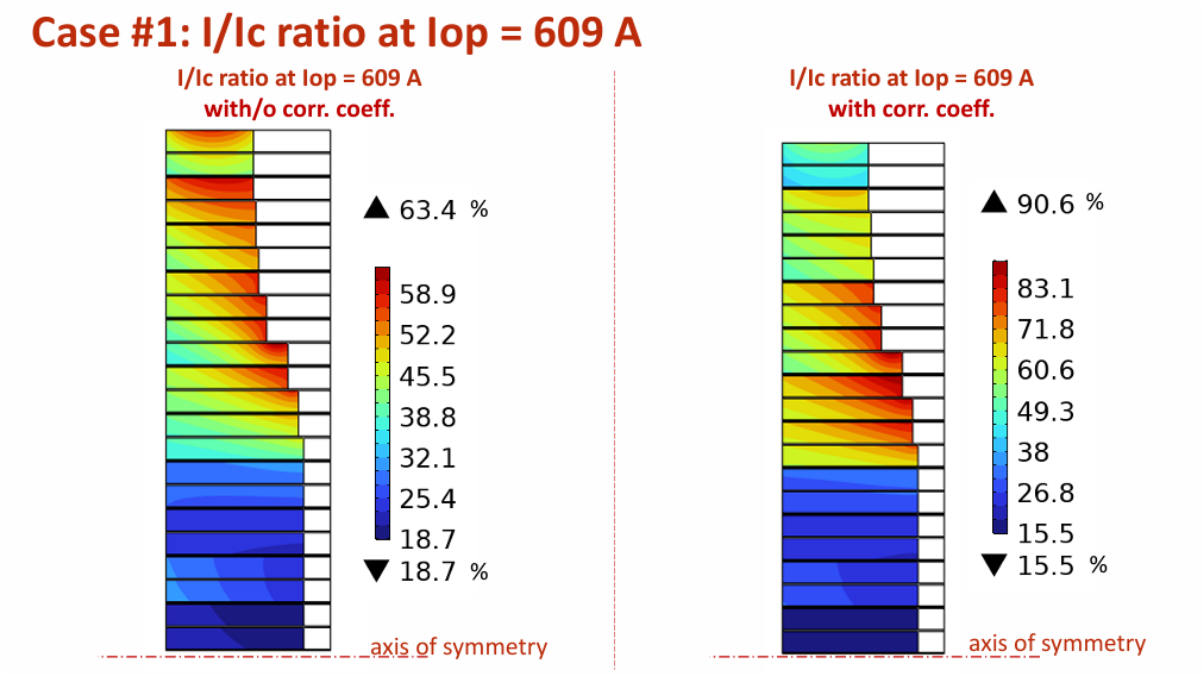
Case #1: I/Ic ratio at Iop = 609 A

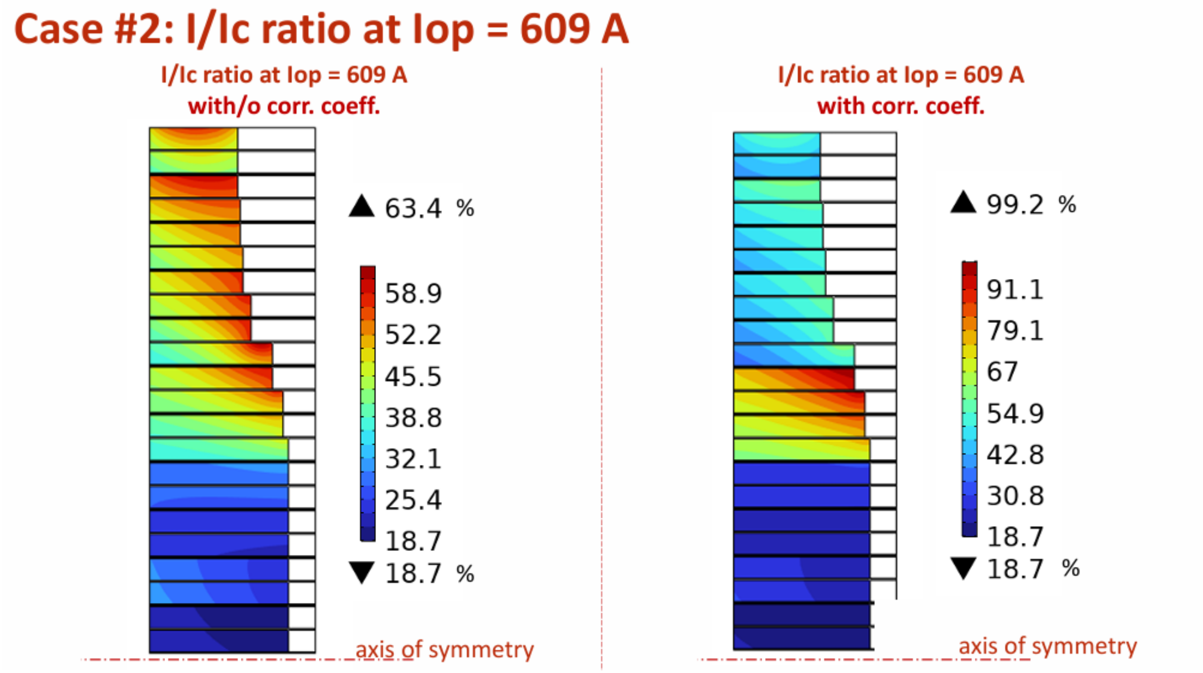
Case #2: I/Ic ratio at Iop = 609 A

Figure 77 - $^{I}/_{I_c}$ *ratio for* I_{op} *=609A.*

The subsequent figures exhibit resistance of each module and the voltage per module for operational current 609A.

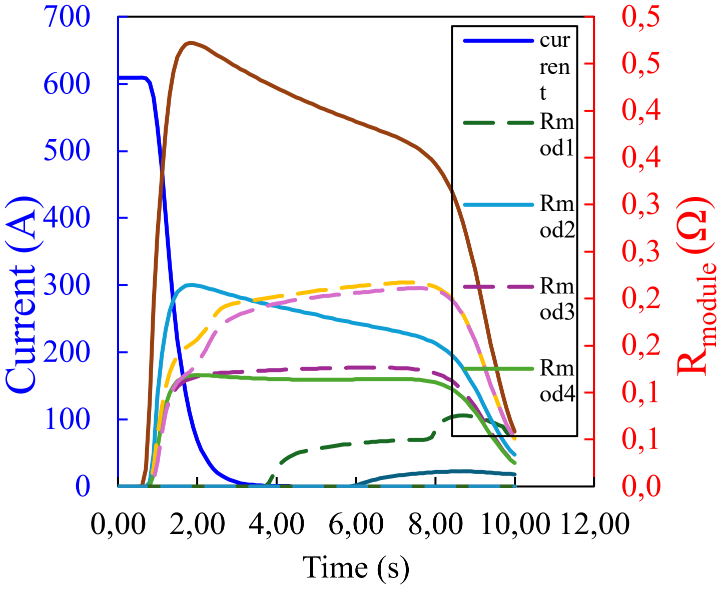

Figure 78 - Resistance distribution over time for I_{op} = 609A

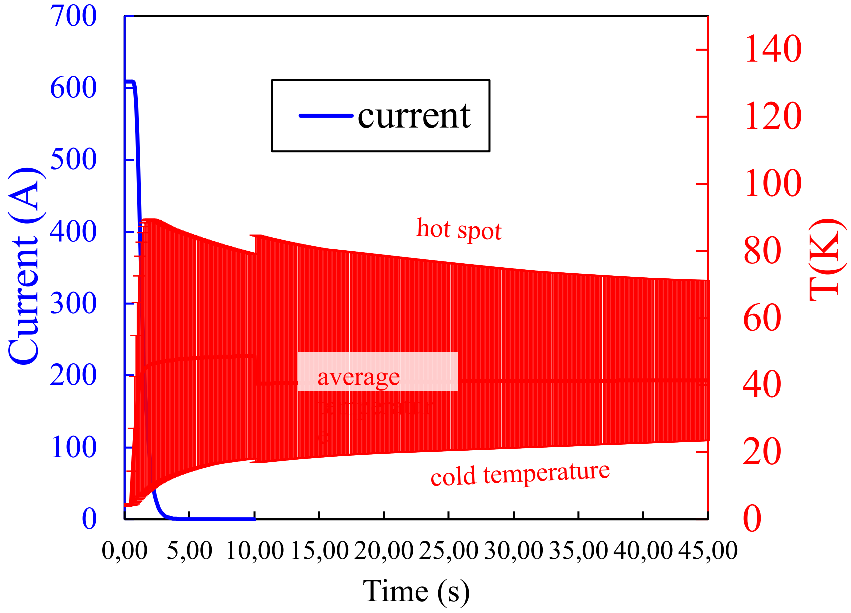

Fig 79 - Temperature over time for I_{op}= 609A

The hotspot temperature reaches around 85 K, and the average temperature stays around 40 K. This shows consistency with the previous cases - as the operation current decreases, the hotspot temperature and the average temperature decreases as well.

Current Sharing Temperature

In a superconducting magnet, when the temperature increases beyond the critical temperature, while maintaining the current constant at the operating value, it determines the reaching of the critical surface at a *'current sharing' temperature* or redistribution of the current. It is termed as 'current sharing' because the superconducting material is unable to carry a current higher than the critical current and the current is shared between the superconductor and the normal material. Below this temperature, all current is carried by the superconductor. Naturally, upon increasing the temperature further, the superconductor carries at most the critical current, so the current in the normal material increases, until it becomes equal to the total current at the critical temperature T_c.

The current in the superconductor remains constant at the I_{op} value until the temperature is below the T_{cs}, then it decreases along the I_c (T) curve. At temperature T_c, the current is zero in the superconductor and all the operational current flows in the copper stabilizer.

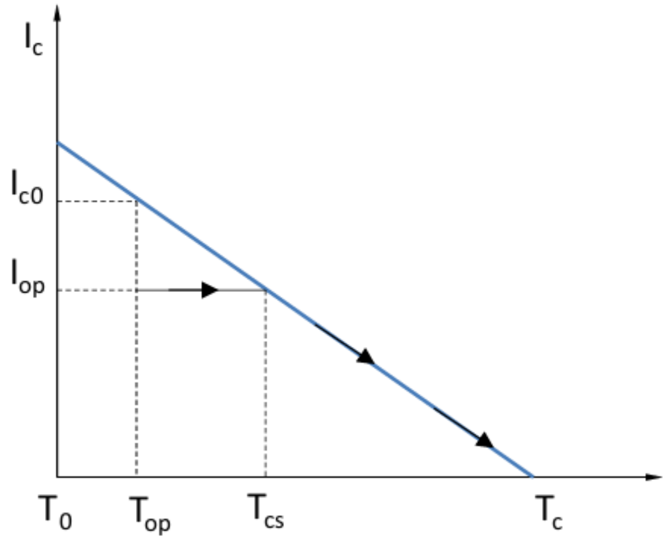

Figure 80 - Effect of the temperature increase on the critical current and on the operating point of the conductor

The mathematical relationship between the critical temperature, current sharing temperature, operating current and operating temperature is given by the equation.

$$\frac{I_{op}}{T_c - T_{cs}} = \frac{I_{c0}}{T_c - T_{op}} = \frac{I_c}{T_c - T} \tag{Eq.55}$$

where,

I_{op} = operational current

I_{c0} = indicates the value assumed by critical current in correspondence with the operating temperature of the magnet: $I_{c0} = I_c(T_{op})$

T_c = critical temperature

T_{op} = operating temperature of magnet

T_{cs} = current sharing temperature

T = Temperature at that given instant

I_c = critical current

The current sharing temperature in the LSC computed at the nominal operating condition is shown in Fig.81.

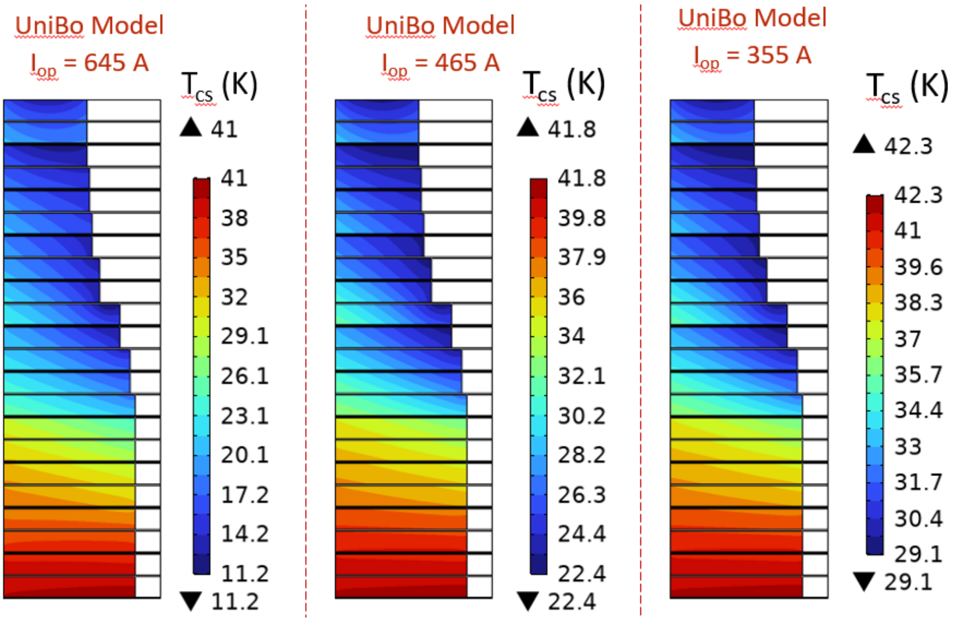

Figure 81 - Current sharing temperature for different operating currents

From Fig. 81, it is evident that, as the operating current decreases, the current sharing temperature increases thereby increasing safety margin from quench. For 645 A, the T_{cs} is lower particularly in lower pancakes where they reach 11.2 K. The risk of premature quench is significantly higher. For 465 A, minimum T_{cs} = 22.4 K which shows improved margin and for 355 A, minimum T_{cs} = 29.1 K, which keeps the system far from instability.

The current sharing temperature is a critical parameter in the quench analysis of a superconducting magnet, as it defines the temperature threshold above which the magnet cannot carry the full operating current alone and shares a part of it with the normal material. This transition has a direct impact on the instability. The lower the thermal margin, the smaller the safety margin. The lower the T_{cs}, higher is the probability to trigger Joule heating due to normal resistive effect.

CONCLUSION

This thesis highlights the study and electrothermal analysis of the quench phenomenon in a prototype coil, named as LSC, in the frame of the 40 T superconducting magnet under construction at the NHMFL laboratory.

A COMSOL-based model was developed, implementing both the heat balance equation and the constitutive equation (Kirchhoff's voltage law applied to the magnet).

The model enables and ensures calculation of:

- temperature distribution within the magnet during quench
- current flow through the conductor
- resistance and voltage across each module of the magnet.

The simulations ensure the study of the behaviour of the system, after quench detection, i.e., when all heaters are activated. The purpose of the heaters is to uniformly heat the superconducting material to prevent localized hot spots, which would irreparably damage the material and the magnet.

Based on the results, during the quench with an operating current of 645 A, the temperature in the LSC exhibits an average value of ~100 K after 12 seconds of heater activation. A decrease in the average temperature was observed upon decreasing the operating current.

The model also provides values for resistance and voltage across each magnet module, yielding voltages around 50–60 V. The most critical modules are not necessarily the central ones with the highest magnetic field, but rather modules 2–6, where a combined effect of magnetic field strength and field angle impacts the critical current of the superconductor.

Resistive growth is gradual and sustained, showing that energy is effectively spread across multiple modules, helpful for quench protection.

There is a safe decay in the current, demonstrating the system's ability to handle the quench without its failure.

The plots reflect good thermal stabilization and symmetry, though, variation in resistance peaks may suggest uneven heat transfer or material properties across the modules.

The current sharing temperature is a critical parameter to assess the stability of the magnet. Upon careful consideration of this factor, it would enable engineers to identify weak zones in the magnet and prioritise placement of heaters, sensors and dump resistors.

REFERENCES

1. https://www.energy.gov/science/doe-explainssuperconductivity#:~:text=Superconductivity%20is%20the%20property%20of,transition%20to%20the%20superconducting%20state.
2. https://nationalmaglab.org/about-the-maglab/around-the-lab/maglab-dictionary/resistive-magnet/
3. Mark D Bird., *Superconducting magnet technology for the outer coils of resistive-superconducting hybrid magnets,* IOP
4. Dr. Safa Hasan Mohammed, Almustaqbal University College
5. M. Breschi et al., *Analysis of Quench in NHMFL REBCO Coils for the 32 T Magnet Project*, University of Bologna, 2016
6. Theory of Superconductivity* , J Bardeen, L.N . Cooper,, J.R.Schreiffer, Volume 108, Number 5
7. M. Noe, R. Heller, W.H. Fietz, W. Goldacker, Th. Schneider, Forschungszentrum Karlsruhe, Karlsruhe, Germany , HTS APPLICATIONS, ,
8. M. Marchevsky , Quench detection and protection for HTS accelerator magnets, LBNL
9. https://www.iter.org/
10. https://nationalmaglab.org/magnet-development/magnet-projects/
11. F. Toral, Mechanical Design of Superconducting Accelerator Magnets, CIEMAT, Madrid, Spain,
12. M. Wilson, Superconducting Magnets (Clarendon Press, Oxford, 1983).
13. Shuangsong Dua et al., *ITER PF6 double pancakes winding line, Fusion Engineering and Design, Volume 116, March 2017, Pages 10-16*
14. L. Cavallucci et al., *A Numerical Study of Quench in the NHMFL 32 T Magnet*, IEEE Transactions on Applied Superconductivity, Vol. 29, No. 5, 2019
15. Tara Benkel et al., *REBCO tape performance under high magnetic field,* Eur. Phys. J. Appl. Phys. (2017) 79: 30601
16. Available on http://www.superpower-inc.com/content/ 2g-hts-wire
17. D. Uglietti, H. Kitaguchi, S. Choi, T. Kiyoshi, IEEE Trans. Appl. Supercond. 19 (2009)
18. P.M. Leys et al., IEEE Trans. Appl. Supercond. 23, 8000604 (2013)
19. William N Hartnett et al., *Characterization of edge damage induced on REBCO superconducting tape by mechanical slitting*, Eng. Res. Express 3 (2021) 035007

20. Sundaram A et al 2016 2G HTS wires made on 30 μm thick hastelloy substrate Supercond. Sci. Technol. 29 104007
21. https://www.comsol.com/comsol-multiphysics